Improving the stability of copper oxide nanoparticles in photoelectrochemical water splitting

By

Nteseng Dorah Mano Mosalakgotla

Submitted in partial fulfilment of the requirements
for the degree

Master of Science (MSc) in Physics

in the
Faculty of Natural and Agricultural Sciences
Department of Physics
University of Pretoria
Supervisor: Prof MM Diale

February 2022

Declaration

I, **NTESENG DORAH MANO MOSALAKGOTLA**, declare that the dissertation, I hereby submit for the degree of Master of Science (MSc) in Physics at the University of Pretoria, is my work and has not been submitted previously by me for a degree at this or any other institution. Any work of others that have been drawn upon is duly acknowledged in the text, and a list of references is presented at the end of every chapter.

Signature:

Date: 7th February 2022

Student number: 20753782

Abstract

In this work, the processing parameters of preparing dip coated CuO films which includes the withdrawal rate, film thickness and annealing temperature were optimized for photoelectrochemical (PEC) water splitting. The CuO samples were fabricated on fluorine-doped tin oxide (FTO) substrates at withdrawal rates of 50-200 mm/min, having films of 239.7-693.6 nm thicknesses, and annealed at 400-650 °C in air for 1 hour. Furthermore, the CuO films prepared at withdrawal speed of 150 mm/min, with thickness of 397.3 nm and annealed at 600 °C were modified with 1, 3, and 5 protective layers of activated charcoal (AC) silver (Ag), and gold (Au) nanoparticles (NPs) to improve their photo-stability in electrolyte. All the prepared CuO films were used as photocathodes in a three-electrode PEC device for water splitting. X-ray diffraction (XRD) and Raman spectroscopy studies confirmed the preparation of highly crystallized pristine CuO, CuO/AC, CuO/Ag and CuO/Au thin films. Linear Sweep Voltammetry (LSV) measurements yielded the highest photo-current density of 2.9 mA/cm^2 at 0.35 V vs RHE for films prepared at withdrawal speed of 150 mm/min, with thickness of 432.8 nm and annealed at 600 °C. The high photo-current recorded was linked to the optimization of the film thickness, optical absorbance, crystallization, and the low resistance to the transfer of charge carriers at the photocathode/electrolyte interface of the films. Chronoamperometry measurements done on the CuO samples revealed that the films could only sustain 28.4 % of its photo-current density after 500 s due to photo-corrosion occurring on the films surface. This implies that a significant portion of the photo-current density obtained for the pristine CuO photocathodes was because of photo-corrosion occurring on the film’s surface. The modification of the pristine CuO films with AC, Ag and Au generally resulted in reduced photo-current density due to the reduction of photo-corrosion occurring on the films surface. However, the photo-stability of the modified CuO films in electrolyte was significantly enhanced. The CuO/AC films yielded the best photo-stability for CuO/AC-5L photocathodes, retaining 45.5 % of its photo-current after 500 s. The CuO/Ag and CuO/Au films retained a maximum of 75.9 and 87.9 % of their photo-current densities for CuO/Ag-5L and CuO/Au-5L photocathodes after 500s, and 74.7 and 84.3 % after 1200 s respectively. This study emphasized the importance of optimizing the processing parameters of preparing dip-coated CuO films for PEC applications, before improving their photo-stability in electrolyte. Furthermore, enhancing the photo-stability of CuO films in electrolyte is paramount to their practical application in PEC water-splitting for hydrogen production.

List of abbreviations

PEC	Photoelectrochemical
CB	Conduction band
VB	Valence band
NHE	Near hydrogen electrode
HER	Hydrogen evolution reaction
OER	Oxygen evolution reaction
NPs	Nanoparticles
EIS	Electrochemical impedance spectra
RHE	Reversible hydrogen electrode
LSV	Linear scan voltammetry
MS	Mott Schottky
FTO	Fluorine-doped tin oxide
XRD	X-ray diffraction
FE-SEM	Field Emission scanning electron microscopy
EDS	Energy dispersive X-ray spectroscopy
CPE	Constant phase element
NRF	National Research Foundation
UV–vis	Ultraviolet and visible spectroscopy
SILAR	Successive ionic layer adsorption and reaction

Dedications

To my uncles Rev Kgomotso Jan Mosalakgotla, Pogiso Peter Mosalakgotla, and Solomon Santana Mosalakgotla for their unwavering support and putting me through the best education.

&

To my wonderful parents, Nkefi Maria Kgasi and Sello Jeremiah Kgasi, my sister Mmathapelo Mosalakgotla for their love and encouragement.

Acknowledgements

I would like to thank the almighty God for leading and guiding me through my studies. Through his word I was able to find comfort, wisdom, and strength to complete this degree.

I would like to express my sincere gratitude to my supervisor, Prof Mmantsae Diale for her fundamental contribution and support towards my MSc program. Also, my deepest gratitude to Dr Pannan I. Kyesmen for his support, encouragement, and constructive criticism. The daily meetings he organized were of much help. I will forever be grateful for the kindness and patience that they both have shown me.

I thank the HOD and the members of staffs of the Physics department for their kindness and providing a conducive atmosphere for me to carry out my MSc studies at my dream university. I also extend my gratitude to all members of the Clean and Green Energy research group of the Department of Physic for their assistance, encouragement, and moral support.

I acknowledge Dr Nombona for granting me access to one of the labs in the Department of Chemistry. I also thank the department of Chemistry for allowing me to use the XRD equipment, the microscopy and microanalysis lab for SEM and EDS trainings and measurements, and the carbon-based nanomaterial research group of the Department of Physics for allowing me to use the equipment for Raman spectroscopy.

Special thanks to the University of Pretoria for providing resources and a conducive environment which enabled me to study efficiently. Finally, thanks to the National Research Foundation (NRF) grant No#N0115/115463 (SARChI, M.D.) for financial assistance towards my MSc program.

Table of Contents

List of Figures

List of Tables

Chapter 1

1.0 Introduction

1.1 Background

Rising atmospheric temperature largely attributed to global warming is having a significant influence on climatic conditions, causing increases in sea levels [1], droughts [2], hurricanes [3], tornadoes [4], wildfires [5], and floods [2] in different parts of the world. Global warming is largely caused by the rising emissions of greenhouse gases such as carbon dioxide (CO_2), methane (CH_4), nitrous oxide (N_2O), and chlorofluorocarbons (CFCs), which act as a barrier in the atmosphere preventing the heat that is re-radiated by the earth's surface from escaping to space. As a consequence, the earth's atmosphere becomes warmer than the expected average temperature over time; a phenomenon that is commonly known as global warming [1, 6, 7]. Among the greenhouse gases in the atmosphere, CO_2 constitutes about 72 % and is regarded as the major source of global warming [8, 9]. Fossil fuels, presently considered as the conventional energy sources, are the main cause of CO_2 emissions into the atmosphere. The burning of fossil fuels at power plants for the generation of electricity [10], in the combustion engine of automobiles [11], and for industrial applications [12] among others results in the emission of large amount of CO_2 into the atmosphere. Renewable and sustainable energy sources are widely considered as a suitable substitute to the conventional energy sources for the mitigation of global warming.

Some popular renewable energy sources include the wind [13], biomass [14], and solar radiation [15] among others. Wind energy is typically utilized indirectly by converting kinetic energy to electrical energy using wind turbines. In 2013, 318.1 GW of power was generated globally from the wind energy [16]. Wind has a potential to meet a significant portion of the growing energy demand. However, wind energy systems are very noisy and possess some health risk to the inhabitants living around the turbines. People living or working near the wind turbines have been reported to suffer from hearing loss, stress or sleep disturbance [13]. Furthermore, wind turbines are very costly and require a large-scale investment from the public or private sector [16]. Biomass are organic substances which store solar energy in the form of chemical energy [17]. They are typically used to generate electricity, heat and biofuels from agricultural residues or solid waste [14]. They produce far less emissions than fossil fuels, reduce the amount of waste in landfills, and revitalize rural communities through the creation of employment [17]. However, the excessive use of biomass as an alternative source of energy, can result in deforestation and slight pollution, which will partly contribute towards increasing the greenhouse gas emissions [14]. Solar energy is considered to be the most ideal energy source as it is free, abundant and has the least negative impacts on the environment. Solar radiation reaching the surface of the earth in a year can provide more than 10,000 times of the energy required globally [18]. Solar energy is typically harnessed using photovoltaic systems to get electric power [19], solar thermal devices to generate electricity [20] and photoelectrochemical (PEC) water-splitting to produce hydrogen (H_2) [21].

PEC water-splitting is a suitable sustainable approach for H_2 production using solar energy and water as the main raw materials [22, 23]. H_2 is an alternative clean fuel which has the potential to greatly contribute towards resolving the global energy crises, since its combustion only produces water (H_2O) as by-product [24]. More so, it is also versatile and eco-friendly [25]. To produce hydrogen through PEC water-splitting, a photoelectrode is immersed in an aqueous electrolyte and illuminated with light in a photocatalytic cell [23]. This will result in the generation of charge carriers in the photoelectrode [26]. For n-type photoelectrodes, the minority charge carriers (holes) in the valence band get transferred to the semiconductor/electrolyte interface to perform photocatalytic reactions [27, 28]. For p-type photoelectrodes, minority charge carriers (electrons) are moved to the semiconductor/electrolyte interface where they also perform photocatalytic reactions for hydrogen generation [29, 30].

For a photoelectrode to be considered suitable for PEC water-splitting, it is required to be stable under aqueous solutions [31], possess a small bandgap (E_g) [32], own the right band-edge positions [33], have a large carrier diffusion length, [32], and be highly crystalline [34]. Since the first photoelectrode (a TiO_2 photoanode) was reported by the pioneers of PEC water-splitting Honda and Fujishima in 1972 [35], a single photoelectrode that meets all the requirements for a suitable photocatalyst has not been found [23]. Photocathodes such as CuO [21], GaAs [36], Cu_2O [37], Sb_2Se_3 [38], $CuFeO_2$ [39] have been utilized for PEC water-splitting. Among these, CuO semiconductors have emerged as one of the promising photocathodes for PEC applications due to their narrow bandgap (~1.2 eV) [40], suitable conduction band-edge position [41], low cost, and the abundance of copper element [42].

1.2 Motivation

As mentioned in section 1.1, CuO semiconductors have emerged as promising photocathodes for PEC applications due to their small bandgaps and other fascinating properties. However, the primary challenge of using CuO as a photocathode for hydrogen evolution is its poor photo-stability in aqueous solutions, as a consequence of the self-reduction that occurs in the material by photo-excited electrons during photocatalysis [21, 43]. Several strategies can be implemented to improve the photo-stability of CuO photocathodes in the electrolyte for large scale PEC applications. These include doping with metal/non-metal ions [44], hetero coupling [45], the use of passivation layers [46], and defect engineering [47] among others. However, stable CuO thin-films are sometimes obtained at the expense of photo-current density. Hence, to find a balance between photo-stability and photo-current density, it is essential to first optimize the photo-current response of the CuO photocathodes prior to enhancing their photo-stability in the electrolyte [21, 48].

The processing parameters of preparing nanostructured CuO films using the sol-gel dip-coating method such as withdrawal rate, film thickness, and annealing temperature can influence the optical, structural, and photocatalytic properties of the films [49-51]. Withdrawal velocity has been found to influence the grain size [52] and thickness [49] of the films. An increasing film thickness may improve crystallinity [50], which limits the probability of electron-hole recombination, promoting efficient charge separation and migration [33, 34]. Increasing annealing temperature has also been reported to enhance the crystallinity of the films [53], which can help limit grain boundaries and improve photo-absorption for an efficient water-splitting process [33]. The influence of withdrawal rates on the PEC properties of photoelectrodes such as ZnO has been previously carried out [54]. However, a study on the influence of withdrawal velocity on the PEC response of CuO photocathodes is yet to be reported. Also, separate investigations have been conducted on the effects of film thickness [55] and calcination temperature [56] on the structural, photo-absorption, and electrical properties of dip-coated CuO films for various applications. However, a single study where withdrawal rates, calcination temperature, and the film’s thickness were optimized for dip-coated CuO photocathodes for photocatalytic water-splitting have not been reported, based on known literature. Therefore, it will be essential to first optimize the processing parameters for preparing dip-coated CuO films for the enhancement of their photo-current density during photocatalysis, prior to further modifications for improving photo-stability in electrolyte.

1.3 Aims and objectives

The aim of this dissertation is to optimize the processing parameters of dip-coated pristine CuO photocathodes to improve their photo-current response, and to enhance their photo-stability through the incorporation of activated charcoal (AC), Silver (Ag) and Gold (Au) nanoparticles (NPs) on their surface.

The objectives of this dissertation are as follows:

i. To optimize the withdrawal rate, film thickness and annealing temperature for preparing dip coated CuO thin films for PEC applications.
ii. To investigate the influence of withdrawal rate, film thickness and annealing temperature on the structural, morphological, and optical properties of dip coated CuO thin films
iii. To investigate the PEC properties of the pristine CuO films
iv. To deposit protective layers of AC, Ag and Au NPs on the pristine CuO films to improve their photo-stability in an electrolyte.
v. To investigate the influence of the surface modification of the pristine CuO films with AC, Ag and Au NPs on the structural, morphological, and optical properties of the films.
vi. To study the photo-current response and photo-stability of the CuO films modified with AC, Ag, and Au NPs.

1.4 Structure of the thesis

This dissertation is divided into five (5) chapters as follows:

Chapter 1 presents the motivation and background of the research. The aims and objectives are also given, along with the structure of the thesis.
Chapter 2 presents a review on the properties and stability of CuO as a photocathode for photoelectrochemical water-splitting.

Chapter 3 reports on the experimental methods employed in the synthesis and characterization of pristine CuO films, and the ones modified with AC, Ag, and Au NPs.

Chapter 4 discusses the results obtained from the synthesis and characterizations of the pristine CuO films, and the AC, Ag and Au modified photocathodes.

Chapter 5 presents the conclusions derived from this study and give some recommendations for future work.

References

[1] A. L. El Zein and N. A. Chehayeb, "The effect of greenhouse gases on earth's temperature," *International Journal of Environmental Monitoring and Analysis,* vol. 3, no. 2, p. 74, 2015.

[2] B. K. Bose, "Global warming: Energy, environmental pollution, and the impact of power electronics," *IEEE Industrial Electronics Magazine,* vol. 4, no. 1, pp. 6-17, 2010.

[3] R. A. Pielke Jr, C. Landsea, M. Mayfield, J. Layer, and R. Pasch, "Hurricanes and global warming," *Bulletin of the American Meteorological Society,* vol. 86, no. 11, pp. 1571-1576, 2005.

[4] J. B. Elsner, S. C. Elsner, and T. H. Jagger, "The increasing efficiency of tornado days in the United States," *Climate Dynamics,* vol. 45, no. 3, pp. 651-659, 2015.

[5] G. Shi, H. Yan, W. Zhang, J. Dodson, H. Heijnis, and M. Burrows, "Rapid warming has resulted in more wildfires in northeastern Australia," *Science of the total environment,* vol. 771, p. 144888, 2021.

[6] Z. Ardakani, F. Bartolini, and G. Brunori, "Economic modeling of climate-smart agriculture in Iran," *New Medit. Mediterranean Journal of Economics, Agriculture and Environment,* vol. 18, no. 1, pp. 29-40, 2019.

[7] K. Paustian *et al.*, "Climate change and greenhouse gas mitigation: challenges and opportunities for agriculture," *CAST Task Force Report,* vol. 141, 2004.

[8] L. Al-Ghussain, "Global warming: review on driving forces and mitigation," *Environmental Progress & Sustainable Energy,* vol. 38, no. 1, pp. 13-21, 2019.

[9] J. G. Olivier, K. Schure, and J. Peters, "Trends in global CO2 and total greenhouse gas emissions," *PBL Netherlands Environmental Assessment Agency,* vol. 5, 2017.

[10] A. Williams, "Role of fossil fuels in electricity generation and their environmental impact," *IEE Proceedings A-Science, Measurement and Technology,* vol. 140, no. 1, pp. 8-12, 1993.

[11] T. Covert, M. Greenstone, and C. R. Knittel, "Will we ever stop using fossil fuels?," *Journal of Economic Perspectives,* vol. 30, no. 1, pp. 117-38, 2016.

[12] H. Akimoto and H. Narita, "Distribution of SO2, NOx and CO2 emissions from fuel combustion and industrial activities in Asia with 1°× 1° resolution," *Atmospheric Environment,* vol. 28, no. 2, pp. 213-225, 1994.

[13] M. S. Nazir, A. J. Mahdi, M. Bilal, H. M. Sohail, N. Ali, and H. M. Iqbal, "Environmental impact and pollution-related challenges of renewable wind energy paradigm–a review," *Science of the Total Environment,* vol. 683, pp. 436-444, 2019.

[14] J. Goldemberg and S. T. Coelho, "Renewable energy—traditional biomass vs. modern biomass," *Energy Policy,* vol. 32, no. 6, pp. 711-714, 2004.

[15] A. Bahadori and C. Nwaoha, "A review on solar energy utilisation in Australia," *Renewable and Sustainable Energy Reviews,* vol. 18, pp. 1-5, 2013.

[16] Y. Kumar *et al.*, "Wind energy: Trends and enabling technologies," *Renewable and Sustainable Energy Reviews,* vol. 53, pp. 209-224, 2016.

[17] C. Gokcol, B. Dursun, B. Alboyaci, and E. Sunan, "Importance of biomass energy as alternative to other sources in Turkey," *Energy Policy,* vol. 37, no. 2, pp. 424-431, 2009.

[18] S. Sen, S. Ganguly, A. Das, J. Sen, and S. Dey, "Renewable energy scenario in India: Opportunities and challenges," *Journal of African Earth Sciences,* vol. 122, pp. 25-31, 2016.

[19] O. Khaselev and J. A. Turner, "A monolithic photovoltaic-photoelectrochemical device for hydrogen production via water splitting," *Science,* vol. 280, no. 5362, pp. 425-427, 1998.

[20] M. R. S. Shaikh, "A review paper on electricity generation from solar energy," 2017.

[21] A. Cots, P. Bonete, and R. Gómez, "Improving the stability and efficiency of CuO photocathodes for solar hydrogen production through modification with iron," *ACS applied materials & interfaces,* vol. 10, no. 31, pp. 26348-26356, 2018.

[22] Y. Tachibana, L. Vayssieres, and J. R. Durrant, "Artificial photosynthesis for solar water-splitting," *Nature Photonics,* vol. 6, no. 8, pp. 511-518, 2012.

[23] Y. Yang, S. Niu, D. Han, T. Liu, G. Wang, and Y. Li, "Progress in developing metal oxide nanomaterials for photoelectrochemical water splitting," *Advanced Energy Materials,* vol. 7, no. 19, p. 1700555, 2017.

[24] J. Nowotny *et al.*, "Towards sustainable energy. Generation of hydrogen fuel using nuclear energy," *International Journal of Hydrogen Energy,* vol. 41, no. 30, pp. 12812-12825, 2016.

[25] T. Veziro and F. Barbir, "Hydrogen: the wonder fuel," *International Journal of Hydrogen Energy,* vol. 17, no. 6, pp. 391-404, 1992.

[26] W. Anaf, O. Schalm, K. Janssens, and K. De Wael, "Understanding the (in) stability of semiconductor pigments by a thermodynamic approach," *Dyes and Pigments,* vol. 113, pp. 409-415, 2015.

[27] P. Peerakiatkhajohn, J.-H. Yun, S. Wang, and L. Wang, "Review of recent progress in unassisted photoelectrochemical water splitting: from material modification to configuration design," *Journal of Photonics for Energy,* vol. 7, no. 1, p. 012006, 2016.

[28] T. Hisatomi, J. Kubota, and K. Domen, "Recent advances in semiconductors for photocatalytic and photoelectrochemical water splitting," *Chemical Society Reviews,* vol. 43, no. 22, pp. 7520-7535, 2014.

[29] C. Li, J. He, Y. Xiao, Y. Li, and J.-J. Delaunay, "Earth-abundant Cu-based metal oxide photocathodes for photoelectrochemical water splitting," *Energy & Environmental Science,* vol. 13, no. 10, pp. 3269-3306, 2020.

[30] M. Bonomo and D. Dini, "Nanostructured p-type semiconductor electrodes and photoelectrochemistry of their reduction processes," *Energies,* vol. 9, no. 5, p. 373, 2016.

[31] S. Chen and L.-W. Wang, "Thermodynamic oxidation and reduction potentials of photocatalytic semiconductors in aqueous solution," *Chemistry of Materials,* vol. 24, no. 18, pp. 3659-3666, 2012.

[32] Z. Wang and L. Wang, "Photoelectrode for water splitting: Materials, fabrication and characterization," *Science China Materials,* vol. 61, no. 6, pp. 806-821, 2018.

[33] A. Kudo and Y. Miseki, "Heterogeneous photocatalyst materials for water splitting," *Chemical Society Reviews,* vol. 38, no. 1, pp. 253-278, 2009.

[34] J. Joy, J. Mathew, and S. C. George, "Nanomaterials for photoelectrochemical water splitting–review," *international journal of hydrogen energy,* vol. 43, no. 10, pp. 4804-4817, 2018.

[35] A. Fujishima and K. Honda, "Electrochemical photolysis of water at a semiconductor electrode," *nature,* vol. 238, no. 5358, pp. 37-38, 1972.

[36] D. Kang *et al.*, "Printed assemblies of GaAs photoelectrodes with decoupled optical and reactive interfaces for unassisted solar water splitting," *Nature Energy,* vol. 2, no. 5, pp. 1-5, 2017.

[37] I. V. Bagal *et al.*, "Cu2O as an emerging photocathode for solar water splitting-a status review," *International Journal of Hydrogen Energy,* vol. 44, no. 39, pp. 21351-21378, 2019.

[38] W. Yang and J. Moon, "Recent advances in earth-abundant photocathodes for photoelectrochemical water splitting," *ChemSusChem,* vol. 12, no. 9, pp. 1889-1899, 2019.

[39] M. S. Prévot, N. Guijarro, and K. Sivula, "Enhancing the performance of a robust sol–gel-processed p-type delafossite CuFeO2 photocathode for solar water reduction," *ChemSusChem,* vol. 8, no. 8, pp. 1359-1367, 2015.

[40] T. H. Tran and V. T. Nguyen, "Copper oxide nanomaterials prepared by solution methods, some properties, and potential applications: a brief review," *International scholarly research notices,* vol. 2014, 2014.

[41] C.-Y. Chiang, K. Aroh, N. Franson, V. R. Satsangi, S. Dass, and S. Ehrman, "Copper oxide nanoparticle made by flame spray pyrolysis for photoelectrochemical water splitting–Part II. Photoelectrochemical study," *International journal of hydrogen energy,* vol. 36, no. 24, pp. 15519-15526, 2011.

[42] Y.-F. Lim, C. S. Chua, C. J. J. Lee, and D. Chi, "Sol–gel deposited Cu 2 O and CuO thin films for photocatalytic water splitting," *Physical Chemistry Chemical Physics,* vol. 16, no. 47, pp. 25928-25934, 2014.

[43] H. Xing, E. Lei, Z. Guo, D. Zhao, X. Li, and Z. Liu, "Exposing the photocorrosion mechanism and control strategies of a CuO photocathode," *Inorganic Chemistry Frontiers,* vol. 6, no. 9, pp. 2488-2499, 2019.

[44] A. M. Ahmed, E. M. Abdalla, and M. Shaban, "Simple and low-cost synthesis of Ba-doped CuO thin films for highly efficient solar generation of hydrogen," *The Journal of Physical Chemistry C,* vol. 124, no. 41, pp. 22347-22356, 2020.

[45] H. S. Park, C.-Y. Lee, and E. Reisner, "Photoelectrochemical reduction of aqueous protons with a CuO| CuBi 2 O 4 heterojunction under visible light irradiation," *Physical Chemistry Chemical Physics,* vol. 16, no. 41, pp. 22462-22465, 2014.

[46] R. Liu, Z. Zheng, J. Spurgeon, and X. Yang, "Enhanced photoelectrochemical water-splitting performance of semiconductors by surface passivation layers," *Energy & Environmental Science,* vol. 7, no. 8, pp. 2504-2517, 2014.

[47] Z. Wang *et al.*, "Identifying copper vacancies and their role in the CuO based photocathode for water splitting," *Angewandte Chemie,* vol. 131, no. 49, pp. 17768-17773, 2019.

[48] H. Tang *et al.*, "Enhancing the stability of CuO thin-film photoelectrodes by Ti alloying," *Journal of electronic materials,* vol. 41, no. 11, pp. 3062-3067, 2012.

[49] Z. N. Kayani, A. Aslam, R. Ishaque, S. N. Zahra, H. Hanif, and H. Khan, "The effect of the withdrawal speed on properties of nickel oxide thin films," *Zeitschrift für Kristallographie-Crystalline Materials,* vol. 234, no. 10, pp. 647-655, 2019.

[50] H. B. Saâd, M. Ajili, S. Dabbabi, and N. T. Kamoun, "Investigation on thickness and annealing effects on physical properties and electrical circuit model of CuO sprayed thin films," *Superlattices and Microstructures,* vol. 142, p. 106508, 2020.

[51] R. Sathyamoorthy, C. Sharmila, K. Natarajan, and S. Velumani, "Influence of annealing on structural and optical properties of Zn3P2 thin films," *Materials characterization,* vol. 58, no. 8-9, pp. 745-749, 2007.

[52] S. Aydemir, "Effects of withdrawal speed on the microstructural and optical properties of sol–gel grown ZnO: Al thin films," *Vacuum,* vol. 120, pp. 51-58, 2015.

[53] F. A. Akgul, G. Akgul, N. Yildirim, H. E. Unalan, and R. Turan, "Influence of thermal annealing on microstructural, morphological, optical properties and surface electronic structure of copper oxide thin films," *Materials Chemistry and Physics,* vol. 147, no. 3, pp. 987-995, 2014.

[54] A. Musaa, S. Farhad, M. Gafura, and A. Jamilb, "Effects of withdrawal speeds on the structural, morphological, electrical, and optical properties of CuO thin films synthesized by dip-coating for CO2 gas sensing."

[55] S. Shariffudin, S. Khalid, N. Sahat, M. Sarah, and H. Hashim, "Preparation and characterization of nanostructured CuO thin films using sol-gel dip coating," in *IOP Conference Series: Materials Science and Engineering*, 2015, vol. 99, no. 1: IOP Publishing, p. 012007.

[56] N. Raship, M. Sahdan, F. Adriyanto, M. Nurfazliana, and A. Bakri, "Effect of annealing temperature on the properties of copper oxide films prepared by dip coating technique," in *AIP Conference Proceedings*, 2017, vol. 1788, no. 1: AIP Publishing, p. 030121.

Chapter 2

2.0. CuO photocathodes for photoelectrochemical water-splitting

2.1. Introduction

Photoelectrochemical (PEC) water-splitting is an ideal inexpensive and sustainable technique for harvesting solar energy for the production hydrogen (H_2) fuel using suitable photoelectrode materials (usually semiconducting oxides) and sunlight as the energy input. Though extensive research has been done on PEC water-splitting, some of the primary concerns preventing effective photo-electrolysis, include stability and low efficiency of photoelectrode materials. Copper Oxide (CuO) has emerged as a promising photocathode for PEC water-splitting due to its outstanding photocatalytic properties. In this chapter, we discuss the basic operation of a PEC cell, basic requirements of photoelectrode materials for PEC water-splitting, as well as CuO as a photocathode for PEC water-splitting. Furthermore, deposition techniques of CuO and the optimization of processing parameters to enhance stability and photo-current response of CuO for hydrogen production are also elaborated.

2.2. Basic operation of a PEC cell in water-splitting

The concept of water-splitting is based on the process of natural photosynthesis by green plants and photosynthetic bacteria, whereby water (H_2O) and carbon dioxide (CO_2) are converted to oxygen (O_2) and carbohydrates in the presence of sunlight to serve as food and fuel for the plant (Eq. 2.2.1), as a result converting H_2O to H_2 and O_2 (Eq. 2.2.2) [1-3].

$$6CO_2 + 6H_2O \longrightarrow C_6H_{12}O_6 + 6O_2 \quad \text{(EO = 1.43 V vs SHE)} \qquad \text{Eq. 2.2.1}$$

$$2H_2O \longrightarrow O_2 + 2H_2 \quad \text{(E = 1.23 Vs SHE)} \qquad \text{Eq. 2.2.2}$$

The redox half-reactions (hydrogen evolution reactions (HER)/oxygen evolution reactions (OER)) of Eq. 2.2.2 are presented in Eq. 2.2.3 and Eq. 2.2.4. The e^- and h^+ in Eq. 2.2.3 and 2.2.4 represent electrons and holes respectively.

$2H^{+} + 2e^{-} \longrightarrow H_2$ $(E_o = 0\ \text{V vs SHE})$ Eq. 2.2.3

$2H_2O + 4h^{+} \longrightarrow O_2 + 4H^{+}$ $(E_o = 1.23\ \text{V vs SHE})$ Eq. 2.2.4

Water-splitting is considered an eco-friendly method for producing clean and green, sustainable, and renewable hydrogen, as it utilizes direct solar energy to produce H_2 and O_2 (photo-electrolysis) [4, 5]. For photo-electrolysis to take place, a semiconductor material/photoelectrode through which solar energy will be absorbed and stored is required, is a key factor which determines the efficiency and performance of the water-splitting system [5, 6]. The overall water-splitting process consists of three primary steps which are listed below and are presented in a schematic diagram in Figure **2.2.*1***[6-10]:

- Step 1: Absorption of photons (light harvesting) – The absorption of light is associated with the generation of charge carriers and photo-voltage needed for the water-splitting process.
- Step 2: Charge separation and migration – determines the chance of electron-hole recombination as well as the amount of photoexcited charge carriers reaching the semiconductor/electrolyte interface for HER/OER. Electron-hole pairs should be efficiently separated and the photoexcited charge carriers should be rapidly transferred to semiconductor/electrolyte interface to prevent electron-hole recombination.
- Step 3: Surface reactions (HER/OER) – The oxidation of water occurs at the anode through OER, while the reduction of water occurs at the cathode through the HER. HER and OER depend on the amount of charge carriers reaching the surface of the semiconductor and the active sites on the surface of the semiconductor, if the active sites for the redox reactions are not sufficient, then the photoexcited charge carriers would have to recombine with each other, restricting the overall water-splitting process.

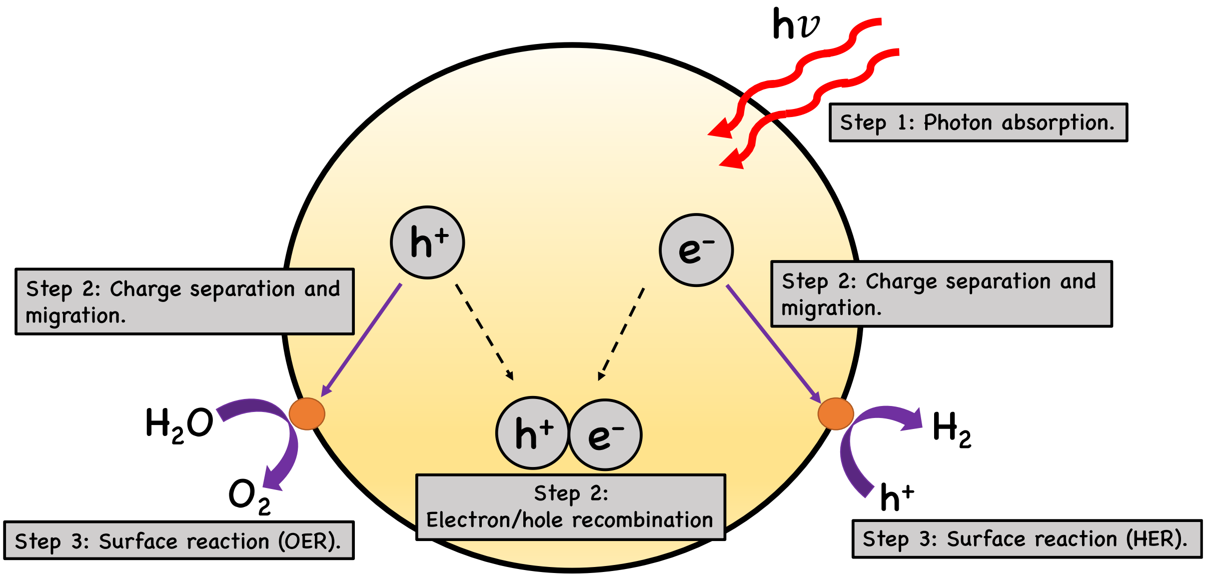

Figure 2.2.1 A schematic diagram illustrating the 3 primary steps of photocatalytic and PEC water-splitting.

Photo-electrolysis is carried out by immersing the photoelectrode in an aqueous electrolyte under illumination of light. As a result, the fermi level (E_f) of the photoelectrode and the electrolyte must equilibrate until the fermi levels are aligned and transfer of charges occurs between the photoelectrode and the electrolyte [11, 12]. For an n-type photoelectrode, photoexcited majority charge carriers (electrons) move from the valence band (VB) to the conduction band (CB), they are further transferred to the surface of the counter electrode (usually Pt) and HER takes place. Concurrently, the minority charge carriers (holes) in the VB transfer to the semiconductor/electrolyte interface where OER takes place, this is illustrated in Figure **2.2.2** (a) [9, 13]. Whereas for p-type photoelectrodes, HER and OER take place in opposite directions. Minority charge carriers (electrons) move from the electrolyte to the semiconductor/electrolyte interface for HER, while majority charge carriers (holes) move to the counter electrode to participate in OER Figure ***2.2.2*** (b) [14, 15].

Prior photo-electrolysis, ions are first absorbed in the solution by the photoelectrode, resulting in the creation of as space charge layer at the semiconductor-electrolyte interface which then forms an electric field in the region, causing the energy bending illustrated in Figure 2.2.2. The absorbed ions at the photoelectrode and the ones near the surface of the electrode also forms a region generally termed as the Helmholtz layer. In the space charge region, there exist an electric field which is essential for the bending of bands, separating the photoexcited electrons from holes and supressing electron-hole recombination. The upward/downward bending of bands depend on the upward/downward movement of the electrons based on the n-type/p-type nature of the photoelectrode materials (Figure **2.2.*3*** (a) and (b)). For an n-type photoelectrode, the space charge region is called the depletion region due to the depleted electrons and excess holes, for a p-type photoelectrode it is called the accumulation region due to the accumulation of electrons [11, 16, 17].

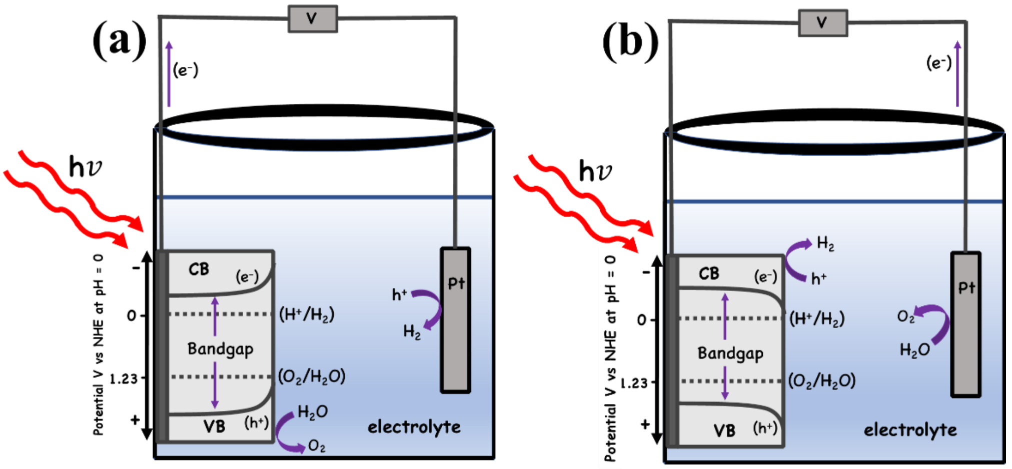

Figure 2.2.2 Schematic illustration of one-step photosystem of **(a)** n-type and **(b)** p-type photoelectrodes for PEC water-splitting.

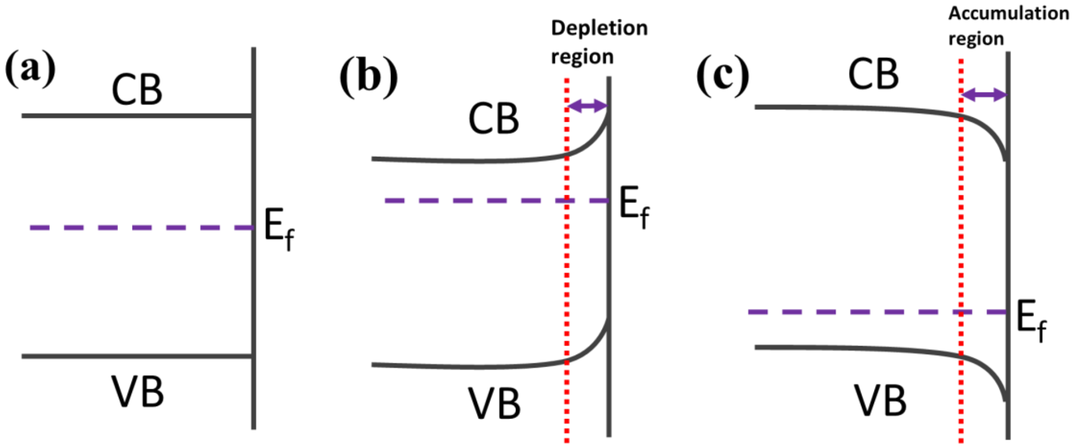

Figure 2.2.3 Schematic diagram illustrating band structure resulting from the fermi-energy level of an (a) intrinsic (b) n-type and (c) p-type semiconductor.

If two photoelectrodes (n-type and p-type) are used instead of a counter electrode, a p-n heterojunction or a z-scheme system is utilized for PEC water-splitting, also called hetero-coupling (Figure **2.2.*4*** (c) and (d)) [13, 18]**.** For a p-n heterojunction, the photoexcited electrons move from the photoelectrode with the higher CB to the one with lower CB, participating in HER on the surface of CB. OER occurs simultaneously when photoexcited holes are promoted from the photoelectrode with the lower VB to the one with higher VB, according to Peerakiatkhajohn *et. al 2016* this is a result of accumulated potential on the solid/liquid interface [13]. Whereas for the z-scheme, HER occurs at the photoelectrode with the higher CB and OER at the one with the lower VB. The two-step photosystem mostly preferred is the z-scheme approach since it requires less energy for photo-electrolysis due to the wider range of visible light absorption [9, 12].

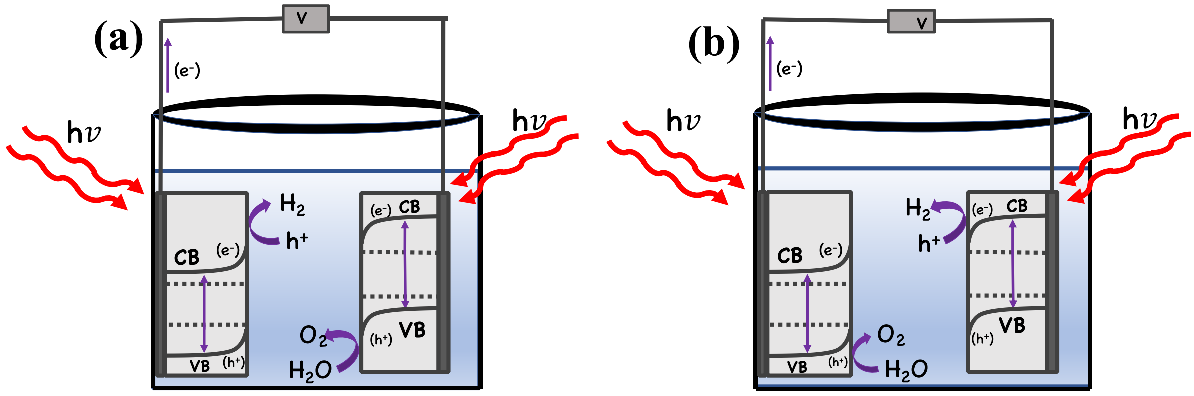

Figure 2.2.4 Schematic illustration of a **(a)** p-n junction diode **(b)** z-scheme approach for PEC water-splitting.

2.3. Basic requirements of a photoelectrode material for Photoelectrochemical water-splitting

For spontaneous water-splitting reaction to take place, an ideal photoelectrode/semiconductor material is immersed in an aqueous electrolyte under irradiation of light. A photoelectrode which is suitable for PEC water-splitting should possess the following properties: It should have a small bandgap (E_g) [4], suitable band-edge positions [7], short carrier diffusion length [4], high crystallinity [12] and it should be stable under aqueous solutions [19], respectively.

2.3.1. Bandgap and band-edge positions

The photoelectrode must have a small Eg (1.6 – 2.2 eV) to absorb a wide range of solar radiation in the visible region. If the energy of the incident light is greater than the energy of the band gap (Eg), it ensures the generation and separation of electron-hole pairs in the valence and conduction bands with sufficient potentials for water-splitting [4, 7]. The conduction band of the photoelectrode material should be higher than the reduction potential of water (H^+/H_2), which is +0 V vs normal hydrogen electrode (NHE) and the valence band energy should be lower than the oxidation potential of water (O_2/H_2O), which is -1.23 V vs NHE at pH=0, implying that the bandgap of the photoelectrode must straddle (H^+/H_2) and (O_2/H_2O). Metal oxides such as CuO, $BiVO_4$, ZnO etc. [6] have bandgaps and band-edge positions which are suitable for PEC water-splitting. Figure **2.3.*1*** exhibits bandgaps and reduction and oxidation potentials of n-type and p-type semiconductors.

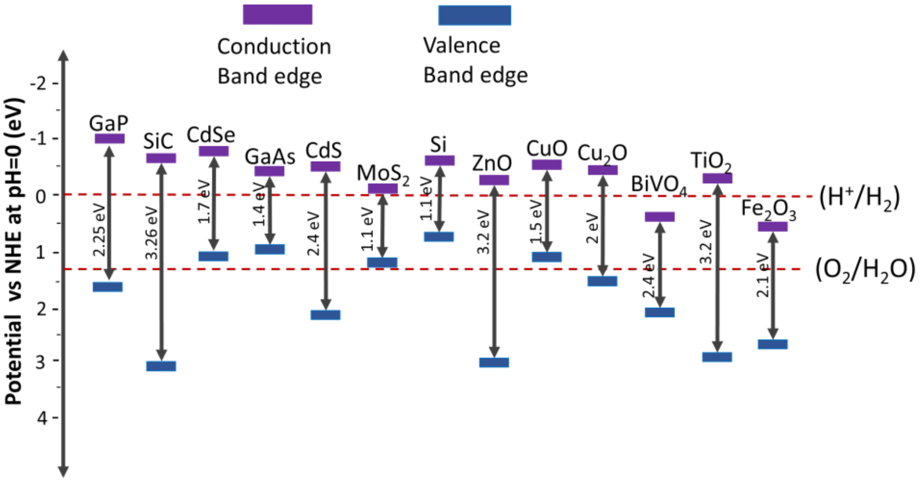

Figure 2.3.1 Diagram representation of redox potentials and band structures of n-type and p-type semiconductors.

2.3.2. Surface area and diffusion length

A large surface area and a long diffusion length close to the solid/liquid interface are also essential to ensure efficient transfer of separated photogenerated charge carriers to their respective reaction sites [4, 20]. Furthermore, the particle/grain sizes must be large, to reduce the number of grain boundaries which function as trapping centres for electron-hole recombination [7, 21]. Semiconductors such as TiO_2 [20], CuO [22], α-Fe_2O_3 [23] have the potential to become well performing photoelectrodes for water-splitting, however their short diffusion length promotes rapid electron-hole recombination, limiting their PEC performance.

2.3.3. Effective charge transfer and separation

Charge transport and separation is vital for the performance of photoelectrodes for PEC applications. The process involves the separation of electron-hole pairs, followed by the rapid transfer of charge carriers between the photoelectrode and the electrolyte for HER/OER depending on the p-type/n-type nature of the material [24, 25]. It is facilitated by a potential barrier that is formed at the solid/liquid interface when a photoelectrode is in contact with an aqueous electrolyte under irradiation of light. The separation of electrons from holes is important for reducing the rate of recombination, whereas the transfer of charges is vital for the charging of the surface of the photoelectrode [17, 25].

2.3.4. Stability in aqueous electrolytes

A photoelectrode should be stable in aqueous solutions to prevent corrosion [26]. Photo-corrosion occurs when the photoelectrode is oxidized/reduced instead of water. For n-type photoelectrodes, photo-corrosion depends on the thermodynamic oxidation potential of the photoelectrode (φ^{ox}) in relation to O_2/H_2O, which occurs when φ^{ox} is higher than O_2/H_2O or it's VB, referred to as anodic photo-corrosion due to the n-type nature of the material. On the contrary, photo-corrosion of p-type photoelectrodes depends on the thermodynamic reduction potential of the photoelectrode (φ^{red}) in relation to H^+/H_2, which occurs when Φ^{red} is lower than H^+/H_2 or it's CB, called cathodic photo-corrosion due to the p-type nature of the material [19, 27, 28], Figure **2.3.*2*** (a) and (b) shows the φ^{ox} and φ^{red} positions of n-type and p-type photoelectrodes which are stable under aqueous electrolytes. While photoelectrodes such as TiO_2 and α-Fe_2O_3 are stable under aqueous electrolytes [29, 30], Others such as CuO and Cu_2O are prone to photo-corrosion in aqueous solutions, resulting in moderate photo-current densities [31, 32].

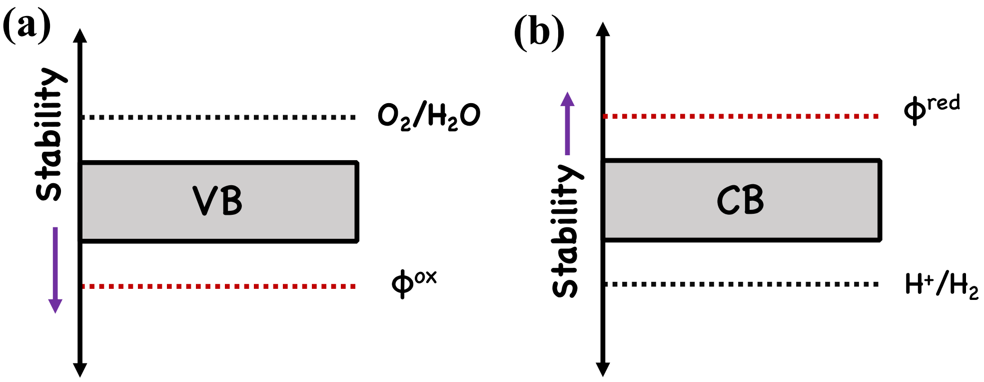

Figure 2.3.2 Diagram illustration of increasing stability for **(a)** an n-type **(b)** p-type photoelectrode.

2.4. CuO as a photocathode for PEC water-splitting

CuO is the most stable phase of copper oxides (i.e., Cu_2O and Cu_4O_3), it is also a p-type, non-toxic semiconductor which exists in three crystalline polymorphs namely, tetragonal [33], cubic [34], and monoclinic phases [35]. Among other p-type semiconductors such Sb_2Se_3 [36], Si [37] and Cr_2O_3 [38], CuO semiconductors have emerged to be promising photocathodes for PEC applications due to the narrow bandgap (1.4 – 2.1 eV) [39], suitable band-edge positions [40], as well as low cost and abundance of the copper element [41] respectively.

One of the pioneering investigations on CuO as a photocathode for PEC applications was reported by Koffyberg *et. al, 1982* [42]. Since then, CuO photocathodes have been modified to improve their PEC properties for efficient water-splitting. For example, in 2000, Yoon *et. al* investigated photoelectrochemical properties of copper oxide thin films coated on a *n*-Si substrate in relation to deposition temperature [43]. In 2004, Chaudhary *et. al*, studied the PEC properties of CuO thin films by varying the deposition temperature and spray time using spray pyrolysis on FTO substrates. In 2012 Tang *et. al*, investigated the stability enhancement of CuO thin-film photoelectrodes by Ti-Alloying [44]. Also, in 2019 Wang *et. al*, reported the identification of copper vacancies and their role in the CuO based photocathode for water-splitting [45].

2.5. Crystal structure of CuO

2.5.1. Tetragonal CuO

Unlike the monoclinic CuO, tetragonal and cubic phases of CuO are rock-salt structures which are more symmetrical, hence they have the potential to be high temperature superconductors [33, 46]. Tetragonal (elongated rock-salt) CuO consists of inter-penetrating corner sub-lattices of CuO$_2$ (Figure **2.5.*1***) which form infinite CuO planes along the c-axis, this results in two anti-ferromagnetic ground states which are shown in the right side of Figure **2.5.*1*** [47-49]. The anti-ferromagnetic interactions form at Néel temperatures ranging from 600 -1000 K [33, 50]. Tetragonal CuO has not been found in nature, however it has been epitaxially grown on SrTiO$_3$ substrates in a form of thin films [47, 51].

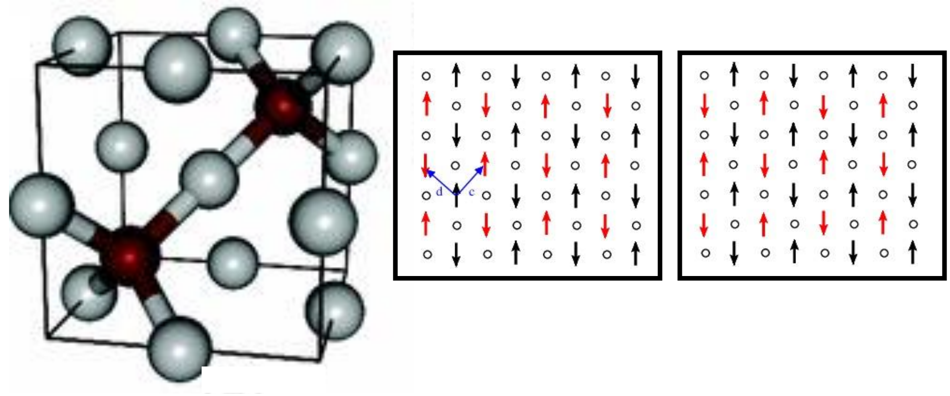

Figure 2.5.1 Crystal structure of Tetragonal CuO.
Red: Oxygen atoms, Grey: Copper atoms, Arrows: Anti-ferromagnetic moments [52]

2.5.2. Cubic CuO

Among the three polymorphs of CuO, the cubic phase has emerged the most structurally and electronically symmetrical. Furthermore, it is metastable, thus it can be converted to monoclinic phase at elevated temperatures [34]. Cubic CuO has also not been found in nature, however Shi *et. al, 2017* reported the first pure cubic phase which was successfully synthesized on an alumina substrate using Cu(acac)$_2$ as a precursor [34]. The unit cell is face-centred and consists of two Copper and two oxygen atoms situated at the edges of the cell with lattice parameters, $a = b = c = 4.245$ Å, $\alpha = \beta = \gamma = 90°$ (Figure **2.5.*2***), has anti-ferromagnetic interactions which form at low Néel temperatures of 600 K [50, 53-55].

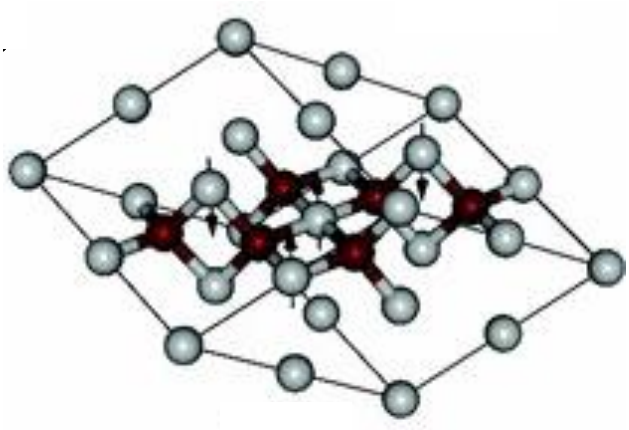

Figure 2.5.2 Crystal structure of Cubic CuO.

Red: Oxygen atoms, Grey: Copper atoms, Arrows: Anti-ferromagnetic moments [52]

2.5.3. Monoclinic CuO

Monoclinic CuO is the least stable phase of CuO and belongs to the space group *C2/c*, with lattice constants *a* = 4.6837 Å, *b* = 3.4226 Å, *c* = 5.1288 Å, and β = 99.54°. The copper atoms in the monoclinic phase are attached to four oxygen atoms located at the edges of a rectangular parallelogram, occupying the symmetry site 4(c) where (x, y, z) = (0.25, 0.25, 0), whereas the oxygen atom is co-ordinated to four carbon atoms located at the edges of a distorted tetrahedron (Figure **2.5.*3***), occupying the 4(e)-symmetry site where (x, y, z) = (0, 0.57, 0.25). The atoms form strong one-dimensional anti-ferromagnetic interactions through the super-exchange paths Cu-O-Cu (θ = ~146°) at a low Néel temperature of 231 K, and diminish above 550 K along the [$10\bar{1}$] direction [35, 52, 56-58]. The reduced Néel temperature is influenced by Jahn-Teller structural distortion which stabilizes the monoclinic ground state. Ferromagnetism is associated with the configuration of Cu^{2+} and O^{2-} in a crystal lattice which results in a single unpaired *d*-electron, inducing magnetic moments and Jahn-Teller structural distortion [59-61]. Magnetic moments of monoclinic CuO are indicated by arrows in Figure **2.5.*3***. It has been extensively investigated more than the other phases due to its wide range of applications as an active catalyst [62], gas sensor [63], supercapacitor [64], photoelectrode [31], superconductor [65] as well as a magnetic and field emission material [66]. As a result, it has fabricated using different techniques to improve charge transfer and migration as well as redox reactions at the surface.

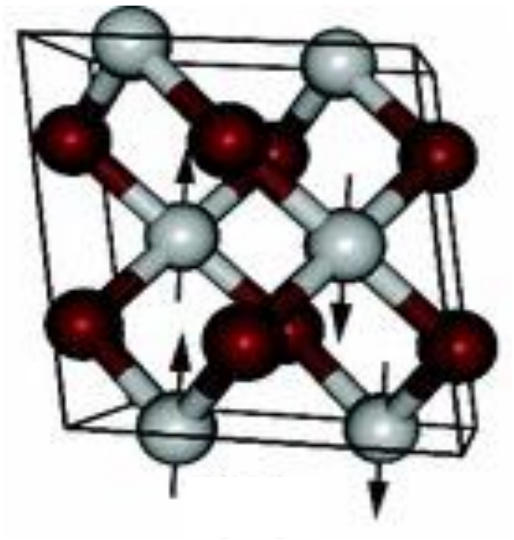

Figure 2.5.3 Crystal structures of monoclinic CuO.

Red: Oxygen atoms, Grey: Copper atoms, Arrows: Anti-ferromagnetic moments [52]

2.6. CuO Deposition techniques for PEC water-splitting

2.6.1. Sol-gel dip-coating

Sol-gel dip-coating is a simple, inexpensive technique used to fabricate thin films for PEC water-splitting by uniformly coating the substrate over large surface areas [67, 68]. The coating process involves dipping, withdrawing and drying the thin films. In detail, the substrate is vertically dipped into the precursor at constant speed and coated for a certain period of time (Figure **2.6.*1*** (a) and (b)), the coated substrate is then withdrawn from the precursor (Figure **2.6.*1*** (c)) and further dried by heat treatment to evaporate the solvent and to induce crystallization (Figure **2.6.*1*** (d)) [69, 70]. The deposition time, withdrawal speed and drying stages are essential for determining the structural and morphological properties of the films [68]. Toupin et. al, 2019 reported CuO thin films deposited via sol–gel dip-coating. The films were further subjected to heat treatment and the pure phase was obtained at temperatures higher than 360 °C in air. The films yielded photo-current response of -0.94 mA cm^{-2} at 0 V vs. RHE when annealed at 400 °C in air [67].

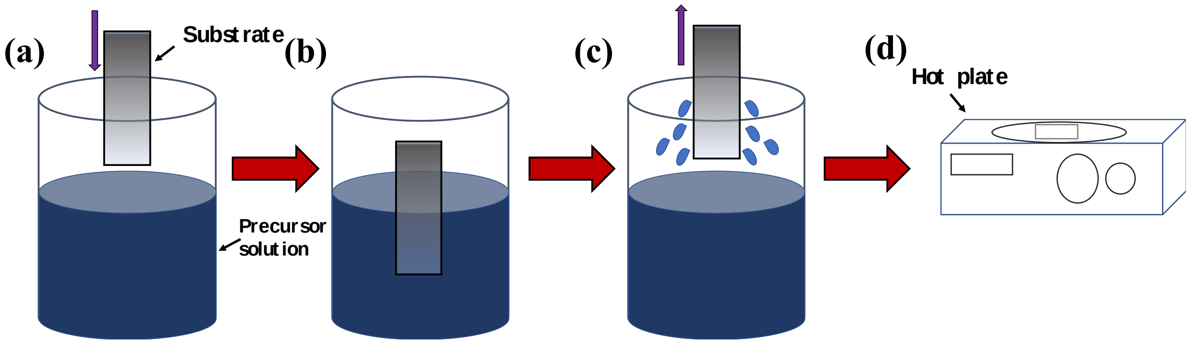

Figure 2.6.1 Deposition process of sol-gel dip-coating: **(a)** Dipping **(b)** Deposition **(c)** Withdrawal **(d)** Drying of the substrate.

2.6.2. Spin coating

Spin coating is a fast, low cost and less hazardous technique which is commonly used to uniformly fabricate thin films on flat substrates for PEC applications. A typical spin coating process includes depositing a small portion of the precursor on the substrate centre (Figure **2.6.*2*** (a)), and then spinning it at a constant high speed for a certain period of time, allowing uniform coating over the surface (Figure **2.6.*2*** (b)). Lastly, the solvent undergoes evaporation, and the desired material is left on the substrate (Figure **2.6.*2*** (c)). The films may be subjected to heat treatment for further drying and crystallization. This process may be repeated a few times to obtain the desired film thickness [41, 68, 71]. The viscosity of the precursor, rotational speed, and drying rate may influence the structural, morphological, and PEC properties of the films. Lim *et. al, 2014* successfully fabricated a pure phase of CuO thin film via spin coating. The film was used as a photocathode for PEC water-splitting, it achieved a photo-current response of -0.35 mA cm^{-2} at 0.05 V *vs.* RHE [41].

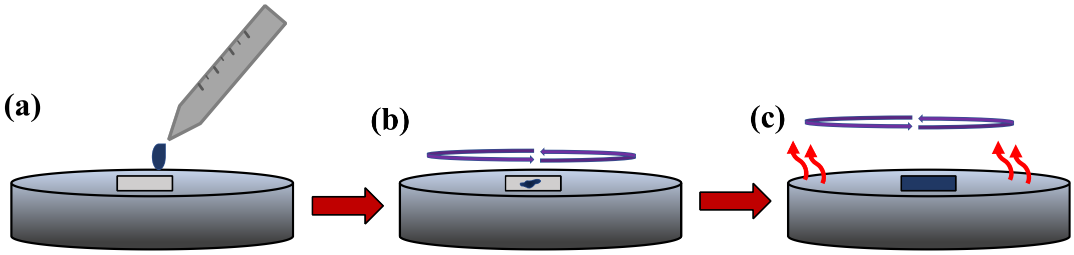

Figure 2.6.2 Schematic presentation of spin-coating: **(a)** Deposition **(b)** Spinning **(c)** Evaporation.

2.6.3. Spray pyrolysis

Spray pyrolysis is an easy, cost effective, contact free technique which is used to prepare films of any composition, from a small-scale laboratory to large-scale industries [68, 72]. The films may be used as fuel cells, or solar cells for PEC applications [72]. A spray pyrolysis method involves spraying a precursor solution on a substrate that is placed on a heated hot plate using a spray nozzle [73] (Figure **2.6.*3***). The temperature of the substrate, as well as the momentum of the droplets, influences the impact of the droplets onto the surface, which in turn affects the spreading and distribution of the precursor solution onto the substrate [72]. Hence, to obtain good quality thin films for PEC water-splitting using spray pyrolysis, processing parameters such as the temperature of the substrate, concentration of the precursor solution and the spray rate may be optimized [74]. Patel *et. al, 2016* synthesized highly photoactive and photo-stable spray pyrolyzed Tenorite CuO thin films for PEC applications, and the films yielded a high photo-current response of 24 mA/cm^{-2} at 0.25 V vs. RHE after the addition of $K_3Fe(CN)_6$ into the electrolyte [75].

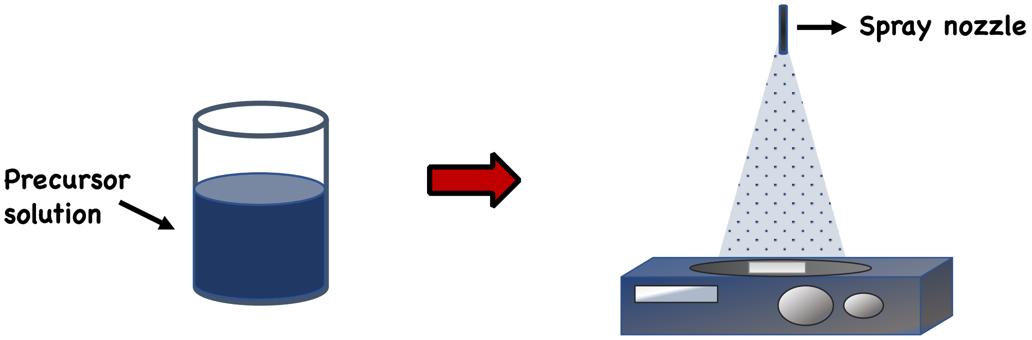

Figure 2.6.3 Schematic diagram of spray pyrolysis.

2.6.4. Successive Ionic Layer Adsorption and Reaction (SILAR)

SILAR is an easy technique which is suitable for deposition over large surface areas, it is based on the adsorption and reaction of ions from differently placed cationic and anionic precursor solutions at room temperature. The coating process involves adsorption of the cations on the surface through the immersion of the substrate in the cationic solution (Figure **2.6.*4*** (a)), resulting in the formation of the Helmholtz electric double layer. This is followed by rinsing of the excess solution with deionized water to remove any excess unreacted ions (Figure **2.6.*4*** (b)). The coated substrate is further immersed in the anionic solution, where the anions react with the cations from the cationic solution to form a solid substance on the surface (Figure **2.6.*4*** (c)). Lastly, the excess product is rinsed again with deionized water (Figure **2.6.*4*** (d)) [76-78].

As a technique which function under low temperatures, it has a significant advantage of also preventing oxidation and corrosion of the substrate. The optimization of the deposition and rinsing time, as well as the concentration and pH of the precursors may be required to obtain good quality thin films [77, 78]. Dubale *et. al, 2016* synthesized a highly photoactive Cu_2O/CuO heterostructure which was modified with CuS via SILAR. The optimized $Cu_2O/CuO/CuS$ photocathode achieved an enhanced photo-current density of -5.4 mA cm^{-2} at 0 V *vs.*RHE, which is 2.5 times more than that of bare Cu_2O/CuO under illumination.

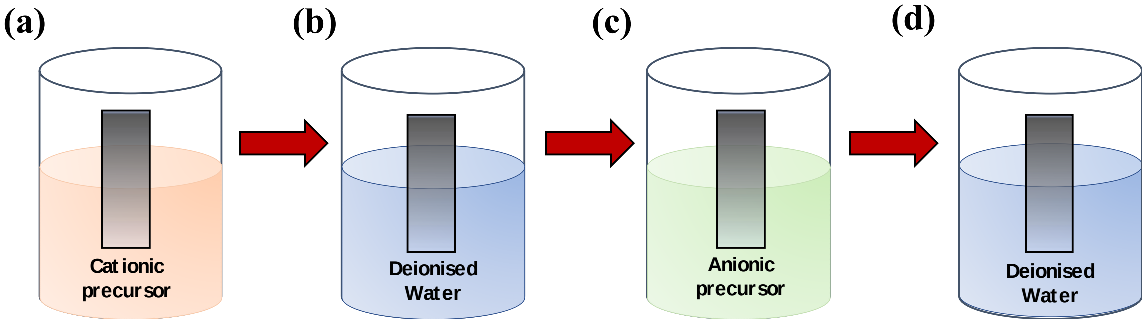

Figure 2.6.4 Schematic presentation of SILAR: **(a)** Deposition of cationic solution **(b)** 1st Rinse **(c)** Deposition of anionic solution **(d)** 2nd rinse

2.6.5. Magnetron sputtering

Magnetron sputtering is a physical vapor deposition technique which is known for producing high purity thin films at high deposition speeds and uniform coating over substrates which are sensitive to heat or possess large surface areas [79]. The coating process involves high-energy particles of a material which are bombarded onto the surface of a substrate through applied electric potential (Figure **2.6.5**). If the incident kinetic energy with which the particles strike the surface is less than the binding energy of the surface particles, it is likely that they will get reflected or absorbed on the surface. Whereas if the incident energy is greater than the binding energy (~10-20 eV), the particles may be sputtered from the surface. This process is performed under vacuum to maintain the high energies of the particles and to prevent too many collisions between particles [79-81]. To obtain good quality thin films, deposition rate, distance to the substrate, sputtering power etc. may be optimized. Masudy-Panah *et. al, 2016* reported a sputter-grown CuO thin film which was used as a photocathode for PEC water-splitting. The film showed photo-current response of ~0.92 $mAcm^{-2}$ at 0 V vs RHE, which increased to ~2.5 $mAcm^{-2}$ at 0 V vs RHE due to an increase in film thickness.

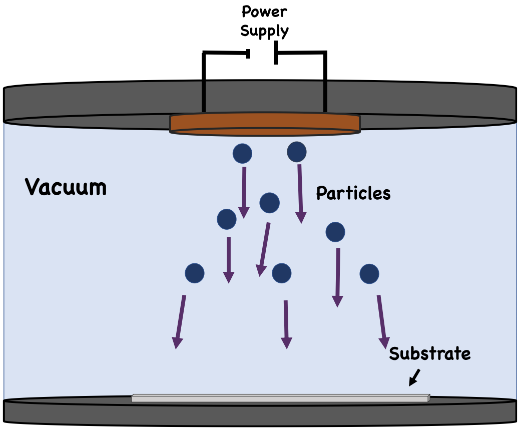

Figure 2.6.5 Schematic diagram of magnetron sputtering.

2.6.6. Drop-casting

Drop-casting is an inexpensive, easily controlled coating technique which does not require any expensive equipment for deposition. It involves dropping a precursor solution onto the surface of the substrate (Figure **2.6.6** (a) and (b)), followed by drying of the films through heat treatment (Figure **2.6.6** (c)) [82]. Unlike the above-mentioned deposition techniques, the application of drop-casting is limited to a small area and is typically used to coat over photoelectrodes to modify their properties [82, 83]. The quality of the films relies on the size, release and spread of the droplet, as well as the direction in which the drop is deposited. The density and viscosity of the precursor also play a role in determining the outcome of the films [82-84]. Park *et. al, 2014* investigated Pt-coated $CuO/CuBi_2O_4$ heterojunction which was synthesized by drop-casting for hydrogen production. The $FTO/CuO/CuBi_2O_4/Pt$ photocathode produced photo-currents of 100 and 80 mA cm^2 which were twice as much as FTO/CuO/Pt and $FTO/CuBi_2O_4/Pt$. The photocathode retained 60% of the photo-current after 20 min of chronoamperometry measurements [85].

Figure 2.6.6 Schematic diagram of a drop casting technique: **(a)** Dropping **(b)** Droplet on top of a substrate **(c)** Drying.

2.7. Optimization of processing parameters of dip-coated CuO as a photocathode for PEC water- splitting

The sol-gel dip coating method stands out among many other film deposition techniques due to its low processing cost, ease of processing, composition control, as well as its ability to form uniform films on substrates with large surface areas. Many processing parameters for preparing dip-coated CuO films can be optimized for enhancement of PEC reactions. These parameters are discussed in this section.

2.7.1. Withdrawal speed

Withdrawal speed of the substrate is a processing parameter which is typically optimized in deposition techniques which involve the vertical withdrawal of the substrate from the precursor solution at constant speed, as shown in Figure **2.6.*1*** (c) [69]. Sol-gel dip-coating [86] and SILAR [78] are good examples of methods which include this parameter. Withdrawal speed influences the film thickness of the films because of the viscous drag between the precursor and the substrate. Increased withdrawal speeds of the substrates result in thicker films which take a longer period to dry. Thus, by optimizing withdrawal speed, the surface area, porosity and crystallinity of the films may be tuned, enhancing morphological properties for PEC applications [69, 86, 87]. The effect of withdrawal speed on PEC properties of photoelectrodes such as ZnO [86], NiO [88], TiO_2 [89] have been studied, however a study on the influence of withdrawal speed on CuO photocathodes for PEC applications is yet to be reported.

2.7.2. Film Thickness

The thickness of the film is a processing parameter which can be optimized through the utilization of any other deposition technique for PEC water-splitting. For example, film thickness can be increased by performing multiple deposition cycles on the substrate using SILAR [90], by increasing the volume of the precursor solution by spray pyrolysis [91], or by increasing the withdrawal speed of the substrate by sol-gel dip-coating [69] etc. Increased film thickness is a parameter is well known for its significant influence on the crystallization, absorbance and transmittance, surface morphology and resistivity of thin films, which makes it essential for enhancing PEC properties [90-92]. Saad *et. al*, *2020* reported crystalline CuO films which were synthesized by spray pyrolysis, the films were highly absorbing as a result of the declined bandgap (1.63 - 1.52 eV), they further showed low resistivity at elevated film thicknesses [91]. Similarly, Akaltun, *2015* reported SILAR-grown CuO thin films which were crystalline and highly absorbing due to the decreased bandgap (2.03 - 1.79 eV) for the film with the optimum thickness of 310 nm [90].

2.7.3. Annealing temperature

Annealing is a post-deposition heat treatment which plays an important role in crystallinity and morphology of thin films. The ideal annealing temperature for thin films depend on conditions in which the films were grown, such as the gaseous environment during the annealing process or the above-mentioned processing parameters and deposition techniques. Some thin films may contain mixed phases prior to annealing or at higher/lower annealing temperatures, while some may change morphology [93-96]. For instance, Johan *et. al, 2011* chemically deposited CuO thin films on glass substrates and further annealed them from 200 – 400 °C in air. The films annealed at 200 °C showed a Cu_2O composition, whereas those annealed at 300 °C revealed mixed phases of CuO and Cu_2O. Furthermore, those annealed at 400 °C were completely converted CuO [93].

2.7.4. Period of deposition on the substrate

The period of deposition is typically known to influence the film thickness [97], morphology [98] and crystallinity [99] of thin films. It can either be the period of spraying for deposition techniques which utilize the spraying effect or immersion period for those that use the immersion effect [98, 99]. An increase in the time of deposition result in an increase in the density and size of the particles which is associated with the thickness of the films, this may be due to an increase in the surface area during the deposition [97]. Yaw *et. al, 2016* studied the effect of deposition time on the photoelectrochemical properties of CuO thin films synthesized via electrodeposition method. The CuO films produced photo-current of up to 0.23 mA/cm^2 at - 0.3 V (versus Ag/AgCl) when deposited for 15 minutes. Beyond 15 minutes, photo-current density declined because of the optimum film thickness reached, where the penetration of light decreases [100].

2.7.5. Concentration of the precursor

Similar to the above-mentioned processing parameters, the concentration of the precursor solution has a significant influence on the structural, morphological and optical properties of thin films for PEC applications. Increasing concentrations can enhance the crystallinity, change crystal orientation, morphology and increase the film thickness, as well as the photo-absorption of the films [101-103]. This may be attributed to the increasing number of particles, which result in increasing film thickness, consequently increasing optical absorbance and crystal size [104]. Kushwaha *et. al, 2017* tailored the morphology of a CuO photocathode using aqueous solution technique for enhanced visible light driven water-splitting. The CuO-nanoleaves showed photo-current response of 1.5 mA/cm^2, whereas the CuO-nanosheets yielded photo-current of 1.1 mA/cm^2 at 0 V v/s RHE, respectively.

2.8. Stability of CuO photocathodes under aqueous electrolytes for hydrogen production

The primary challenge of utilizing CuO as a photocathode for hydrogen evolution is the poor photo-stability in aqueous solutions, also it is prone to photo-corrosion as a consequence of self-reduction by photo-excited electrons [105, 106]. Over the years, strategies have been implemented to improve the stability and photo-current response of CuO for large scale PEC applications, these include doping of metal/non-metal ions [107], hetero-coupling [85], passivation layers [108] and defect engineering (nano-structuring) [45], respectively. Notably, stable CuO thin-films are typically obtained at the expense of photo-current density, hence to find a balance between stability and photo-current response, photoelectrodes may need to be optimized prior to performing stability tests [44, 105].

2.8.1. Doping of metal/non-metal ions

Doping is the introduction a foreign ion to a crystal lattice of a host material, the dopants form donor/acceptor energy levels in the bandgaps of the host materials, depending on whether the host is n-type or p-type [7, 11]. These energy levels can drastically reduce the photocatalytic activity of semiconductors by working as recombination centres for the photoexcited charge carriers, however if a suitable dopant is chosen it can improve the stability as well as the conductivity of the semiconductor by extending the lifetime of photogenerated charge carriers, enhancing charge transfer and migration and narrowing the bandgap for enhanced photo-absorption [7, 109].

Ahmed *et. al. 2020* reported a 2% Ba-doped CuO thin film via SILAR for solar generation of hydrogen, the film showed long-term stability at a photo-current density of 17 mA/ cm^2 at -1 V, which was 3.5 times that of the bare CuO films [107]. Tang *et. al, 2012* incorporated Ti into CuO and CuO/CuO thin films to enhance stability for PEC water-splitting. The Ti-alloyed CuO displayed improvement in photo-stability and no photo-corrosion for a time-scan of 2hrs, however photo-current density declined by 80% due to nonradiative recombination centres introduced by doping. Whereas the Ti-alloyed CuO/CuO films displayed improvement in stability with no significant decline in photo-current density [44].

2.8.2. Hetero-coupling

Hetero-coupling of two or more semiconductors is commonly utilized to limit electron-hole recombination, as well as isolating reaction sites on the surface of the photoelectrodes through the separation of electrons and holes into different compartments [10, 18]. The charge separation is caused by the electric field which is formed at the interface of the P-N junction, furthermore the bandgap of the formed heterojunction is able to increase photo-absorption in the visible region [24]. Examples of heterostructures are shown in Figure **2.2.4** (a) and (b). Tsege *et. al, 2018* fabricated a CuO/ZnO nanowire heterojunction for PEC water-splitting, the prepared photocathode yielded an enhanced photo-current density of -8.1 mA/cm^2 at 0 vs RHE. 69% of the photo-current density was retained under illumination of light, the CuO/ZnO photocathode was 1.46 times more stable than an intrinsic CuO photocathode [110]. Also, Xing et. al, 2019 synthesized a CuO/TiO_2/Pt photocathode for photoelectrochemical water-splitting. The photocathode showed a photo-current response of −0.75 mA cm^{-2} at −0.55 V vs. Ag/AgCl, it also retained stability of 84% after a stability test of 2 hours [106].

2.8.3. Passivation/protective layers

Photoelectrodes can be encapsulated with protective layers to prevent photo-corrosion and improve photo-stability in aqueous electrolytes [108]. Moreover, they can prevent the occurrence of charge recombination states within the bandgap [111], they can function as catalysts for HER/OER at the solid/liquid interface [112], Lastly they can shift the band positions of the photoelectrode relative to the electrolyte [113]. The layers should be inexpensive, easily synthesized, thin enough to permit transfer of charges between the semiconductor and the electrolyte and thick enough to prevent corrosion from the aqueous electrolyte, furthermore they must not destroy the semiconductor-electrolyte junction, respectively [108]. For example, Xing et. al, 2019 synthesized a CuO/Al photocathode which was subjected to a spontaneous oxidation process in air to form a Al_2O_3 passivation layer. The resulting photo-current density was 1.9 times higher than that of pure CuO with photo-stability of 89.5 % after 1 hour [114]. Kunturu et.al, 2019 reported carbon coated Cu_2O and Cu_2O/CuO photocathodes which showed improved photo-current densities of 6.5 and 7.5 mA/cm^{-2} at 0 and −0.1 V vs RHE potentials, furthermore the photocathodes were stable for 50h at 0.3 V vs RHE [115].

2.8.4. Defect engineering (nano-structuring)

Nano-structuring is typically used to improve the stability [116], photo-absorption [117], charge separation and migration [118] and bandgap tuning [119] of photoelectrodes for optimized PEC performance. Nano-structuring can however result in a slow charge transport process, increasing the chances of charge recombination. To overcome these limitations, 1D (nanowires, nanorods, nanotubes) [120], 2D (group III-V semiconductors) [121], 3D (integrated 1D or 2D nanostructures) [122] nanostructures as well as co-catalysts [106], plasmonic nanoparticles [123] and quantum dots [124] have been incorporated or loaded on the surface of the semiconductors, respectively. Zhao *et. al, 2014* synthesized CuO nanowire arrays which were decorated by Ag nanoparticles for enhanced PEC water-splitting, the photo-current response of the photocathodes were four times the photo-current of bare CuO nanowire arrays under the same conditions, also the photocathodes showed stability after 300s [123]. Masudy-Panah *et. al, 2017* fabricated CuO photocathodes which were further deposited with gold-palladium (Au-Pd) nanoparticles on the surface, the prepared photocathodes showed ~ 25% improvement in the photo-current density, as well as enhanced photo-stability of ~90% for 20 minutes, respectively [125].

References

[1] A. J. Bard and M. A. Fox, "Artificial photosynthesis: solar splitting of water to hydrogen and oxygen," *Accounts of Chemical Research,* vol. 28, no. 3, pp. 141-145, 1995.

[2] T. J. Meyer, "Chemical approaches to artificial photosynthesis," *Accounts of Chemical Research,* vol. 22, no. 5, pp. 163-170, 1989.

[3] M. G. Walter *et al.*, "Solar water splitting cells," *Chemical reviews,* vol. 110, no. 11, pp. 6446-6473, 2010.

[4] Z. Wang and L. Wang, "Photoelectrode for water splitting: Materials, fabrication and characterization," *Science China Materials,* vol. 61, no. 6, pp. 806-821, 2018.

[5] Z. Guo and Z. Liu, "Synthesis and control strategies of nanomaterials for photoelectrochemical water splitting," *Dalton Transactions,* vol. 50, no. 6, pp. 1983-1989, 2021.

[6] Y. Yang, S. Niu, D. Han, T. Liu, G. Wang, and Y. Li, "Progress in developing metal oxide nanomaterials for photoelectrochemical water splitting," *Advanced Energy Materials,* vol. 7, no. 19, p. 1700555, 2017.

[7] A. Kudo and Y. Miseki, "Heterogeneous photocatalyst materials for water splitting," *Chemical Society Reviews,* vol. 38, no. 1, pp. 253-278, 2009.

[8] Z. Wang and L. Wang, "Progress in designing effective photoelectrodes for solar water splitting," *Chinese Journal of Catalysis,* vol. 39, no. 3, pp. 369-378, 2018.

[9] T. Hisatomi, J. Kubota, and K. Domen, "Recent advances in semiconductors for photocatalytic and photoelectrochemical water splitting," *Chemical Society Reviews,* vol. 43, no. 22, pp. 7520-7535, 2014.

[10] H. Wang *et al.*, "Semiconductor heterojunction photocatalysts: design, construction, and photocatalytic performances," *Chemical Society Reviews,* vol. 43, no. 15, pp. 5234-5244, 2014.

[11] W. Anaf, O. Schalm, K. Janssens, and K. De Wael, "Understanding the (in) stability of semiconductor pigments by a thermodynamic approach," *Dyes and Pigments,* vol. 113, pp. 409-415, 2015.

[12] J. Joy, J. Mathew, and S. C. George, "Nanomaterials for photoelectrochemical water splitting–review," *international journal of hydrogen energy,* vol. 43, no. 10, pp. 4804-4817, 2018.

[13] P. Peerakiatkhajohn, J.-H. Yun, S. Wang, and L. Wang, "Review of recent progress in unassisted photoelectrochemical water splitting: from material modification to configuration design," *Journal of Photonics for Energy,* vol. 7, no. 1, p. 012006, 2016.

[14] C. Li, J. He, Y. Xiao, Y. Li, and J.-J. Delaunay, "Earth-abundant Cu-based metal oxide photocathodes for photoelectrochemical water splitting," *Energy & Environmental Science,* vol. 13, no. 10, pp. 3269-3306, 2020.

[15] M. Bonomo and D. Dini, "Nanostructured p-type semiconductor electrodes and photoelectrochemistry of their reduction processes," *Energies,* vol. 9, no. 5, p. 373, 2016.

[16] Z. Zhang and J. T. Yates Jr, "Band bending in semiconductors: chemical and physical consequences at surfaces and interfaces," *Chemical reviews,* vol. 112, no. 10, pp. 5520-5551, 2012.

[17] A. Heller, "Conversion of sunlight into electrical power and photoassisted electrolysis of water in photoelectrochemical cells," *Accounts of chemical research,* vol. 14, no. 5, pp. 154-162, 1981.

[18] S. G. Kumar and K. K. Rao, "Comparison of modification strategies towards enhanced charge carrier separation and photocatalytic degradation activity of metal oxide semiconductors (TiO2, WO3 and ZnO)," *Applied Surface Science,* vol. 391, pp. 124-148, 2017.

[19] S. Chen and L.-W. Wang, "Thermodynamic oxidation and reduction potentials of photocatalytic semiconductors in aqueous solution," *Chemistry of Materials,* vol. 24, no. 18, pp. 3659-3666, 2012.

[20] W. Leng, P. R. Barnes, M. Juozapavicius, B. C. O'Regan, and J. R. Durrant, "Electron diffusion length in mesoporous nanocrystalline TiO2 photoelectrodes during water oxidation," *The Journal of Physical Chemistry Letters,* vol. 1, no. 6, pp. 967-972, 2010.

[21] Y. S. Chaudhary, R. Shrivastav, V. R. Satsangi, and S. Dass, "Synthesis and characterization of nanostructured undoped/doped CuO films and their application in photoelectrochemical water splitting," *NSTI Nanotechnol,* vol. 2, pp. 601-603, 2005.

[22] K. W. Lim and J.-L. Lee, "Three-Dimensional CuO Branched Nanowires for Efficient Photoelectrochemical Water Splitting," in *ECS Meeting Abstracts,* 2016, no. 29: IOP Publishing, p. 1466.

[23] P. Sharma, J. W. Jang, and J. S. Lee, "Key strategies to advance the photoelectrochemical water splitting performance of α-Fe2O3 photoanode," *ChemCatChem,* vol. 11, no. 1, pp. 157-179, 2019.

[24] G. Wang, Y. Ling, H. Wang, L. Xihong, and Y. Li, "Chemically modified nanostructures for photoelectrochemical water splitting," *Journal of Photochemistry and Photobiology C: Photochemistry Reviews,* vol. 19, pp. 35-51, 2014.

[25] T. Bak, J. Nowotny, M. Rekas, and C. Sorrell, "Photo-electrochemical hydrogen generation from water using solar energy. Materials-related aspects," *International journal of hydrogen energy,* vol. 27, no. 10, pp. 991-1022, 2002.

[26] J. Tan *et al.*, "Fullerene as a photoelectron transfer promoter enabling stable TiO2-protected Sb2Se3 photocathodes for photo-electrochemical water splitting," *Advanced Energy Materials,* vol. 9, no. 16, p. 1900179, 2019.

[27] D. Bae, B. Seger, P. C. Vesborg, O. Hansen, and I. Chorkendorff, "Strategies for stable water splitting via protected photoelectrodes," *Chemical Society Reviews,* vol. 46, no. 7, pp. 1933-1954, 2017.

[28] C. Jiang, S. J. Moniz, A. Wang, T. Zhang, and J. Tang, "Photoelectrochemical devices for solar water splitting–materials and challenges," *Chemical Society Reviews,* vol. 46, no. 15, pp. 4645-4660, 2017.

[29] K. L. Hardee and A. J. Bard, "Semiconductor electrodes: V. The application of chemically vapor deposited iron oxide films to photosensitized electrolysis," *Journal of the Electrochemical Society,* vol. 123, no. 7, p. 1024, 1976.

[30] M. Kapilashrami, Y. Zhang, Y.-S. Liu, A. Hagfeldt, and J. Guo, "Probing the optical property and electronic structure of TiO2 nanomaterials for renewable energy applications," *Chemical reviews,* vol. 114, no. 19, pp. 9662-9707, 2014.

[31] J. Li *et al.*, "Copper oxide nanowires for efficient photoelectrochemical water splitting," *Applied Catalysis B: Environmental,* vol. 240, pp. 1-8, 2019.

[32] I. V. Bagal *et al.*, "Cu2O as an emerging photocathode for solar water splitting-a status review," *International Journal of Hydrogen Energy,* vol. 44, no. 39, pp. 21351-21378, 2019.

[33] X.-Q. Chen, C. L. Fu, C. Franchini, and R. Podloucky, "Hybrid density-functional calculation of the electronic and magnetic structures of tetragonal CuO," *Physical Review B,* vol. 80, no. 9, p. 094527, 2009.

[34] G. Shi, J. Liu, B. Chen, Y. Bao, and J. Xu, "Phase‐controlled growth of cubic phase CuO nanoparticles by chemical vapor deposition," *physica status solidi (a),* vol. 214, no. 10, p. 1700041, 2017.

[35] A. Moura *et al.*, "Structure and growth mechanism of CuO plates obtained by microwave-hydrothermal without surfactants," *Advanced Powder Technology,* vol. 21, no. 2, pp. 197-202, 2010.

[36] W. Yang *et al.*, "Time-resolved observations of photo-generated charge-carrier dynamics in Sb2Se3 photocathodes for photoelectrochemical water splitting," *ACS nano,* vol. 12, no. 11, pp. 11088-11097, 2018.

[37] H.-C. Fu *et al.*, "Improved performance and stability of photoelectrochemical water-splitting Si system using a bifacial design to decouple light harvesting and electrocatalysis," *Nano Energy,* vol. 70, p. 104478, 2020.

[38] K. Sekizawa, K. Oh-Ishi, and T. Morikawa, "Photoelectrochemical water-splitting over a surface modified p-type Cr 2 O 3 photocathode," *Dalton Transactions,* vol. 49, no. 3, pp. 659-666, 2020.

[39] B. Meyer *et al.*, "Binary copper oxide semiconductors: From materials towards devices," *physica status solidi (b),* vol. 249, no. 8, pp. 1487-1509, 2012.

[40] C.-Y. Chiang, K. Aroh, N. Franson, V. R. Satsangi, S. Dass, and S. Ehrman, "Copper oxide nanoparticle made by flame spray pyrolysis for photoelectrochemical water splitting–Part II. Photoelectrochemical study," *International journal of hydrogen energy,* vol. 36, no. 24, pp. 15519-15526, 2011.

[41] Y.-F. Lim, C. S. Chua, C. J. J. Lee, and D. Chi, "Sol–gel deposited Cu 2 O and CuO thin films for photocatalytic water splitting," *Physical Chemistry Chemical Physics,* vol. 16, no. 47, pp. 25928-25934, 2014.

[42] F. Koffyberg and F. Benko, "A photoelectrochemical determination of the position of the conduction and valence band edges of p‐type CuO," *Journal of Applied Physics,* vol. 53, no. 2, pp. 1173-1177, 1982.

[43] K. H. Yoon, W. J. Choi, and D. H. Kang, "Photoelectrochemical properties of copper oxide thin films coated on an n-Si substrate," *Thin solid films,* vol. 372, no. 1-2, pp. 250-256, 2000.

[44] H. Tang *et al.*, "Enhancing the stability of CuO thin-film photoelectrodes by Ti alloying," *Journal of electronic materials*, vol. 41, no. 11, pp. 3062-3067, 2012.

[45] Z. Wang *et al.*, "Identifying copper vacancies and their role in the CuO based photocathode for water splitting," *Angewandte Chemie,* vol. 131, no. 49, pp. 17768-17773, 2019.

[46] P. M. Grant, "Electronic properties of rocksalt copper monoxide: a proxy structure for high temperature superconductivity," in *Journal of Physics: Conference Series*, 2008, vol. 129, no. 1: IOP Publishing, p. 012042.

[47] W. Siemons, G. Koster, D. H. Blank, R. H. Hammond, T. H. Geballe, and M. R. Beasley, "Tetragonal CuO: End member of the 3 d transition metal monoxides," *Physical Review B,* vol. 79, no. 19, p. 195122, 2009.

[48] S. Moser *et al.*, "Magnons in tetragonal CuO," *Physical Review B,* vol. 92, no. 14, p. 140404, 2015.

[49] I. J. Hamad, L. O. Manuel, and A. Aligia, "Generalized one-band model based on Zhang-Rice singlets for Tetragonal CuO," *Physical review letters,* vol. 120, no. 17, p. 177001, 2018.

[50] K. Rabinovich, L. Samoilenko, A. Zhuravleva, and A. Shneider, "Magnetic properties of high-symmetry CuO," *Applied Physics Letters,* vol. 104, no. 18, p. 182406, 2014.

[51] C. Franchini, X.-Q. Chen, and R. Podloucky, "Thickness dependent structural and electronic properties of CuO grown on SrTiO3 (100): a hybrid density functional theory study," *Journal of Physics: Condensed Matter,* vol. 23, no. 4, p. 045004, 2010.

[52] M. Heinemann, B. Eifert, and C. Heiliger, "Band structure and phase stability of the copper oxides Cu 2 O, CuO, and Cu 4 O 3," *Physical Review B,* vol. 87, no. 11, p. 115111, 2013.

[53] S. Hibble, C. Malitesta, and P. G. Dickens, "The chemical and electrochemical lithiation of CuO: an analytical, electron microscopy investigation," *Solid state ionics,* vol. 39, no. 3-4, pp. 289-295, 1990.

[54] B. Himmetoglu, R. M. Wentzcovitch, and M. Cococcioni, "First-principles study of electronic and structural properties of CuO," *Physical Review B,* vol. 84, no. 11, p. 115108, 2011.

[55] B. Yao, X. Zhou, M. Liu, J. Yu, J. Cao, and L. Wang, "First-principles calculations on phase transformation and elastic properties of CuO under pressure," *Journal of Computational Electronics,* vol. 17, no. 4, pp. 1450-1456, 2018.

[56] B. Yang, T. Thurston, J. Tranquada, and G. Shirane, "Magnetic neutron scattering study of single-crystal cupric oxide," *Physical Review B,* vol. 39, no. 7, p. 4343, 1989.

[57] S. Åsbrink and L.-J. Norrby, "A refinement of the crystal structure of copper (II) oxide with a discussion of some exceptional esd's," *Acta Crystallographica Section B: Structural Crystallography and Crystal Chemistry,* vol. 26, no. 1, pp. 8-15, 1970.

[58] H.-J. Koo and M.-H. Whangbo, "Magnetic superstructures of cupric oxide CuO as ordered arrangements of one-dimensional antiferromagnetic chains," *Inorganic chemistry,* vol. 42, no. 4, pp. 1187-1192, 2003.

[59] H. Ohno, H. Munekata, y. T. Penney, S. Von Molnar, and L. Chang, "Magnetotransport properties of p-type (In, Mn) As diluted magnetic III-V semiconductors," *Physical Review Letters,* vol. 68, no. 17, p. 2664, 1992.

[60] T. Story, R. Gałazka, R. B. Frankel, and P. Wolff, "Carrier-concentration–induced ferromagnetism in PbSnMnTe," *Physical review letters,* vol. 56, no. 7, p. 777, 1986.

[61] A. Filippetti and V. Fiorentini, "Magnetic ordering in CuO from first principles: a cuprate antiferromagnet with fully three-dimensional exchange interactions," *Physical review letters,* vol. 95, no. 8, p. 086405, 2005.

[62] M. He, M. Luo, and P. Fang, "Characterization of CuO species and thermal solid-solid interaction in CuO/CeO2-Al2O3 catalyst by in-situ XRD, Raman spectroscopy and TPR," *Journal of Rare Earths,* vol. 24, no. 2, pp. 188-192, 2006.

[63] P. Samarasekara, N. Kumara, and N. Yapa, "Sputtered copper oxide (CuO) thin films for gas sensor devices," *Journal of Physics: Condensed Matter,* vol. 18, no. 8, p. 2417, 2006.

[64] S. Shinde *et al.*, "Using chemical bath deposition to create nanosheet-like CuO electrodes for supercapacitor applications," *Colloids and Surfaces B: Biointerfaces,* vol. 181, pp. 1004-1011, 2019.

[65] S. Yip and J. Sauls, "Nonlinear Meissner effect in CuO superconductors," *Physical review letters,* vol. 69, no. 15, p. 2264, 1992.

[66] D. Shang *et al.*, "Magnetic and field emission properties of straw-like CuO nanostructures," *Applied Surface Science,* vol. 255, no. 7, pp. 4093-4096, 2009.

[67] J. Toupin, H. Strubb, S. Kressman, V. Artero, N. Krins, and C. Laberty-Robert, "CuO photoelectrodes synthesized by the sol–gel method for water splitting," *Journal of Sol-Gel Science and Technology,* vol. 89, no. 1, pp. 255-263, 2019.

[68] K. T. Chaudhary, "Thin Film Deposition: Solution Based Approach," in *Thin Films*: IntechOpen, 2021.

[69] C. Brinker, G. Frye, A. Hurd, and C. Ashley, "Fundamentals of sol-gel dip coating," *Thin solid films,* vol. 201, no. 1, pp. 97-108, 1991.

[70] C. Brinker, A. Hurd, P. Schunk, G. Frye, and C. Ashley, "Review of sol-gel thin film formation," *Journal of Non-Crystalline Solids,* vol. 147, pp. 424-436, 1992.

[71] M. Tyona, "A theoritical study on spin coating technique," *Advances in materials Research,* vol. 2, no. 4, p. 195, 2013.

[72] D. Perednis and L. J. Gauckler, "Thin film deposition using spray pyrolysis," *Journal of electroceramics,* vol. 14, no. 2, pp. 103-111, 2005.

[73] R. Chamberlin and J. Skarman, "Chemical spray deposition process for inorganic films," *Journal of the Electrochemical Society,* vol. 113, no. 1, p. 86, 1966.

[74] P. S. Patil, "Versatility of chemical spray pyrolysis technique," *Materials Chemistry and physics,* vol. 59, no. 3, pp. 185-198, 1999.

[75] M. Patel, R. Pati, P. Marathey, J. Kim, I. Mukhopadhyay, and A. Ray, "Highly photoactive and photo-stable spray pyrolyzed tenorite CuO thin films for photoelectrochemical energy conversion," *Journal of The Electrochemical Society,* vol. 163, no. 14, p. H1195, 2016.

[76] D. P. Dubal and R. Holze, "A successive ionic layer adsorption and reaction (SILAR) method to induce Mn 3 O 4 nanospots on CNTs for supercapacitors," *New Journal of Chemistry,* vol. 37, no. 2, pp. 403-408, 2013.

[77] Y. Nicolau, "Solution deposition of thin solid compound films by a successive ionic-layer adsorption and reaction process," *Applications of Surface Science,* vol. 22, pp. 1061-1074, 1985.

[78] H. Pathan and C. Lokhande, "Deposition of metal chalcogenide thin films by successive ionic layer adsorption and reaction (SILAR) method," *Bulletin of Materials Science,* vol. 27, no. 2, pp. 85-111, 2004.

[79] S. Swann, "Magnetron sputtering," *Physics in technology,* vol. 19, no. 2, p. 67, 1988.

[80] B. E. Aufderheide, "30.2 General Principles of Sputtering," *Coatings Technology Handbook,* 2006.

[81] M. J. Jung, K. H. Nam, L. R. Shaginyan, and J. G. Han, "Deposition of Ti thin film using the magnetron sputtering method," *Thin Solid Films,* vol. 435, no. 1-2, pp. 145-149, 2003.

[82] K. Tschulik, C. Batchelor-McAuley, H.-S. Toh, E. J. Stuart, and R. G. Compton, "Electrochemical studies of silver nanoparticles: a guide for experimentalists and a perspective," *Physical Chemistry Chemical Physics,* vol. 16, no. 2, pp. 616-623, 2014.

[83] M. Eslamian and F. Soltani-Kordshuli, "Development of multiple-droplet drop-casting method for the fabrication of coatings and thin solid films," *Journal of Coatings Technology and Research,* vol. 15, no. 2, pp. 271-280, 2018.

[84] A. L. Yarin, "Drop impact dynamics: splashing, spreading, receding, bouncing…," *Annu. Rev. Fluid Mech.,* vol. 38, pp. 159-192, 2006.

[85] H. S. Park, C.-Y. Lee, and E. Reisner, "Photoelectrochemical reduction of aqueous protons with a CuO| CuBi 2 O 4 heterojunction under visible light irradiation," *Physical Chemistry Chemical Physics,* vol. 16, no. 41, pp. 22462-22465, 2014.

[86] S. Aydemir, "Effects of withdrawal speed on the microstructural and optical properties of sol–gel grown ZnO: Al thin films," *Vacuum,* vol. 120, pp. 51-58, 2015.

[87] L. Landau and B. Levich, "Dragging of a liquid by a moving plate," in *Dynamics of curved fronts*: Elsevier, 1988, pp. 141-153.

[88] Z. N. Kayani, A. Aslam, R. Ishaque, S. N. Zahra, H. Hanif, and H. Khan, "The effect of the withdrawal speed on properties of nickel oxide thin films," *Zeitschrift für Kristallographie-Crystalline Materials,* vol. 234, no. 10, pp. 647-655, 2019.

[89] S. Mei, J. Yang, S. Christian, S. Yuan, and J. M. F. Ferreira, "Fabrication and characterisation of titania nanoporous thin film for photoelectrochemical (PEC) conversion of water," *Energy Procedia,* vol. 75, pp. 2187-2192, 2015.

[90] Y. Akaltun, "Effect of thickness on the structural and optical properties of CuO thin films grown by successive ionic layer adsorption and reaction," *Thin Solid Films,* vol. 594, pp. 30-34, 2015.

[91] H. B. Saâd, M. Ajili, S. Dabbabi, and N. T. Kamoun, "Investigation on thickness and annealing effects on physical properties and electrical circuit model of CuO sprayed thin films," *Superlattices and Microstructures,* vol. 142, p. 106508, 2020.

[92] S. Shariffudin, S. Khalid, N. Sahat, M. Sarah, and H. Hashim, "Preparation and characterization of nanostructured CuO thin films using sol-gel dip coating," in *IOP Conference Series: Materials Science and Engineering*, 2015, vol. 99, no. 1: IOP Publishing, p. 012007.

[93] M. R. Johan, M. S. M. Suan, N. L. Hawari, and H. A. Ching, "Annealing effects on the properties of copper oxide thin films prepared by chemical deposition," *Int. J. Electrochem. Sci,* vol. 6, no. 12, pp. 6094-6104, 2011.

[94] F. A. Akgul, G. Akgul, N. Yildirim, H. E. Unalan, and R. Turan, "Influence of thermal annealing on microstructural, morphological, optical properties and surface electronic structure of copper oxide thin films," *Materials Chemistry and Physics,* vol. 147, no. 3, pp. 987-995, 2014.

[95] C. Abinaya *et al.*, "The effect of post-deposition annealing conditions on structural and thermoelectric properties of sputtered copper oxide films," *RSC Advances,* vol. 10, no. 49, pp. 29394-29401, 2020.

[96] J. G. Lee *et al.*, "Scalable binder-free supersonic cold spraying of nanotextured cupric oxide (CuO) films as efficient photocathodes," *ACS applied materials & interfaces,* vol. 8, no. 24, pp. 15406-15414, 2016.

[97] S.-C. Jung, S.-J. Kim, N. Imaishi, and Y.-I. Cho, "Effect of TiO2 thin film thickness and specific surface area by low-pressure metal–organic chemical vapor deposition on photocatalytic activities," *Applied Catalysis B: Environmental,* vol. 55, no. 4, pp. 253-257, 2005.

[98] K. Anuar, W. Tan, M. Jelas, S. Ho, S. Gwee, and N. Saravanan, "Effects of deposition period on the properties of FeS2 thin films by chemical bath deposition method," *Science & Technology Asia,* pp. 62-69, 2010.

[99] V. Shinde, T. Gujar, and C. Lokhande, "Studies on growth of ZnO thin films by a novel chemical method," *Solar energy materials and solar cells,* vol. 91, no. 12, pp. 1055-1061, 2007.

[100] C. S. Yaw, A. K. Soh, and M. N. Chong, "Effect of deposition time on the photoelectrochemical properties of cupric oxide thin films synthesized via electrodeposition method," in *MATEC Web of Conferences*, 2016, vol. 60: EDP Sciences, p. 01001.

[101] B. Reguig, M. Regragui, M. Morsli, A. Khelil, M. Addou, and J. Bernede, "Effect of the precursor solution concentration on the NiO thin film properties deposited by spray pyrolysis," *Solar Energy Materials and Solar Cells,* vol. 90, no. 10, pp. 1381-1392, 2006.

[102] S. Golshahi, S. Rozati, R. Martins, and E. Fortunato, "P-type ZnO thin film deposited by spray pyrolysis technique: The effect of solution concentration," *Thin solid films,* vol. 518, no. 4, pp. 1149-1152, 2009.

[103] A. Kushwaha, R. S. Moakhar, G. K. Goh, and G. K. Dalapati, "Morphologically tailored CuO photocathode using aqueous solution technique for enhanced visible light driven water splitting," *Journal of Photochemistry and Photobiology A: Chemistry,* vol. 337, pp. 54-61, 2017.

[104] A. Abdelkrim, S. Rahmane, O. Abdelouahab, N. Abdelmalek, and G. Brahim, "Effect of solution concentration on the structural, optical and electrical properties of SnO2 thin films prepared by spray pyrolysis," *Optik,* vol. 127, no. 5, pp. 2653-2658, 2016.

[105] A. Cots, P. Bonete, and R. Gómez, "Improving the stability and efficiency of CuO photocathodes for solar hydrogen production through modification with iron," *ACS applied materials & interfaces,* vol. 10, no. 31, pp. 26348-26356, 2018.

[106] H. Xing, E. Lei, Z. Guo, D. Zhao, X. Li, and Z. Liu, "Exposing the photocorrosion mechanism and control strategies of a CuO photocathode," *Inorganic Chemistry Frontiers,* vol. 6, no. 9, pp. 2488-2499, 2019.

[107] A. M. Ahmed, E. M. Abdalla, and M. Shaban, "Simple and low-cost synthesis of Ba-doped CuO thin films for highly efficient solar generation of hydrogen," *The Journal of Physical Chemistry C,* vol. 124, no. 41, pp. 22347-22356, 2020.

[108] R. Liu, Z. Zheng, J. Spurgeon, and X. Yang, "Enhanced photoelectrochemical water-splitting performance of semiconductors by surface passivation layers," *Energy & Environmental Science,* vol. 7, no. 8, pp. 2504-2517, 2014.

[109] Z. Guo and Z. Liu, "Synthesis and control strategies of nanomaterials for photoelectrochemical water splitting," *Dalton Transactions,* 2021.

[110] E. L. Tsege, S. K. Cho, L. T. Tufa, J. Lee, H.-K. Kim, and Y.-H. Hwang, "Scalable and inexpensive strategy to fabricate CuO/ZnO nanowire heterojunction for efficient photoinduced water splitting," *Journal of Materials Science,* vol. 53, no. 4, pp. 2725-2734, 2018.

[111] B. Klahr, S. Gimenez, F. Fabregat-Santiago, J. Bisquert, and T. W. Hamann, "Photoelectrochemical and impedance spectroscopic investigation of water oxidation with “Co–Pi”-coated hematite electrodes," *Journal of the American Chemical Society,* vol. 134, no. 40, pp. 16693-16700, 2012.

[112] K. Sivula, "Metal oxide photoelectrodes for solar fuel production, surface traps, and catalysis," *The Journal of Physical Chemistry Letters,* vol. 4, no. 10, pp. 1624-1633, 2013.

[113] T. P. Brennan *et al.*, "TiO2 conduction band modulation with In2O3 recombination barrier layers in solid-state dye-sensitized solar cells," *The Journal of Physical Chemistry C,* vol. 117, no. 46, pp. 24138-24149, 2013.

[114] H. Xing, E. Lei, D. Zhao, X. Li, M. Ruan, and Z. Liu, "A high-efficiency and stable cupric oxide photocathode coupled with Al surface plasmon resonance and Al 2 O 3 self-passivation," *Chemical Communications,* vol. 55, no. 100, pp. 15093-15096, 2019.

[115] P. P. Kunturu and J. Huskens, "Efficient solar water splitting photocathodes comprising a copper oxide heterostructure protected by a thin carbon layer," *ACS Applied Energy Materials,* vol. 2, no. 11, pp. 7850-7860, 2019.

[116] D. S. Eissa, S. S. El-Hagar, E. A. Ashour, and N. K. Allam, "Electrochemical nano-patterning of brass for stable and visible light-induced photoelectrochemical water splitting," *International Journal of Hydrogen Energy,* vol. 44, no. 29, pp. 14588-14595, 2019.

[117] J. Lin, W. Wang, and G. Li, "Modulating Surface/Interface Structure of Emerging InGaN Nanowires for Efficient Photoelectrochemical Water Splitting," *Advanced Functional Materials,* vol. 30, no. 52, p. 2005677, 2020.

[118] O. Zandi and T. W. Hamann, "The potential versus current state of water splitting with hematite," *Physical Chemistry Chemical Physics,* vol. 17, no. 35, pp. 22485-22503, 2015.

[119] A. Amin and A. El-dissouky, "One-step synthesis of novel Cu2ZnNiO3 complex oxide nanowires with tuned band gap for photoelectrochemical water splitting," *Journal of Applied Crystallography,* vol. 53, no. 6, 2020.

[120] Y. Xia *et al.*, "One‐dimensional nanostructures: synthesis, characterization, and applications," *Advanced materials,* vol. 15, no. 5, pp. 353-389, 2003.

[121] L. A. Cipriano, G. Di Liberto, S. Tosoni, and G. Pacchioni, "Quantum confinement in group III–V semiconductor 2D nanostructures," *Nanoscale,* vol. 12, no. 33, pp. 17494-17501, 2020.

[122] O. Crespo-Biel, B. J. Ravoo, D. N. Reinhoudt, and J. Huskens, "Noncovalent nanoarchitectures on surfaces: from 2D to 3D nanostructures," *Journal of materials chemistry,* vol. 16, no. 41, pp. 3997-4021, 2006.

[123] X. Zhao, P. Wang, Z. Yan, and N. Ren, "Ag nanoparticles decorated CuO nanowire arrays for efficient plasmon enhanced photoelectrochemical water splitting," *Chemical Physics Letters*, vol. 609, pp. 59-64, 2014.

[124] L. Jin, H. Zhao, Z. M. Wang, and F. Rosei, "Quantum Dots‐Based Photoelectrochemical Hydrogen Evolution from Water Splitting," *Advanced Energy Materials,* vol. 11, no. 12, p. 2003233, 2021.

[125] S. Masudy-Panah, R. Siavash Moakhar, C. S. Chua, A. Kushwaha, and G. K. Dalapati, "Stable and efficient CuO based photocathode through oxygen-rich composition and Au–Pd nanostructure incorporation for solar-hydrogen production," *ACS applied materials & interfaces,* vol. 9, no. 33, pp. 27596-27606, 2017.

Chapter 3

3.0 Experimental

3.1 Introduction

In this chapter, the fabrication of Copper Oxide (CuO) thin films prepared via the sol-gel dip-coating method at different withdrawal rates, film thicknesses and annealing temperatures are discussed. Furthermore, the deposition of protective layers of CuO films with Activated Charcoal (AC) by spray pyrolysis and Silver (Ag) and Gold (Au) nanoparticles (NPs) by drop casting method to improve the photo-stability of the films in electrolyte are presented. The results of studying the pristine and modified CuO films using X-ray diffraction (XRD), field emission scanning electron microscopy (FE-SEM), energy dispersive X-ray spectroscopy (EDS), ultraviolet-visible (UV-Vis) spectroscopy and Raman spectroscopy are explained in detail. Furthermore, an expansive discussion of the results obtained from the photoelectrochemical (PEC) studies of all pristine and modified CuO photocathodes using linear sweep voltammetry (LSV), electrochemical impedance spectroscopy (EIS), Mott-Schottky (MS) analysis, and chronoamperometry techniques are given.

3.2 Preparation of CuO thin films

3.2.1 Substrate cleaning

Fluorine-doped Tin Oxide (FTO) substrates of dimensions 1.1 x 3 cm were sequentially cleaned in an ultrasonic bath with detergent, deionised (DI) water, ethanol, and isopropanol for 15 min each. The substrates were further dried with nitrogen gas to remove the excess isopropanol. The FTO substrates were purchased from Sigma Aldrich and has a sheet resistance of 7 Ω/sq.

3.2.2 Synthesis of CuO thin films

The precursor solution used for the deposition of CuO films was prepared by dissolving 0.25 M copper acetate in 90% propan-2-ol, 5% diethanolamine and 5% polyethylene glycol-400 at room temperature. All the chemicals used were purchased from Sigma Aldrich and were of analytical grade. In detail, 0.25 M copper acetate was dissolved in 27 ml propan-2-ol, the solution was vigorously stirred for 1 hr. Afterwards, 1.5 ml diethanolamine was added and continuously stirred for another 1 hr. Finally, 1.5 ml polyethylene glycol-400 was added to the solution and further stirred for 2 hrs. For the optimization of withdrawal speed, the substrates were dipped into the precursor solution for 1 min and withdrawn at different rates of 50, 100, 150 and 200 mm/min respectively. The films were then dried at 120 °C for 12 min, and further treated at 300 °C for 5 min. The process was repeated five times to obtain 5 layers of the films prepared at different withdrawal rates. The films were all annealed for 1 hr at 600 °C for further crystallization. For the optimization of the film thickness, additional samples were prepared at a constant withdrawal speed of 150 mm/min to consist of 7 and 10 layers of the CuO films under the same drying and annealing conditions. Lastly, more CuO films were prepared at withdrawal speed of 150 mm/min, consisting of 7 layers, and subjected to the same drying and heat treatment conditions as previous samples except that the films were annealed at 400°C, 500°C and 650°C to also study the influence of annealing temperature on the photocatalytic properties of the films. An illustration of this experimental procedure is given in Figure **3.2.*1***

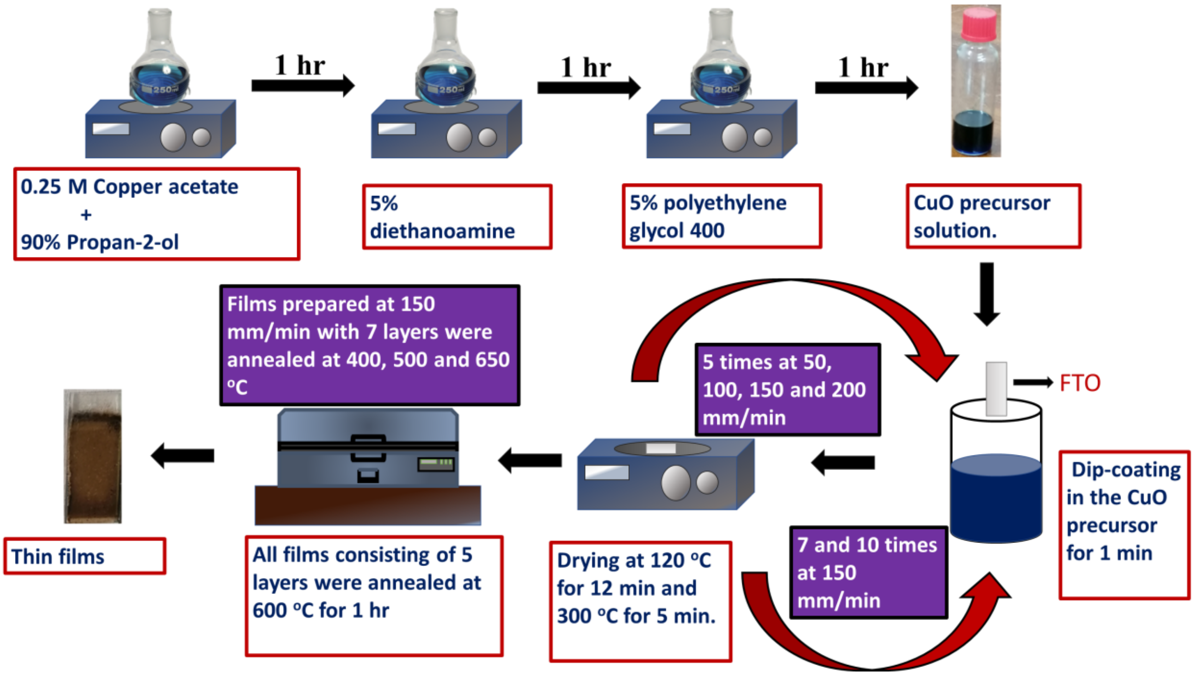

Figure 3.2.1 Schematic illustration of the experimental procedure for the preparation of the CuO precursor and CuO thin film preparation using the three-step heat treatment approach.

3.2.3 Synthesis of CuO films modified with activated charcoal (AC)

Pristine CuO films were first prepared as described in section 3.2.2 at a withdrawal rate of 150 mm/min, consisting of 7 layers and annealed at 600 °C. The pristine CuO films were modified with different number of layers of AC via spray pyrolysis. A 0.5 M of AC solution was prepared by dissolving 2.40 g of AC in 400 ml of ethanol under vigorous stirring for 30 minutes. One layer of AC was deposited on the pristine CuO films using a 0.5 mm nozzle and spray solution of AC at a nozzle-substrate distance of 30 cm, substrate temperature of 300°C, and spray-time of 30 s. The sample was further treated at 350 °C to obtain 1 layer of AC on CuO films. Following the same procedure, two more samples were prepared consisting of 3 and 5 layers of AC on pristine CuO films. CuO/AC-1L, CuO/AC-3L and CuO-AC-5L were used to denote the pristine CuO samples modified with 1, 3, and 5 layers of AC respectively. Figure 3.2.2 presents a simple illustration of the process of AC deposition on pristine CuO.

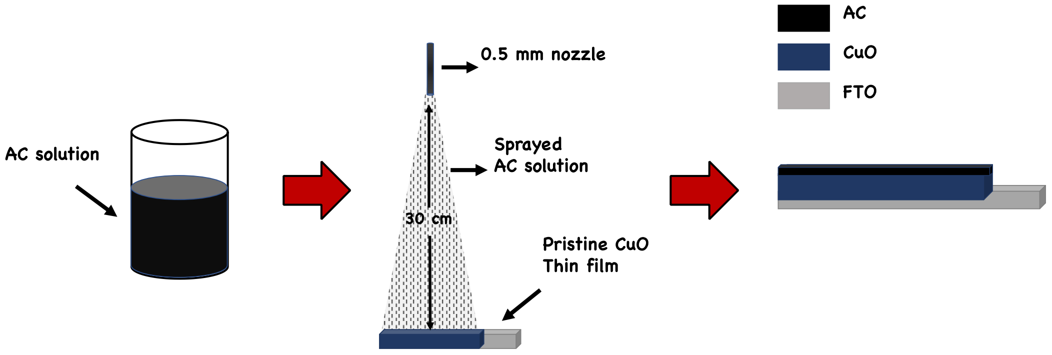

Figure 3.2.2 Schematic representation of the synthesis of CuO/AC thin films.

3.2.4 Synthesis of CuO/Ag thin films

Pristine CuO films prepared as described in section 3.2.2 at a withdrawal rate of 150 mm/min, consisting of 7 layers and annealed at 600 °C were modified with Ag nanoparticles using a simple solution-based drop casting technique. To prepare the Ag NPs used for the modification the CuO films, 1 mM Silver Nitrate ($AgNO_3$) was dissolved in 50 ml di-ionized (DI) water under vigorous stirring, at room temperature. 1 mM trisodium citrate ($Na_3C_6H_50_7$) was then slowly added to the solution while stirring. Lastly, 1.5 L aqueous solution of 40 mM Sodium Borohydride ($NaBH_4$) was added into the solution, which immediately turned yellow. The solution was heated at 100°C for 30 min to obtain a solution of Ag nanoparticles [1, 2]. 150 µL of the Ag NPs solution was deposited dropwise on FTO/CuO films via drop casting and allowed to dry at 100°C for 15 min to form one (1) layer of Ag nanoparticles on the pristine CuO films (Figure 3.2.3). Following the same drop casting procedure, additional samples were prepared to consist of 3 and 5 layers of deposited Ag nanoparticles on the pristine CuO films. The pristine CuO films modified with 1, 3, and 5 layers of Ag were labeled CuO/Ag-1L, CuO/Ag-3L, and CuO/Ag-5L respectively.

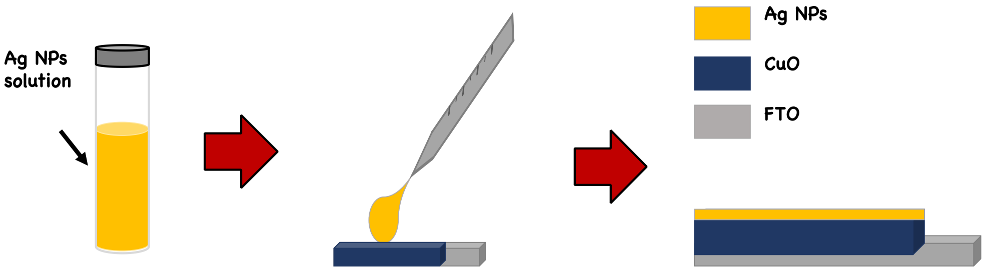

Figure 3.2.3 Schematic illustration of the surface modification of CuO films with Ag NPs

3.2.5 Synthesis of CuO/Au thin films

CuO films prepared as described in section 3.2.2 at a withdrawal rate of 150 mm/min, consisting of 7 layers and annealed at 600 °C were also modified with Au nanoparticles using a simple solution-based drop casting technique. A solution of Au NPs was prepared by adding 40 mM $NaBH_4$ into a stirring solution containing 1 mM of Chloroauric acid ($HAuCl_4$) and 1 mM of $Na_3C_6H_50_7$ in DI water, the mixture immediately turned into a light shade of pink colour. The solution further turned into a dark shade of purple after a few minutes and to ruby-red following 20 minutes of heating while stirring at 100 °C, indicating the formation of Au nanoparticles. The ruby-red solution was heated for an additional 10 mins at the same temperature to obtain a solution of Au NPs. 150 µL of the prepared Au NPs solution was added dropwise onto the pristine CuO films via the drop casting technique illustrated in Figure 3.2.4. The films were allowed to dry on a hot plate at 100 °C for 15 min to obtain 1 layer of Au NPs on CuO films. Following the same drop casting procedure, additional samples were prepared to consist of 3 and 5 layers of deposited Au nanoparticles on the pristine CuO films. The pristine CuO films modified with 1, 3, and 5 layers of Ag were labeled CuO/Au-1L, CuO/Au-3L, and CuO/Au-5L respectively.

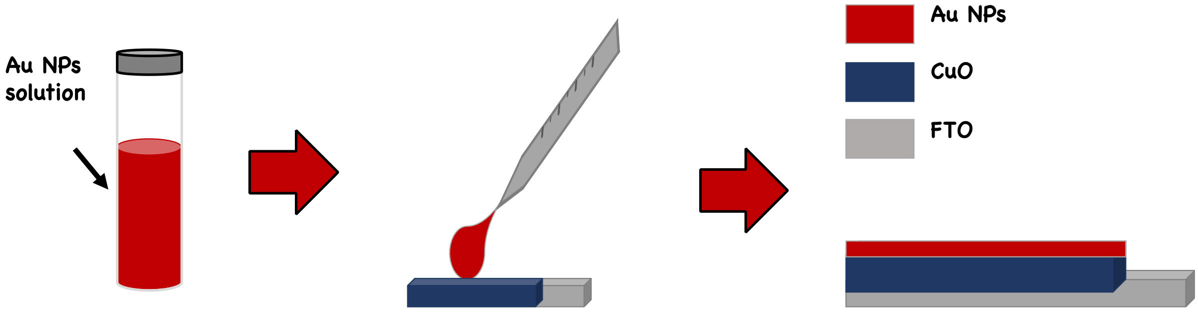

Figure 3.2.4 Schematic representation of the synthesis of CuO/Ag thin films.

3.3 Characterization

The structural properties of the prepared CuO, CuO/AC, CuO/Ag, CuO/Au thin films were investigated using XRD measurements with a D2 PHASER-e diffractometer which utilizes Cu-Kα radiation at a wavelength of 0.15418 nm. The Raman spectra of the films were analysed using WiTec alpha 300 RAS+ Confocal Raman instrument with an excitation laser of 532 nm at 5 mW. The Field emission scanning electron microscopy (FE-SEM) was used to study the surface morphology and cross-sectional views of the prepared films were studied using Zeiss Ultrafast 540 instrument. An energy dispersive X-ray spectroscopy (EDS) system which was coupled to the Zeiss Ultrafast 540 was used to analyse the elemental composition of the thin films. An Agilent Cary 60 UV-Vis spectrometer was used to study the optical properties of the films.

3.4 PEC measurements

PEC properties of CuO, CuO/AC, CuO/Ag, CuO/Au thin films were investigated. The films were used as photocathodes in a three-electrode electrochemical system [3]. The PEC cell used to perform the PEC measurements consist of a transparent window made of fused silica (amorphous SiO_2) for the transmission of light in the range of ultraviolet to near-infrared region of the electromagnetic spectrum [4]. 1 M NaOH (pH = 13.6) bubbled with N_2 gas for 30 mins was used as the electrolyte for the electrochemical measurements. The CuO photocathodes, 2 × 2 cm platinum mesh, and Ag/AgCl in 3M KCl were used as working, counter, and reference electrodes respectively. The PEC cell was coupled to a VersaSTAT 3F potentiostat from Princeton Applied Research which was used to carry out all the PEC measurements. The photo-current responses of the films were obtained using Linear Scan Voltammetry (LSV) measurements which were performed on the films under dark and illuminate conditions, in the potential range of 0 to -0.65 V vs Ag/AgCl, and at the scan rate of 0.04 V/s. The Newport *Oriel® LCS* −100 TM solar simulator was used as a light source and was calibrated using a Newport 91150V reference cell to 1 sun. Electrochemical impedance spectroscopy (EIS) measurements were performed to study the charge transport processes occurring at the surface of the photocathodes. These were carried out at -0.5 V vs. Ag/AgCl, at an excitation amplitude of 10 mV, and a frequency range of 10 000 – 0.1 Hz. The measurements were done in dark conditions for the pristine CuO samples and under illumination for the AC, Ag, and Au modified CuO films. EIS measurement was also performed on pristine CuO consisting of 7 layers under illumination for comparative purposes with the modified samples. The surface area of the photocathodes exposed to the illumination of light was 0.49 cm^2. The obtained EIS experimental data were fitted to an equivalent circuit model using the ZView software from Scribner Associates. Chronoamperometry measurements were also performed under dark and illumination conditions to study the stability of the thin films. This was done at -0.4 V vs Ag/AgCl for CuO and CuO/AC samples, and at -0.5 V vs Ag/AgCl for CuO/Ag and CuO/Au photocathodes. Also, the time scan was 0-500 s for the chronoamperometry measurements performed on the pristine photocathodes and 0-1200 s for all the other films. All the potentials measured against Ag/AgCl were converted to the RHE scale using Eq. 3.1:

$$\Phi_{RHE} = \Phi_{Ag/AgCl} + (0.059 \times pH) + \Phi°_{Ag/AgCl} \qquad \text{Eq. 3.1}$$

Φ_{RHE} represents the potential in RHE scale, whereas $\Phi_{Ag/AgCl}$ is the potential against the Ag/AgCl reference electrode and $\Phi°_{Ag/AgCl}$ is the potential of the reference electrode against Ag/AgCl used in the experiment. The value of $\Phi°_{Ag/AgCl}$ is 0.198 V at 25 ℃ [4, 5].

3.5. Techniques for film characterization

3.5.1. X-ray diffraction (XRD)

XRD has been a standard technique typically used to study the crystal structure, phase and orientation of materials. The XRD pattern of a material is used to determine the crystallinity, crystal size, lattice parameters, strain, and defects within its crystal structure [6]. The mechanism of XRD involves the generation of X-rays within a cathode ray tube of a diffractometer which are then shifted and bombarded onto the sample. The interaction of the X-rays with the sample triggers some rays to diffract in different directions. Lastly, the detector scans sample in a range of 2θ angles, processes the signals, and records the pattern of the diffracted X-rays on a monitor (Figure **3.5.*1***) [6, 7].

Diffraction occurs if the conditions of Bragg's law given in Eq. 3.2 are satisfied when the interaction between the incident X-rays and the sample produce constructive interference after the diffraction of the rays.

$$n\lambda = 2d \sin\theta \qquad \text{Eq. 3.2}$$

where λ represents the wavelength of the X-rays, n is an integer, d is the interplanar spacing between diffraction planes, and θ is the angle of diffraction [6, 8].

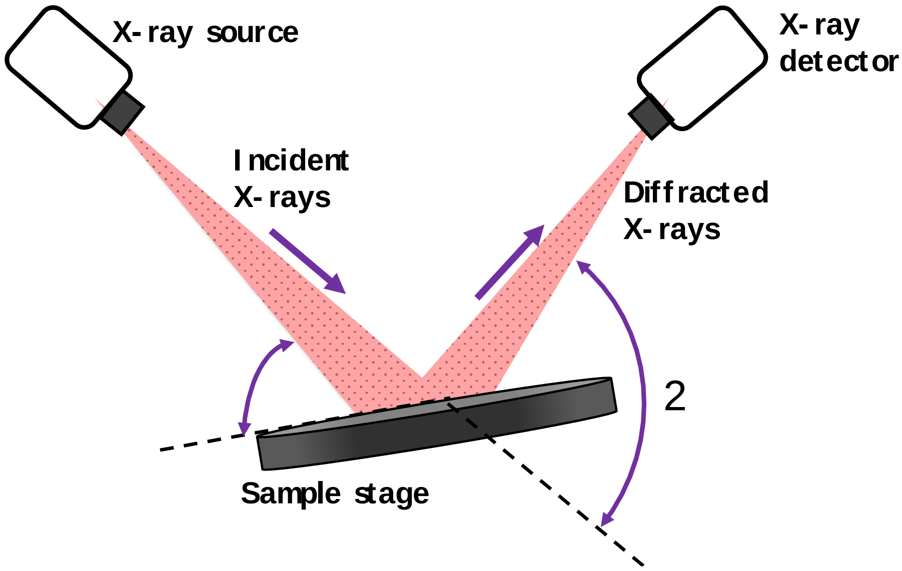

Figure 3.5.1 Schematic diagram of XRD.

3.5.2. Raman Spectroscopy

Raman spectroscopy is a non-destructive, analytical technique which has been used to determine the chemical composition, crystallinity, and molecular interaction of materials through the inelastic scattering of light [9, 10]. It involves the irradiation of a laser beam on a sample and sequentially, the beam of light is split into different wavelengths by an edge filter before being absorbed by a detector (Figure **3.5.2**). The spectrum of the measurement is recorded and displayed on a computer monitor as a plot of intensity against the Raman shift [9, 11].

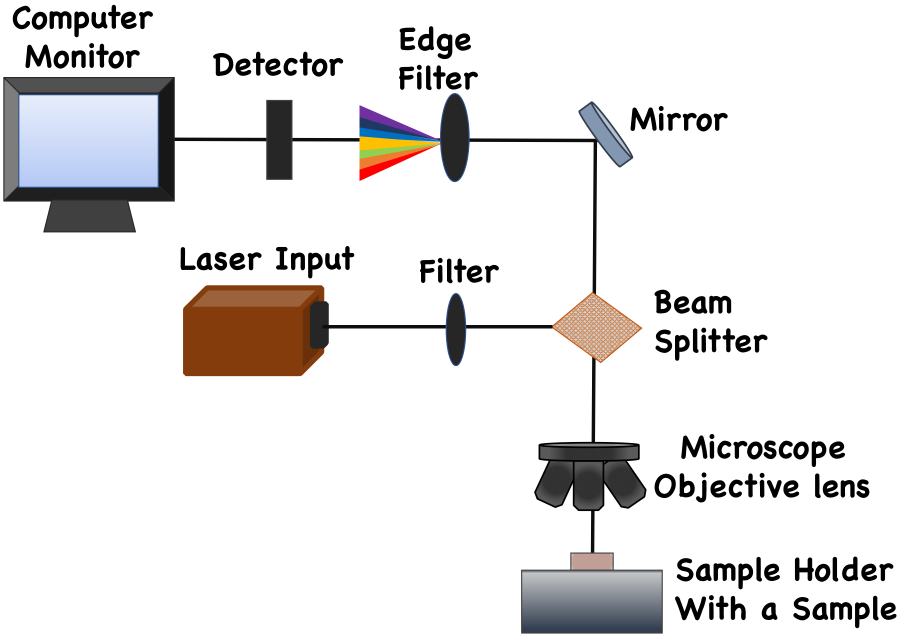

Figure 3.5.2 Schematic representation of Raman spectroscopy.

3.5.3. Scanning electron microscopy (SEM)

SEM is a non-destructive technique commonly used to study the surface morphology, chemical composition and crystalline structures of materials through the scanning of high-energy electron beams across the sample under vacuum [12]. SEM can operate at high magnifications of up to 1,000,000 times and has a large depth of field which enables focusing on a large portion of the sample surface. Therefore, it does not depend on the smoothness of the sample to function [12, 13].

The operation of SEM includes the thermal emission of high-energy electrons (~ 2 – 40 KeV) from the tip of an electron gun such as lanthanum hexaboride (LaB_6), field emission gun, and tungsten hairpin filament. The magnitude of the electron beam is then reduced into a fine probe by electromagnetic condenser lenses, and through some scan coils, the selected area of the surface of the sample is scanned in a raster which is synchronised with the electron beam

(Figure 3.5.3) [13, 14]. The interaction of the beam with the sample produces secondary and backscattered electrons. The signal from secondary electrons yields an image with a high depth of field, whereas the signal from the backscattered electrons yields an image that show the sample's composition. The signals are collected by detectors and recorded on a monitor [12, 13].

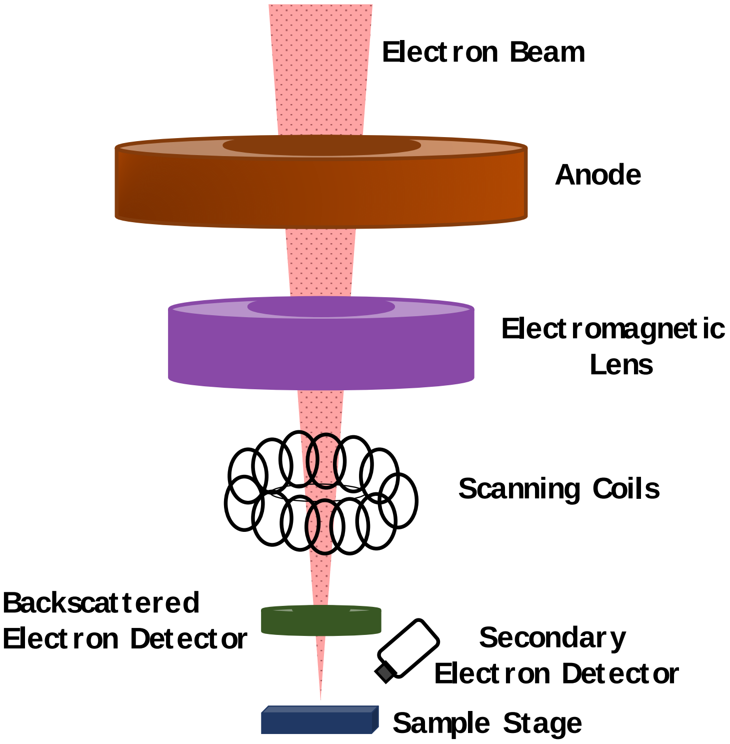

Figure 3.5.3 Schematic diagram of SEM.

3.5.4. Energy dispersive X-Ray Spectroscopy (EDS)

EDS is a microanalysis technique used to identify major elements mostly greater than 10 % by weight which are present at the point where the electron beam interacts with the sample [12]. Typically, it is coupled with SEM, hence it uses the electron beam of the microscope for the generation of characteristic X-rays of the main elements of a sample [15]. The emitted X-rays are then absorbed and separated by the detector on the basis of Bragg diffraction, leading to the identification of primary elements belonging to the material. The spectrum of the elements in a scanned area of a sample are recorded and shown on a monitor. Furthermore, EDS can map the elemental composition using the point analyser at a certain point of the sample [16, 17].

3.5.5. Ultraviolet and visible spectroscopy (UV–vis)

UV-vis is utilized to measure optical properties of materials by recording their absorption, transmittance, and reflectance of in the ultraviolet (200-400 nm) and visible (400–700 nm) regions of the electromagnetic spectrum. It is also referred to as the electronic absorption spectroscopy due to the excitation of electrons from low energy to high-energy molecular orbitals (Electronic Energy Level) when a material is irradiated with light [18, 19].

UV-vis spectrometers consist of monochromators and sample chambers which are placed in alignment with the light source. Before a beam of light is irradiated on a sample, it is first split into various wavelengths by the monochromator. The diffracted spectrum then passes through the slit before it is focused onto the sample. Once the light is illuminated on a sample, it is either absorbed, transmitted or reflected by the sample. Hence, light with various intensities falls on the detector, generating a signal of alternating voltage. The signal is recorded as a plot of wavelength versus intensity of absorbed/transmitted/reflected radiation [20, 21]. Figure **3.5.*4*** present a schematic diagram illustrating the basic operation of a UV-Vis spectrometer.

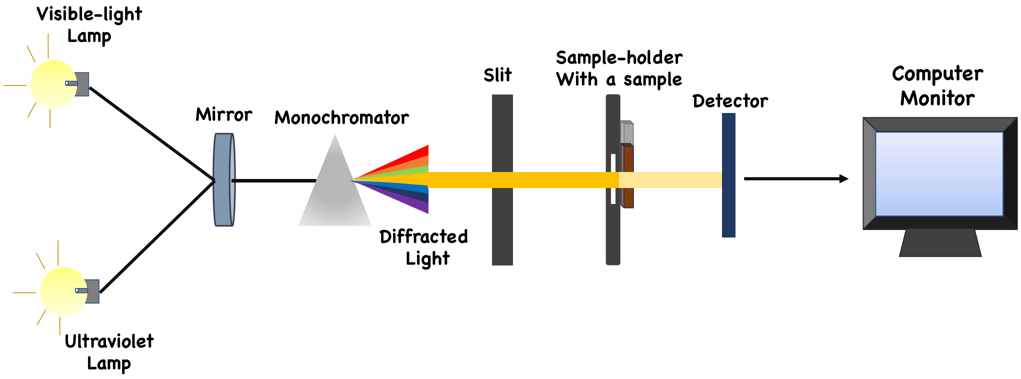

Figure 3.5.4 Schematic diagram of UV-Vis.

3.6. Techniques for Photoelectrochemical studies

3.6.1. Linear Scan Voltammetry (LSV)

LSV is a technique used to obtain qualitative data of occurring electrochemical reactions occurring on electroactive materials [22]. To carry out the measurement, a PEC cell is attached to a three-electrodes (working, counter, and reference) electrochemical equipment typically known as a potentiostat, a function generator, an amplifier, and a recording and display system. A potential is then applied and scanned from lower to higher potentials or vice versa, at a constant scan rate. The flow of current during the reaction is largely influenced by the electrochemical reactions occurring on the electrodes surface, and partly due to the applied potential [22, 23]. The current response of the material can either be cathodic or anodic for n- or p-type materials, respectively (Figure **3.6.*1***) [24]. The photo-current measurements are recorded and plotted as a function of potential on a monitor. The measurements can be done under both dark and illumination conditions to obtain the photo-current response of a photoactive electrode.

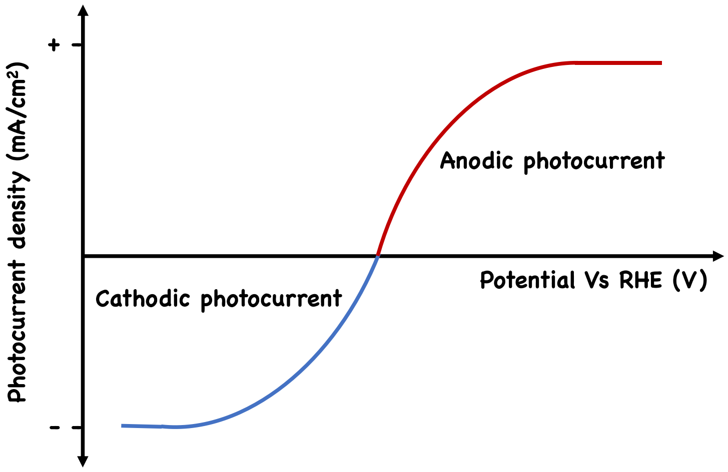

Figure 3.6.1 Schematic illustration of a cathodic and anodic photo-current response

3.6.2. Electrochemical impedance spectroscopy (EIS)

EIS is an electrochemical method commonly used to study the charge transfer processes occurring at the solid/liquid interface and in the region of the electric double layer of an electrode. The current flowing across the PEC cell induces a redox reaction given in Eq. 3.3 at the electrode/electrolyte interface.

$$O + ne^{-} \rightarrow R \qquad \text{Eq. 3.3}$$

where n is the number of transferred electrons, O is the oxidant, and R is the reductant. The rate in which the reactants are consumed and products are generated is dependent on the rate of charge transfer [25, 26]. The transfer of charges after the application of a small sinusoidal signal result in an impedance response basically consisting of resistance, capacitance, and inductance. The impedance responses of a system are most commonly presented in Nyquist plots: a plot of the imaginary component against the real component of the impedance response as shown in Figure **3.6.2**. An equivalent electrical circuit such as the commonly use Randles model given in the inset of Figure **3.6.2** can be used to represent the physical processes occurring on the electrochemical system. The semicircles in a Nyquist plot symbolize the charge transfer processes occurring at the electrode material been measured. The diameter of the semicircles is equivalent to the charge transfer resistance at the solid/liquid interface, denoted by R_{ct} in the Randles circuit. A decrease in R_{ct} indicates an acceleration of charge transfer and migration across the solid/liquid interface. Also, the broadness of the semicircles is related to the capacitance response of the material been studied. Moreover, the intersection of the semicircle with the x-axis is numerically equivalent to the total series resistance (R_s) experience by the measured electrode in the electrochemical system. [27, 28].

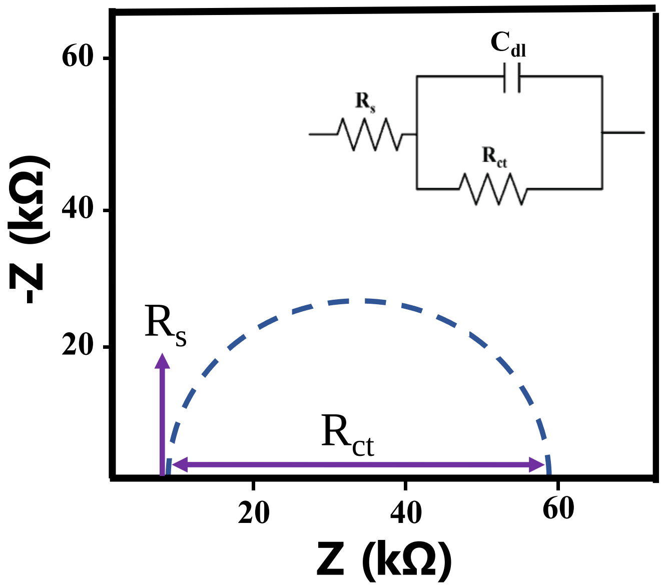

Figure 3.6.2 A simple Nyquist plot with an inset showing the Randles equivalent circuit model.

3.6.3. Mott-Schottky (MS)

MS is typically used to obtain the flat-band potential (V_{fb}) and charge carrier densities of the photoelectrode/electrolyte Schottky barriers. Also, the band edge positions, diffusion lengths and charge carrier lifetimes may be determined using MS analysis [29, 30]. When a photoelectrode and an electrolyte come into contact, the fermi level of the photoelectrode is either higher or lower than that of the electrolyte depending on the p-type/n-type conductivity of the photoelectrode, and through transfer of charges, equilibrium between the two can be obtained. This produces a charge on the photoelectrode which counterbalances the charge of the electrolyte. For a p-type photoelectrode, a negative charge is produced because the charge carrier density is much higher than that of the solution, resulting in a negative slope as given in the MS plot of Figure **3.6.*3*** (a). A positive charge is produced for an n-type photoelectrode, since the charge carrier densities of the photoanode are lower than those in solution which results in a positive slope as given in the MS plot of Figure **3.6.*3*** (b) [5, 30].

By applying bias through a potentiostat, the fermi levels of the semiconductor material are altered, changing the space charge region and eventually changing the level of band bending, until it reaches its flat-band potential where there is no longer any bending of bands or depletion of charges. Flat-band potentials and charge carrier concentrations can be determined for a photocathode and photoanodes using the MS Eq. 3.4 and Eq. 3.5 respectively:

$$\frac{1}{C^2} = \frac{-2}{\varepsilon\varepsilon_0 e A^2 N_A} \left(V - V_{FB} + \frac{kT}{e}\right) \qquad \text{Eq. 3.4}$$

$$\frac{1}{C^2} = \frac{2}{\varepsilon\varepsilon_0 e A^2 N_D} \left(V - V_{FB} - \frac{kT}{e}\right) \qquad \text{Eq. 3.5}$$

where C is the capacitance of the space-charge layer, $\boldsymbol{\varepsilon}$ is the dielectric constant of the material, $\boldsymbol{\varepsilon}_0$ is the vacuum permittivity with a numerical value of 8.85 x 10^{-14} F/cm and *e* is the electronic charge with a value of 1.602 x 10^{-19} C, A is the surface area of the electrode, N_A is the acceptor density, N_D is the donor density, V represent the applied voltage, V_{FB} is the flat-band potential, K is the Boltzmann constant, and T stands for the temperature [5, 29]. charge carrier densities can be obtained from the slope of linear portions of the MS plots, whereas the flat-band potentials are determined from the intercept of the fitted straight line on the potential-axis at $1/C^2 = 0$, in line with Eq. 3.4 and Eq. 3.5 for p- and n-type materials respectively [31].

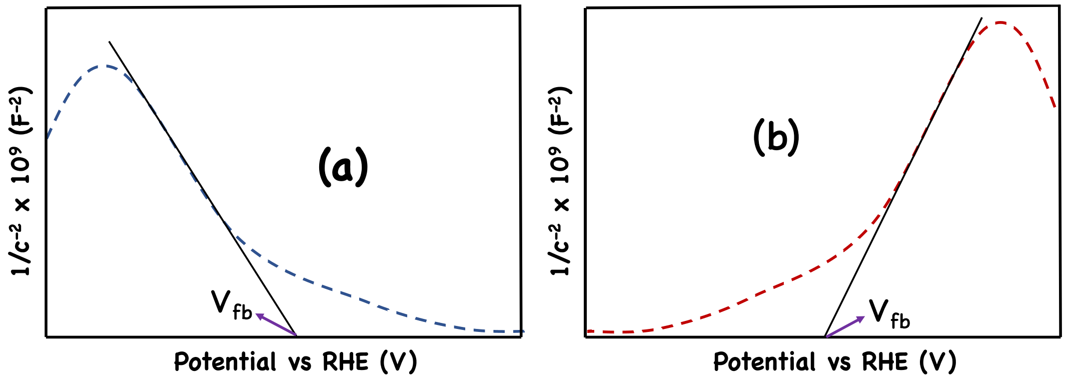

Figure 3.6.3 MS plots of **(a)** p-type and **(b)** n-type semiconductor material.

3.6.4. Chronoamperometry

Chronoamperometry a method commonly used to analyse the photo-stability of photoelectrodes and the redox reactions occurring at the photoelectrode/electrolyte interface at constant a potential, yielding current density as a function of time [5, 32]. Through the application of external bias to a photoelectrode in a PEC cell, the transfer and migration of charges occur across the photoelectrode/electrolyte interface, generating photo-current. When the measurements are performed under dark and illumination conditions, the resulting photo-current response over time are used to determine the photo-stability of the material in electrolyte. Therefore, chronoamperometry measurements depict the stability of the photoelectrode overtime, and they are recorded in current density vs time plots, at constant potentials [32].

References

[1] R. C. Doty, T. R. Tshikhudo, M. Brust, and D. G. Fernig, "Extremely stable water-soluble Ag nanoparticles," *Chemistry of Materials,* vol. 17, no. 18, pp. 4630-4635, 2005.

[2] H. Huang *et al.*, "Ag-decorated highly mesoporous Co3O4 nanosheets on nickel foam as an efficient free-standing cathode for Li-O2 batteries," *Journal of Alloys and Compounds,* vol. 726, pp. 939-946, 2017.

[3] T. Lopes, L. Andrade, H. A. Ribeiro, and A. Mendes, "Characterization of photoelectrochemical cells for water splitting by electrochemical impedance spectroscopy," *international journal of hydrogen energy,* vol. 35, no. 20, pp. 11601-11608, 2010.

[4] R. Van de Krol and M. Grätzel, *Photoelectrochemical hydrogen production*. Springer, 2012.

[5] P. I. Kyesmen, N. Nombona, and M. Diale, "Heterojunction of nanostructured α-Fe2O3/CuO for enhancement of photoelectrochemical water splitting," *Journal of Alloys and Compounds,* vol. 863, p. 158724, 2021.

[6] A. A. Bunaciu, E. G. UdriŞTioiu, and H. Y. Aboul-Enein, "X-ray diffraction: instrumentation and applications," *Critical reviews in analytical chemistry,* vol. 45, no. 4, pp. 289-299, 2015.

[7] A. Kapil, "Applications and Determination of Atomic Structures by X-Ray Crystallography and diffraction," 2015.

[8] A. Chauhan and P. Chauhan, "Powder XRD technique and its applications in science and technology," *J Anal Bioanal Tech,* vol. 5, no. 5, pp. 1-5, 2014.

[9] J. T. Hays, "Line mixing in the rotational Raman spectrum of ethylene," New Mexico State University, 1982.

[10] K. J. Ember *et al.*, "Raman spectroscopy and regenerative medicine: a review," *NPJ Regenerative medicine,* vol. 2, no. 1, pp. 1-10, 2017.

[11] R. L. McCreery, *Raman spectroscopy for chemical analysis*. John Wiley & Sons, 2005.

[12] G. S. Casuccio, S. F. Schlaegle, T. L. Lersch, G. P. Huffman, Y. Chen, and N. Shah, "Measurement of fine particulate matter using electron microscopy techniques," *Fuel processing technology,* vol. 85, no. 6-7, pp. 763-779, 2004.

[13] K. Vernon-Parry, "Scanning electron microscopy: an introduction," *III-Vs Review,* vol. 13, no. 4, pp. 40-44, 2000.

[14] D. McMullan, "Scanning electron microscopy 1928–1965," *Scanning,* vol. 17, no. 3, pp. 175-185, 1995.

[15] C. Hollerith *et al.*, "Energy dispersive X-ray spectroscopy with microcalorimeters," *Nuclear Instruments and Methods in Physics Research Section A: Accelerators, Spectrometers, Detectors and Associated Equipment,* vol. 520, no. 1-3, pp. 606-609, 2004.

[16] J. C. Russ, *Fundamentals of energy dispersive X-ray analysis: Butterworths monographs in materials*. Butterworth-Heinemann, 2013.

[17] D. E. Newbury* and N. W. Ritchie, "Is scanning electron microscopy/energy dispersive X-ray spectrometry (SEM/EDS) quantitative?," *Scanning,* vol. 35, no. 3, pp. 141-168, 2013.

[18] L. Yadav, "Ultraviolet (UV) and visible spectroscopy," in *Organic Spectroscopy*: Springer, 2005, pp. 7-51.

[19] B. M. Tissue, "Ultraviolet and visible absorption spectroscopy," *Characterization of Materials,* 2002.

[20] H.-H. Perkampus, *UV-VIS Spectroscopy and its Applications*. Springer Science & Business Media, 2013.

[21] B. M. Weckhuysen, "Ultraviolet-visible spectroscopy," 2004.

[22] D. Andrienko, "Cyclic voltammetry," *John Wiely & Sons publication, New York,* pp. 3-12, 2008.

[23] A. J. Bard and L. R. Faulkner, "Fundamentals and applications," *Electrochemical methods,* vol. 2, no. 482, pp. 580-632, 2001.

[24] R. Białek, D. J. Swainsbury, M. Wiesner, M. R. Jones, and K. Gibasiewicz, "Modelling of the cathodic and anodic photo-currents from Rhodobacter sphaeroides reaction centres immobilized on titanium dioxide," *Photosynthesis research,* vol. 138, no. 1, pp. 103-114, 2018.

[25] B.-Y. Chang and S.-M. Park, "Electrochemical impedance spectroscopy," *Annual Review of Analytical Chemistry,* vol. 3, pp. 207-229, 2010.

[26] G. Brug, A. L. van den Eeden, M. Sluyters-Rehbach, and J. H. Sluyters, "The analysis of electrode impedances complicated by the presence of a constant phase element," *Journal of electroanalytical chemistry and interfacial electrochemistry,* vol. 176, no. 1-2, pp. 275-295, 1984.

[27] J. Toupin, H. Strubb, S. Kressman, V. Artero, N. Krins, and C. Laberty-Robert, "CuO photoelectrodes synthesized by the sol–gel method for water splitting," *Journal of Sol-Gel Science and Technology,* vol. 89, no. 1, pp. 255-263, 2019.

[28] Y. Chen, A. Li, Q. Li, X. Hou, L.-N. Wang, and Z.-H. Huang, "Facile fabrication of three-dimensional interconnected nanoporous N-TiO2 for efficient photoelectrochemical water splitting," *Journal of materials science & technology,* vol. 34, no. 6, pp. 955-960, 2018.

[29] S. P. Harrington and T. M. Devine, "Analysis of electrodes displaying frequency dispersion in Mott-Schottky tests," *Journal of The Electrochemical Society,* vol. 155, no. 8, p. C381, 2008.

[30] K. Gelderman, L. Lee, and S. Donne, "Flat-band potential of a semiconductor: using the Mott–Schottky equation," *Journal of chemical education,* vol. 84, no. 4, p. 685, 2007.

[31] T. Lopes, L. Andrade, F. Le Formal, M. Gratzel, K. Sivula, and A. Mendes, "Hematite photoelectrodes for water splitting: evaluation of the role of film thickness by impedance spectroscopy," *Physical Chemistry Chemical Physics,* vol. 16, no. 31, pp. 16515-16523, 2014.

[32] J. Wang and H. Zeng, "Recent advances in electrochemical techniques for characterizing surface properties of minerals," *Advances in Colloid and Interface Science,* p. 102346, 2020.

Chapter 4

4.0 Results and discussion

4.1. Introduction

In this section, results obtained from the enhancement of photo-current response and photo-stability in electrolyte of pristine dip-coated CuO thin films are discussed. The films were prepared at different withdrawal rates, film thicknesses, and annealing temperatures to optimize the processing parameters for preparing the films for improvement of their photoelectrochemical (PEC) response. The structural, morphological, optical, and PEC properties of the pristine CuO films are presented. Pristine CuO thin films were coated with a protective layer of Activated Charcoal (AC) using spray pyrolysis; and Silver (Ag) and Gold (Au) nanoparticles (NPs) via drop casting to improve their photo-stability in the electrolyte. The structural, morphological, and optical properties of the modified CuO films are also presented. Furthermore, the photo-current response and photo-stability observed for the pristine CuO, CuO/AC, CuO/Ag, and CuO/Au thin films are discussed in detail.

4.2. Optimization of processing parameters of dip-coated copper (II) oxide films for photoelectrochemical water-splitting

In this section, the results obtained from the optimization of withdrawal rates, film thickness, and annealing temperature for dip coated CuO photocathodes are presented and discussed. The influence of the processing parameters on the structural, optical and PEC properties of the CuO films is explained. The photo-stability of pristine CuO films are also discussed.

4.2.1 Structural properties

The structural properties of CuO thin films were characterized using XRD within a 2 theta range of 20 and 70° and the results are shown in Figure ***4.2.1*** (a), (b) and (c) for samples prepared at different withdrawal rates, with different thicknesses and annealed at various temperatures respectively. Diffraction peaks at ($\bar{1}11$) and (111) planes were observed on the

XRD patterns confirming the monoclinic crystal structure of the prepared CuO films with lattice parameters a = 4.64 Å, b = 3.4 Å, c = 5.09 Å, β = 99.5° according to JCPDS no. 05–0661 [1, 2]. Other weak reflections were also observed at (020) and $(\bar{1}13)$ corresponding to those of CuO films. No obvious peak shift or Bragg reflections for copper (Cu) or copper (I) oxide (Cu_2O) were observed, confirming the high purity of the CuO films prepared. It was observed that the intensity of the diffraction peaks increases with increasing withdrawal speed (Figure **4.2.*1*** (a)). This is due to the increased thickness of the films with increasing withdrawal speed [3]. Films with different numbers of deposited layers also showed an increase in the intensity of the diffraction peaks because of increasing film thickness [4]. Films consisting of seven layers which were annealed at different temperatures also show enhancement in their diffraction peak intensities with increasing annealing temperature. This is attributed to improvement in the crystallinity of the thin films with increasing calcination temperature [2, 5].

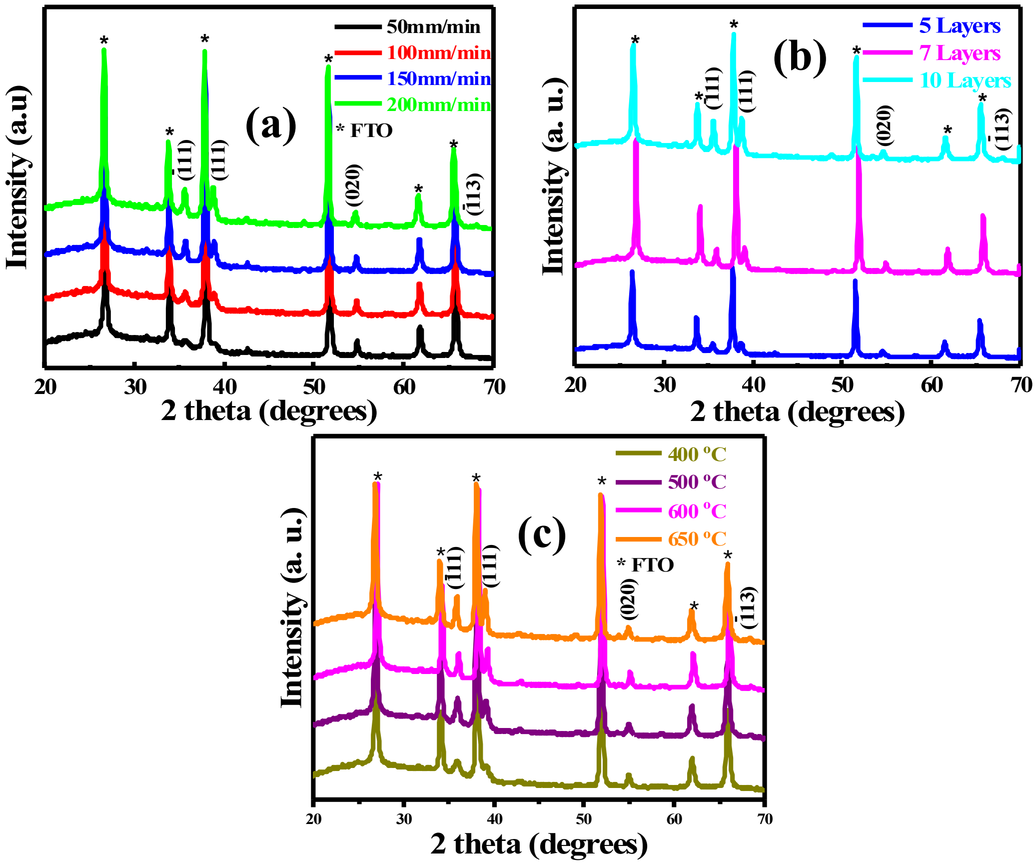

Figure 4.2.1 XRD patterns of CuO thin films (a) withdrawn from the precursor at different withdrawal speeds, (b) consisting of different number of film layers, and (c) annealed at various temperatures.

The peaks at $(\bar{1}11)$ were used to obtain the full width at half maximum (FWHM) and crystal size values of the prepared CuO films. This was done to understand the impact of withdrawal speed, film thickness, and annealing temperature on the crystallization of the films. The approximate crystal sizes (*D*) of the samples were calculated using the Debye-Scherrer formula given in Eq. 4.2.1 [1].

$$\mathrm{D} = \frac{k\lambda}{\mathcal{B}cos\theta} \qquad \text{Eq. 4.2.1}$$

where *k* is the shape factor (0.9), λ is the wavelength of incident X-ray (λ = 0.15418 nm for Cu-Kα radiation), β is the FWHM and θ is the Bragg angle [6].

The FWHM and crystal size values of the CuO films prepared at different withdrawal rates, consisting of films with different numbers of film layers and annealed at various temperatures are given in Table **4.2.*1***. For films prepared using different withdrawal speeds, the films withdrawn at 150 mm/min and 50 mm/min were observed to have the highest and least crystal sizes of 19.4 and 8.5 nm respectively. An increase in the crystal size values of thin films is an indication of improved crystallization. The withdrawal speed of 150 mm/min was used to prepare CuO films of different number of deposited layers for the optimization of film thickness due to the high crystallinity observed for the films. This was because of the crucial role that high film crystallization has on PEC water-splitting as it promotes efficient charge migration and separation [7]. Increased crystal sizes influence the level of band-bending during photocatalysis, preventing charge recombination, and consequentially enhancing the photo-current response of the films [8]. There is no significant difference in the crystal sizes of films consisting of different layers since they were all annealed at the same temperature of 600°C. Lastly, the crystal sizes of the films increase with annealing temperature. The film annealed at 650 °C shows the highest crystallite size value of 21.01 nm. This was due to the increase in thermal energy by the particles with annealing temperature which promotes migration of atoms during crystal formation, leading to larger crystallites [5]. Larger crystal sizes resulting from increasing annealing temperature can positively influence charge separation and transportation during PEC water-splitting as earlier explained [5].

Table 4.2.1 XRD analysis showing FWHM and crystal sizes of CuO thin films withdrawn from the precursor at different speeds, consisting of different number of film layers, and annealed at various temperatures.

Processing parameters	**Sample**	**2 theta**	**FWHM**	**Crystal size (nm)**
Withdrawal speed	**50 mm/min**	35.66	0.89	8.50
	100 mm/min	35.62	0.63	12.01
	150 mm/min	35.68	0.39	19.40
	200 mm/min	35.80	0.41	18.45
Film thickness				
(150 mm/min)	**5 Layers**	35.68	0.39	19.04
	7 Layers	36.08	0.38	19.89
	10 Layers	35.76	0.37	20.44
Annealing temperature	**400°C**	35.89	0.76	9.96
(7 Layers)	**500°C**	35.93	0.49	15.43
	600°C	36.08	0.38	19.89
	650°C	35.84	0.36	21.01

The Raman spectra of the CuO films were obtained to study the vibration of phonon modes of the films to extract more structural information. The spectra are shown in Figure **4.2.*2*** (a), (b) and (c) for samples prepared at different withdrawal rates, consisting of different film layers and annealed at various temperatures respectively. The Raman spectra for the CuO films revealed $1A_g$ and $2B_g$ Raman active phonon modes for the films. The peak at 302 cm^{-1} is indexed to the A_g mode and the ones at 250 and 638 cm^{-1} are assigned to the $2B_g$ modes, respectively. The phonon modes belonging to Cu, Cu_2O, or other forms of copper oxide were not detected, confirming the high quality of the prepared CuO films. Raman peaks intensities of CuO thin films increase with increasing withdrawal speed from 50–150 mm/min. The film withdrawn at 200 mm/min did not show much change in its Raman intensity compared to those prepared at 150 mm/min because there was no significant difference in their crystallinity (Table **4.2.*1***). The Raman peaks of CuO films consisting of 5-10 layers did not show any significant difference in their intensities. This was because the films had similar crystallinity as observed in their XRD analysis (Table **4.2.*1***). Figure **4.2.*2*** (c) reveals broadened Raman peaks for the films prepared at low annealing temperatures of 400-500 °C caused by the quantum confinement effect of the CuO nanoparticles [9].

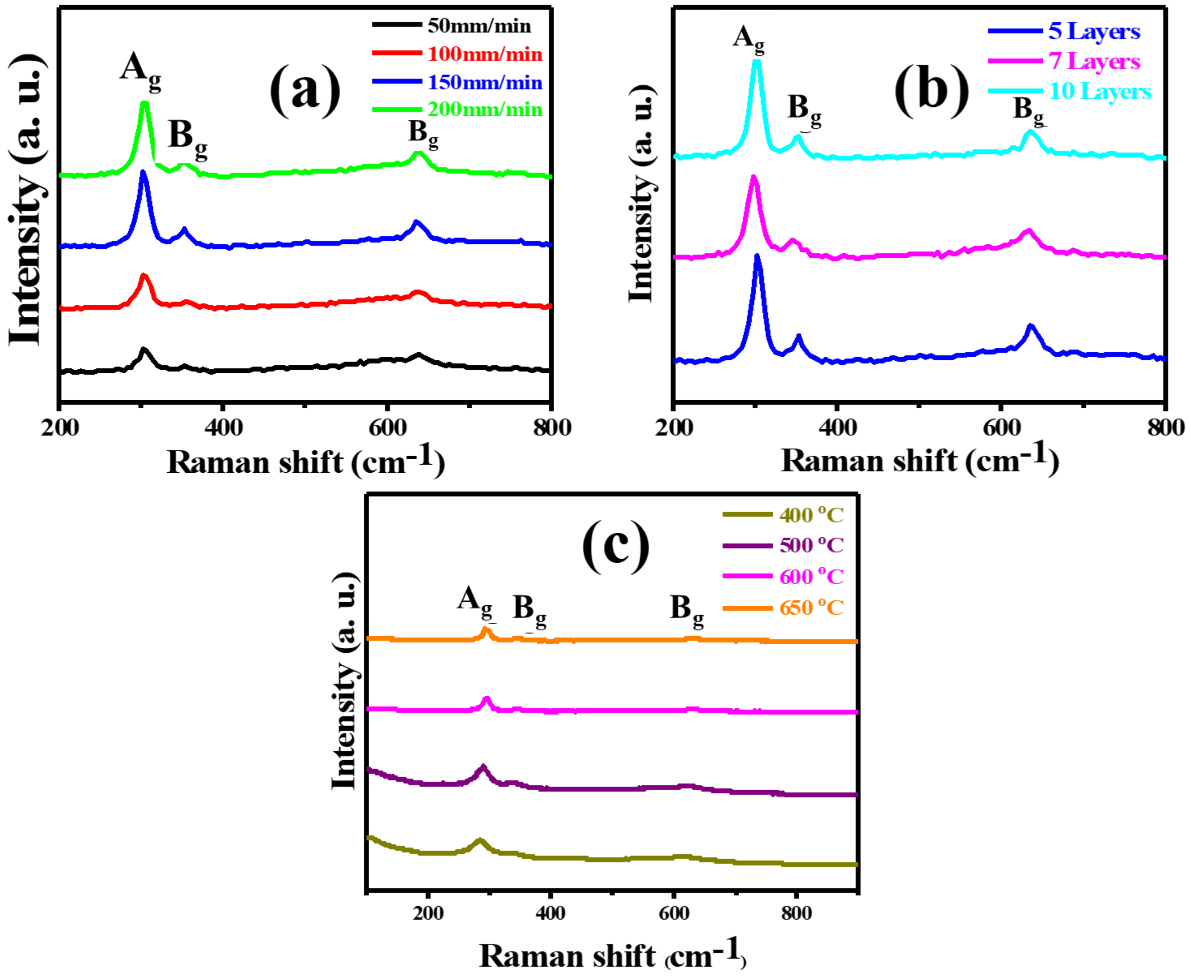

Figure 4.2.2 Raman spectra of CuO thin films **(a)** withdrawn from the precursor at different speeds **(b)** consisting of different number of film layers, and **(c)** annealed at different temperatures.

The high Raman intensities exhibited by films prepared at 150 and 200 mm/min, which has been associated to improvement in their crystal sizes [10], can lead to enhance charge separation and migration during PEC water-splitting. Similarly, films annealed at elevated temperatures of 600-650 °C revealed sharp and narrowed Raman peaks compared to the ones sintered at 400-500 °C which is also attributed to improvement in their crystallinity [11]. The broadened Raman peaks observed for the films prepared at 400-500 °C has been associated to the quantum confinement effect resulting from smaller CuO crystals. In view of these, CuO films annealed at 600-650 °C are expected to yield better PEC response compared to the ones treated at lower temperatures because of their improved crystallinity, in line with other observations in literature [5, 12].

4.2.2 Surface morphology and film thickness

The pristine CuO films were characterized using FE-SEM to understand the impact of sample processing parameters on the surface morphology of the Films. The morphology of all thin films revealed spherical nanoparticles which are homogeneously distributed throughout the substrates. Figure **4.2.*3*** (a), (b), (c), and (d) presents the surface morphology of CuO films prepared at 50, 100, 150, and 200 mm/min respectively**.** The average grain sizes for the thin films withdrawn at the speeds of 50, 100, 150, and 200 mm/min were estimated as 19.60, 20.49, 25.13, and 25.82 nm with the standard deviation of 6.76, 10.16, 9.52, and 8.89 nm respectively. A slight increase in the porosity of films prepared at speeds of 150 mm/min and above was observed. According to Brinker et. al, 1991 an increase in the withdrawal speed results in an enhancement of the film's thickness, and thicker films take time to dry, leading to the stiffening of the films, consequently increasing porosity [3].

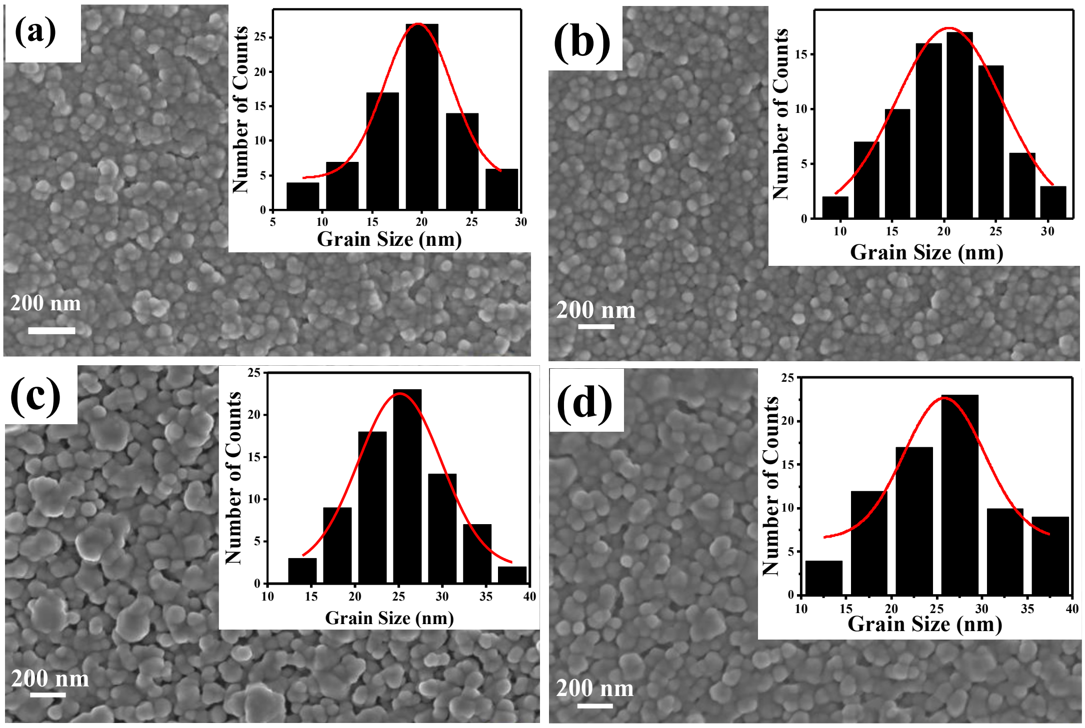

Figure 4.2.3 SEM micrographs of CuO thin films prepared at withdrawal speeds of **(a)** 50 mm/min **(b)** 100 mm/min **(c)** 150 mm/min **(d)** 200 mm/min: the corresponding histograms of the particle size distribution of the films are presented their insets.

The surface morphology of CuO films consisting of 5, 7, and 10 layers, prepared at 150 mm/min are given in Figure 4.2.4 (a), (b) and (c) respectively. There is no significant difference in the morphologies and grain sizes of the films. This is contradictory compared to some morphology studies of CuO films reported in literature where the surface properties of the films vary in relation to film thickness [4, 13, 14]. This contradiction was because the annealing temperature of the films at 600 °C was done after each of the dip-coated layers were treated at 120 °C and 300 °C respectively, which was sufficient to initiate significant film crystallization [15]. The average grain size of the films which were deposited with 5, 7, and 10 layers were estimated as 25.13, 26.37, and 24.92 nm with a standard deviation of 9.52, 9.19, and 3.03 nm, respectively. No substantial change was observed in the grain sizes of the films. Shariffudin *et. al*, *2015* reported increasing grain sizes for CuO films at higher film thicknesses, whereas at lower film thicknesses, the grain sizes did not differ much [13].

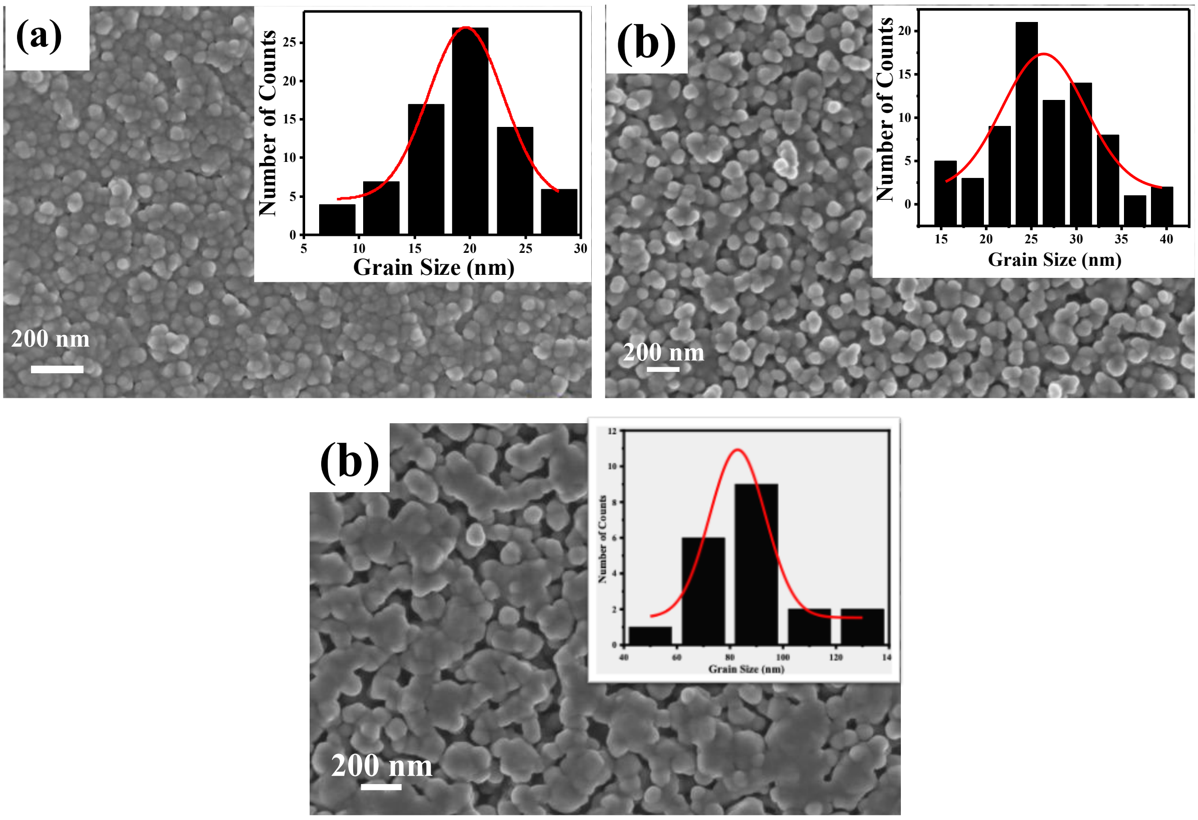

Figure 4.2.4 SEM micrographs of thin films deposited with **(a)** 5 Layers **(b)** 7 Layers and **(c)** 10 Layers of CuO together with the corresponding histograms of their particle size distribution.

The surface morphology of CuO films annealed at different temperatures are also given in

Figure **4.2.5** (a), (b), (c) and (d)**,** the samples were annealed at 400, 500, 600, and 650°C respectively. An increase in the grain size of the films was observed with increasing annealing temperatures. Figure **4.2.5** (d) shows a significant difference in the morphology of the film annealed at 650 °C compared to the ones treated at 400, 500, and 600 °C. The surface appears to be compact, smooth, and extremely agglomerated. Furthermore, the nanoparticles seem to have coalesced into larger nanostructures which may be due to a large amount of tension over the surface of the films caused by the high annealing temperature [16]. The average grain size of the films annealed at 400, 500, and 600°C was estimated as 12.85, 19.92, and 26.37 nm with the standard deviation of 3.85, 5.67, and 9.91 nm, respectively. The average grain size of the nanoparticles of the thin films annealed at 650 °C could not be estimated due to extreme agglomeration and grain boundaries that are not well defined. High particle agglomeration has been reported to limit charge transport and PEC response of photoelectrodes during water-splitting [17, 18].

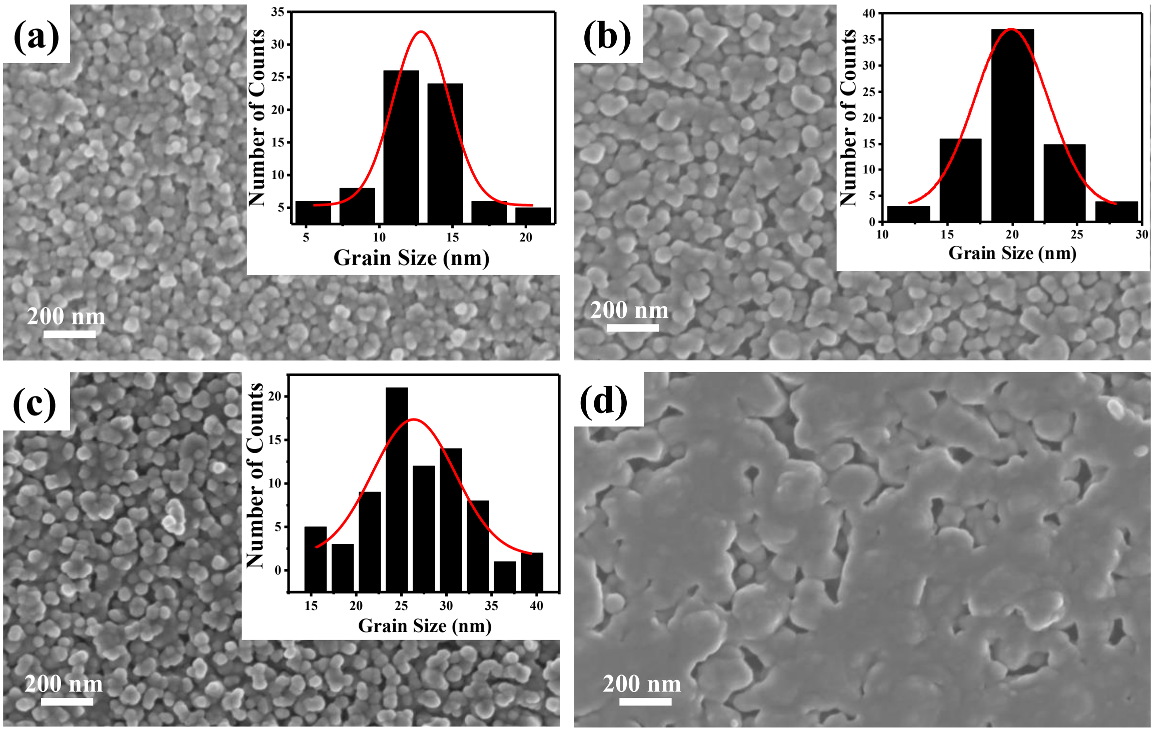

Figure 4.2.5 FE-SEM micrographs of CuO thin films prepared at withdrawal speeds of **(a)** 50 mm/min **(b)** 100 mm/min **(c)** 150 mm/min **(d)** 200 mm/min: the corresponding histograms of the particle size distribution of the films are presented in their insets.

The FE-SEM cross-sectional views of CuO thin films consisting of 5 layers and prepared at 50, 100, 150, and 200 mm/min withdrawal rates were obtained to estimate their thicknesses and are presented in Figure **4.2.6** (a), (b), (c) and (d) respectively. The average thicknesses of the films were estimated using ImageJ software to be 239.7, 277.3, 317.4, and 355.2 nm for samples prepared at 50, 100, 150, and 200 mm/min withdrawal rates respectively. The film thickness increases with increasing withdrawal rates. It is a result of the dragging caused by the viscosity of the precursor solution on the moving substrate at higher withdrawal speeds when using the dip-coating approach [19, 20]. The increase in thickness with increasing withdrawal rates also corresponds with the improvement in crystal sizes observed in the XRD analysis (Table **4.2.*1***). According to Aydemir, *2015* increasing film thickness is directly proportional to the withdrawal speed of the films. In succession, increasing film thickness increases the crystallite size [20]. Similarly, Akaltun, *2015* and Saâd et.al, *2020* reported increasing film thickness which correspond to the crystalline sizes of the films [2, 4].

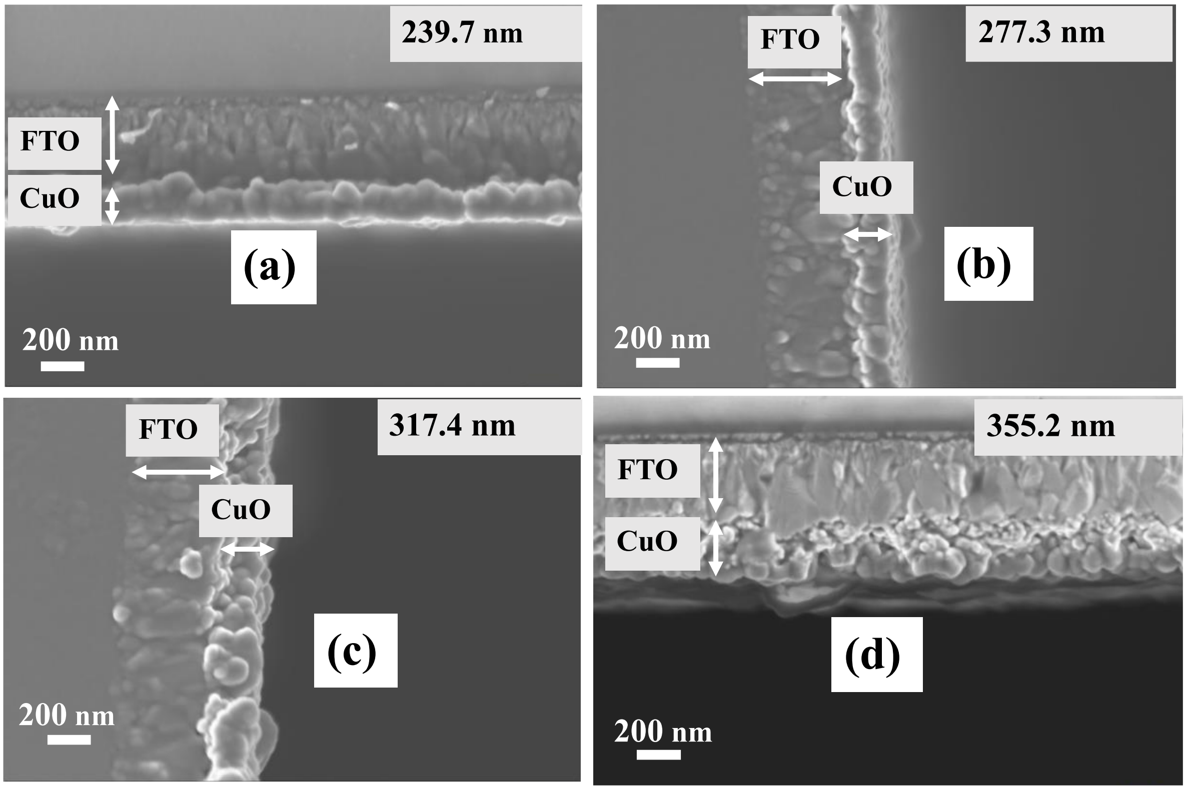

Figure 4.2.6 FE-SEM cross-sectional views of CuO thin films prepared using withdrawal speeds of **(a)** 50 mm/min **(b)** 100 mm/min **(c)** 150 mm/min **(d)** 200 mm/min.

The FE-SEM cross-sectional views of the CuO thin films prepared at 150 mm/min withdrawal speed, consisting of 5, 7, and 10 layers are presented in Figure **4.2.7** (a), (b) and (c). The thickness of the CuO films was estimated to be 317.4, 432.8, and 693.6 nm for films consisting of 5, 7, and 10 layers respectively. As expected, the thickness of the films increases with the increasing number of film layers. The cross-sectional views of CuO thin films consisting of 7 layers and annealed at 400, 500, and 650 °C were not characterized since annealing temperature was not expected to have a significant influence on the film's thickness. This was because each layer of the films was treated at 120 and 300 °C prior to annealing. In addition, Akgul *et. al, 2014* previously reported uniform thicknesses for CuO thin films which were annealed at different temperatures [5]. An optimal film thickness is important for enhancing the PEC performance of CuO photocathodes because of the short diffusion length of 200 nm [15].

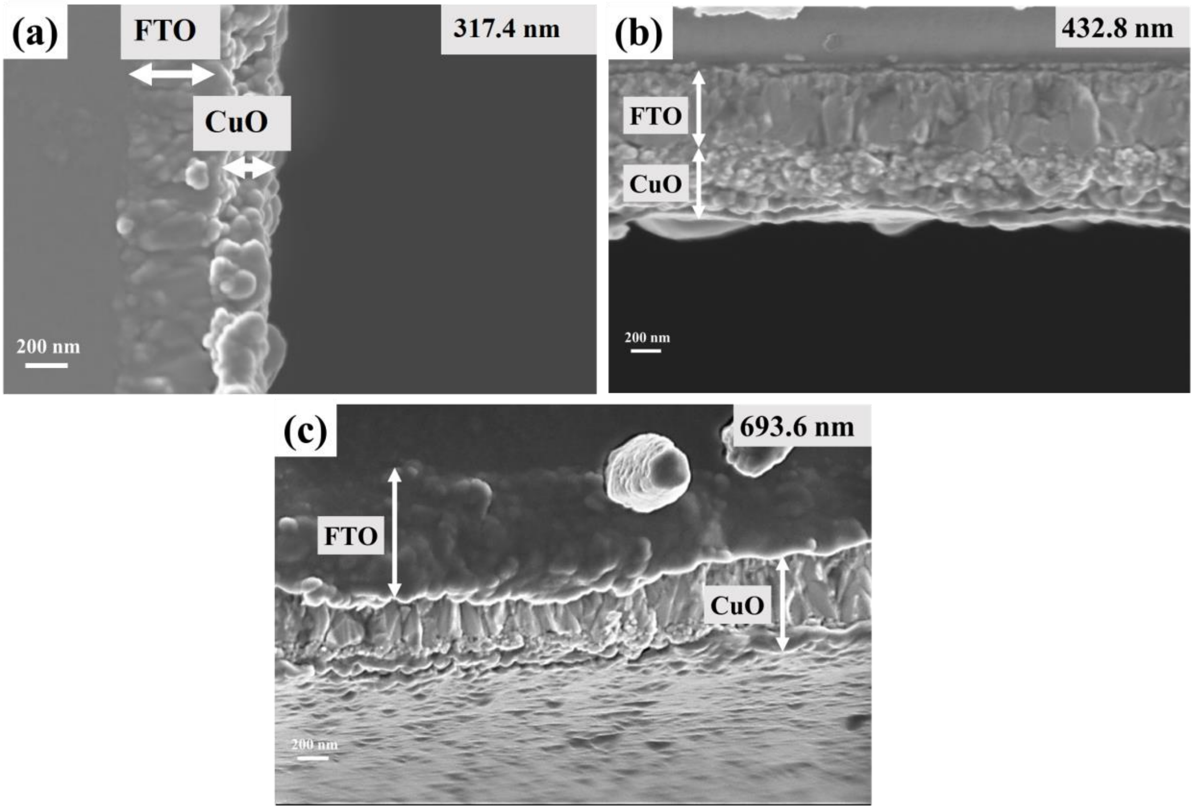

Figure 4.2.7 FE-SEM cross-sectional view of thin films deposited with **(a)** 5 **(b)** 7 and **(c)** 10 Layers of CuO.

4.2.3. Elemental composition

The elemental compositions of the CuO films were confirmed using Energy Dispersive X-ray Spectroscopy (EDS) to verify the presence of possible impurities in the films. Figure **4.2.8** (a), (b), (c), and (d) shows the results of the EDS analysis done on CuO samples prepared at withdrawal rates of 50, 100, 150, and 200 mm/min respectively. The analysis confirms the presence of oxygen (O) and copper (Cu) as expected since they were the constituent elements of CuO. Also, tin (Sn) and a small amount of silicon (Si) were detected in the EDS analysis of all the films. The Sn observed in the films resulted from the SnO content of FTO substrates used for the film's deposition, while the Si detected was because of the quarts content of glass in the glass/FTO substrates [1]. The EDS analysis done on CuO films prepared at 150 mm/min, consisting of 5, 7, 9 layers and annealed at 600°C are shown in Figure 4.2.9 (a), (b) and (c) while those annealed at 400, 500, 600 and 650°C are presented in Figure **4.2.*10*** (a), (b), (c) and (d), respectively. The results revealed the same elemental compositions as observed in Figure **4.2.*8*** for films prepared at different withdrawal rates.

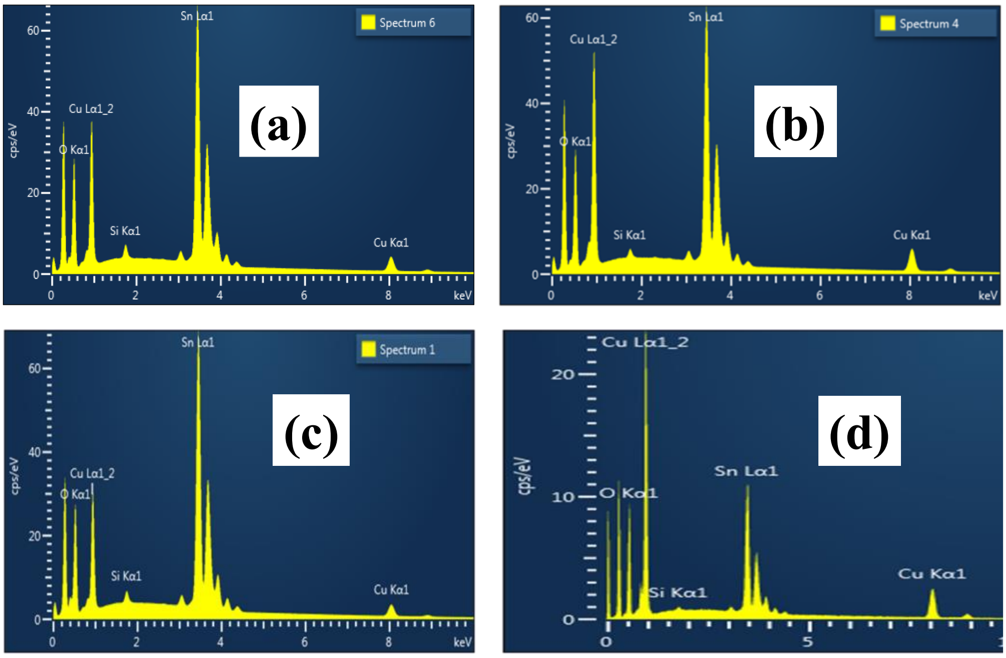

Figure 4.2.8 EDS analysis of CuO thin films withdrawn from the precursor at the speeds of **(a)** 50 mm/min **(b)** 100 mm/min **(c)** 150 mm/min **(d)** 200 mm/min.

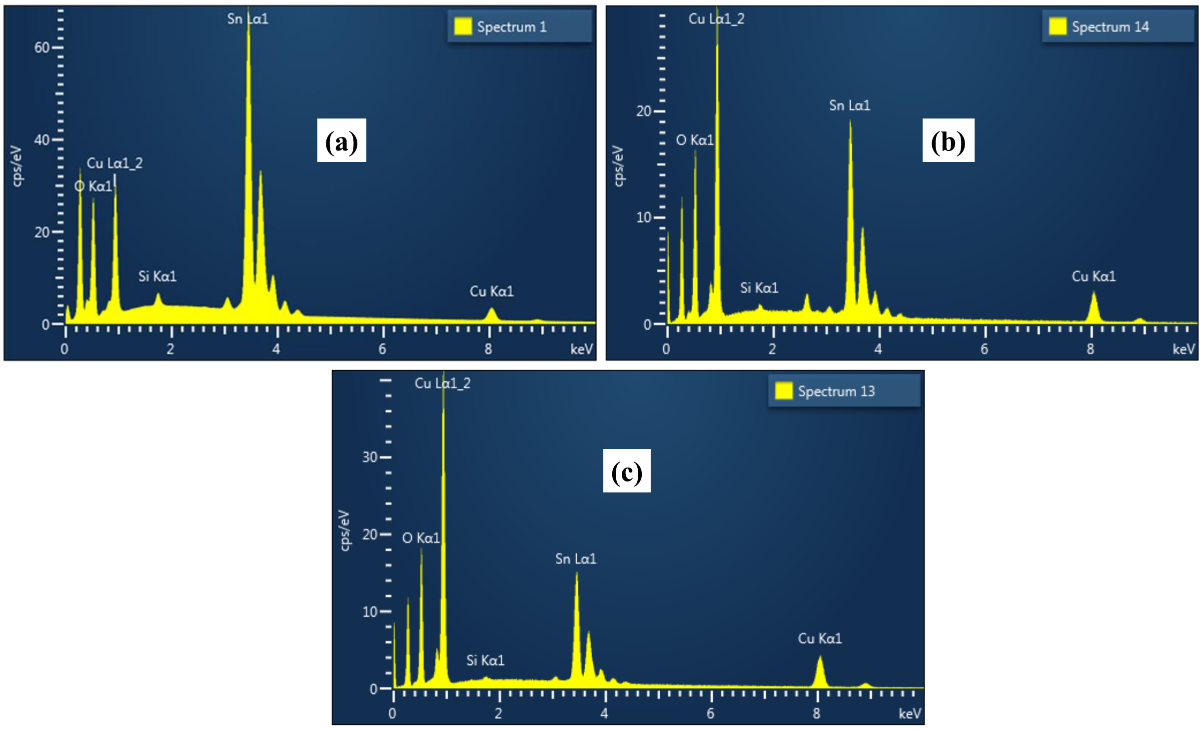

Figure 4.2.9 EDS analysis of the CuO thin films deposited to consist of (a) 5 Layers (b) 7 Layers and (c) 10 Layers.

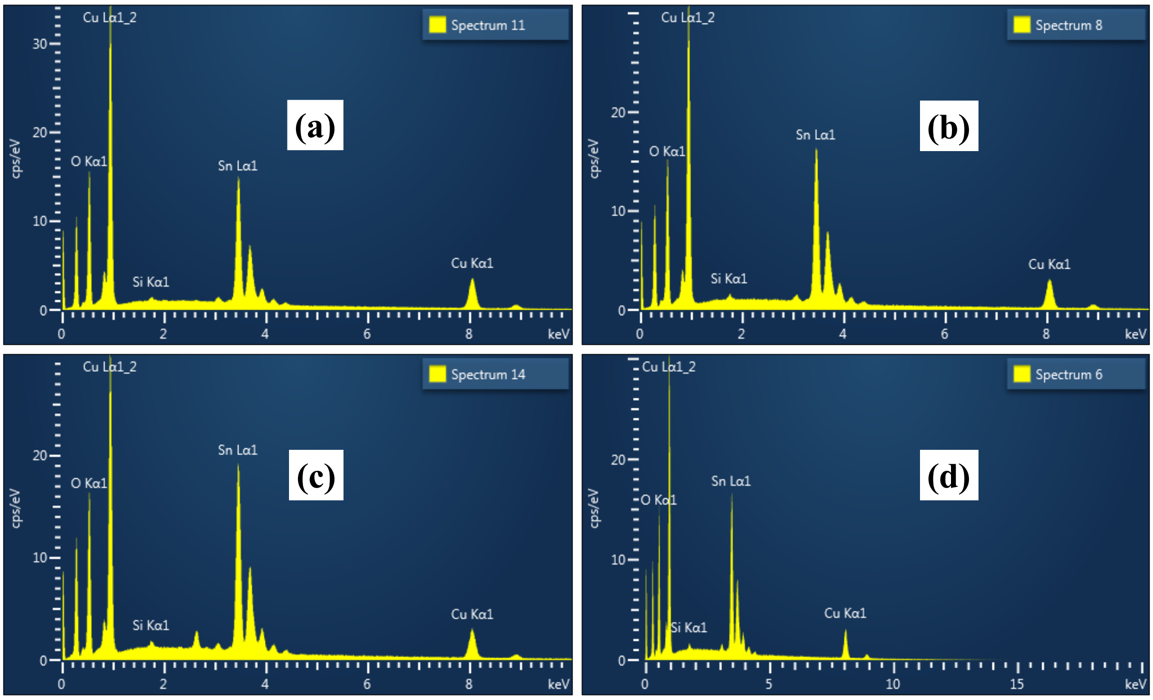

Figure 4.2.10 EDS analysis of CuO thin films annealed at different temperatures of **(a)** 400°C **(b)** 500°C **(c)** 600°C and **(d)** 650°C.

4.2.4 Optical properties

UV-Vis spectroscopy was done to investigate the optical absorption, transmittance, and indirect bandgap of the CuO thin films. Figure **4.2.11** (a), (b), and (c) show the optical absorption of CuO thin films prepared at several withdrawal rates, consisting of different film layers and annealed at various temperatures respectively. The CuO thin films largely absorb in the visible region, with a slight absorption in the near-infrared region. The absorption of the CuO films increases with increasing withdrawal speed (Figure **4.2.11** (a)) and the number of film layers (Figure **4.2.*11*** (b)). This is due to the increase in film thickness with increasing withdrawal rate and number of layers [21]. Also, improved absorption was observed for the films with increasing annealing temperature (Figure **4.2.11** (c)). Enhanced photo-absorbance in the visible region will lead to the increased production of electron-hole pairs, which have the potential to separate and migrate to the surface of the semiconductor for hydrogen production. The insets of Figure **4.2.11** (a), (b), and (c) present the transmittance of the samples prepared at several withdrawal rates, consisting of different film layers, and annealed at various temperatures respectively. The transmittance behaviours of the CuO films are in good agreement with their absorption patterns as expected.

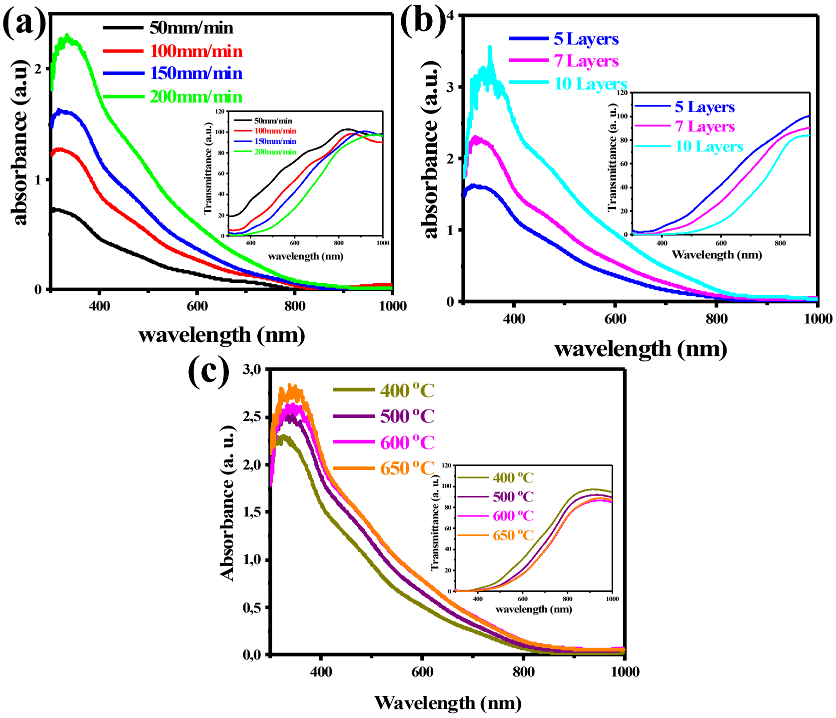

Figure 4.2.11 UV–Vis absorption spectra of CuO thin films **(a)** withdrawn from the precursor at different speeds **(b)** consisting of different number of film layers, and **(c)** annealed at different temperatures, with the insets showing their transmittance measurements.

The Tauc plots for the indirect transitions of CuO thin films prepared at different withdrawal speeds, deposited with the different number of film layers, and annealed at different temperatures are presented in Figure ***4.2.12*** (a), (b), and (c) respectively. The plots were derived from the absorption spectra of the films and were used to approximate the values of their optical bandgaps using the Tauc relation given in Eq. 4.2.2 [22]:

$$\alpha h\upsilon = A(h\upsilon - E_g)n \qquad \text{Eq. 4.2.2}$$

where α is the absorption coefficient, A is a characteristic parameter that is independent of photon energy, *hv* is the photon energy, Eg is the optical bandgap, and $n = \frac{1}{2}$ and 2 for the direct indirect transitions respectively [5, 21]. Straight lines were extrapolated from the Tauc plots, and their intercepts on the *hv*-axis at $(\alpha hv)^{1/2} = 0$ were recorded as the approximate indirect bandgap of the films [23]. The indirect bandgaps for the films were estimated to be 1.34 ± 0.04 eV for all films. [5, 21]. The estimated bandgap of the films is low compared to the values reported for the films in some literature [2, 4]. Low bandgaps are associated with the wide range of photo-absorbance in the visible region which can positively influence the generation and separation of electron-hole pairs for photocatalytic reactions [24, 25].

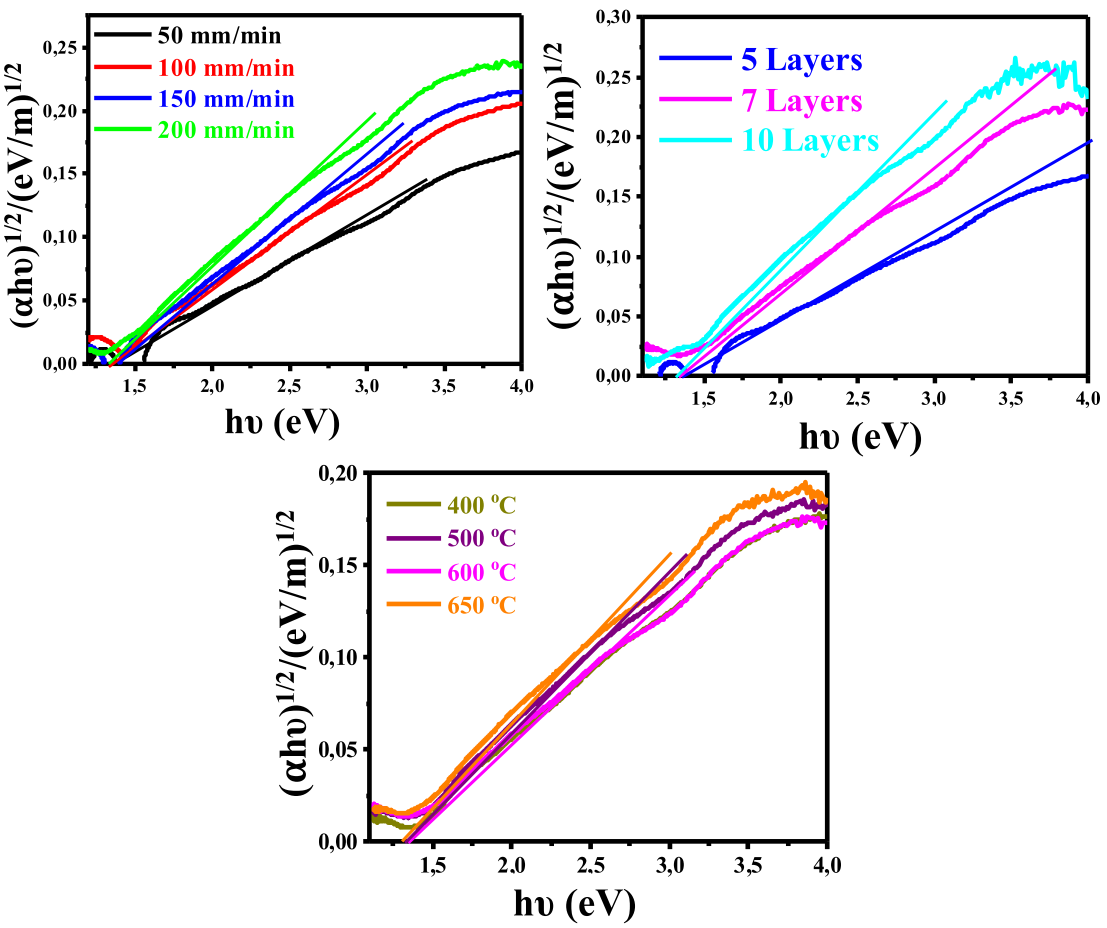

Figure 4.2.12 Tauc approximation for the indirect bandgaps of CuO thin films **(a)** withdrawn from the precursor at different speeds, **(b)** consisting of different number of film layers, and **(c)** annealed at different temperatures.

4.2.5 Photoelectrochemical properties

LSV measurements were done to obtain the photo-current response of the CuO films. Figure **4.2.*13*** (a), (b), and (c) show the LSV results for measurements done on the CuO photocathodes under dark and illumination conditions for samples prepared at several withdrawal rates, consisting of different film layers and annealed at various temperatures respectively. For samples prepared at varying withdrawal rates, the photo-current increases with increasing withdrawal rate with values of 1.6 and 2.0 mA/cm^2 at 0.35 V vs RHE obtained for the film prepared at 150 and 200 mm/min respectively. The high photo-current values obtained are attributed to the enhancement of the crystallinity of the films and photo-absorption, resulting from their relatively increased film thickness. [26]. The enhanced grain size helped to promote the photo-current response of films by decreasing the grain boundaries which often function as charge recombination sites on the surface of the films [27-29]. Furthermore, after the optimization of the film thickness and annealing temperature, the maximum photo-current density of 2.9 mA/cm^2 at 0.35 V vs RHE was observed for films consisting of 7 layers and annealed at 600 ℃. The optimized film thickness of about 432.8 nm obtained for films with 7 layers contributed to the maximal photo-current density obtained. This was evident as a further increase in the number of film layers to 10, lead to a decline in photo-current (Figure **4.2.*13*** (b)). Also, increasing annealing temperatures improve the grain size and crystallinity of the films, enhancing photo-current response, until it reaches its maximum for films annealed at 600°C. Above this annealing temperature, the photo-current density declined to generate a photo-current density of 1.3 mA/cm2 at 0.35 V vs RHE for films calcined at 650℃ [29-31]. In brief, the maximum photo-current density obtained for the CuO films is attributed to the optimized film thickness, optical absorption, and crystallinity of the films which promotes the photogeneration of electron-hole pairs and charge transport during photocatalysis. An extremely low photo-current was observed for the films annealed at 400°C. This has been ascribed to the poor crystallinity of the films which limit its charge mobility and the movement of electrons to the film’s surface.

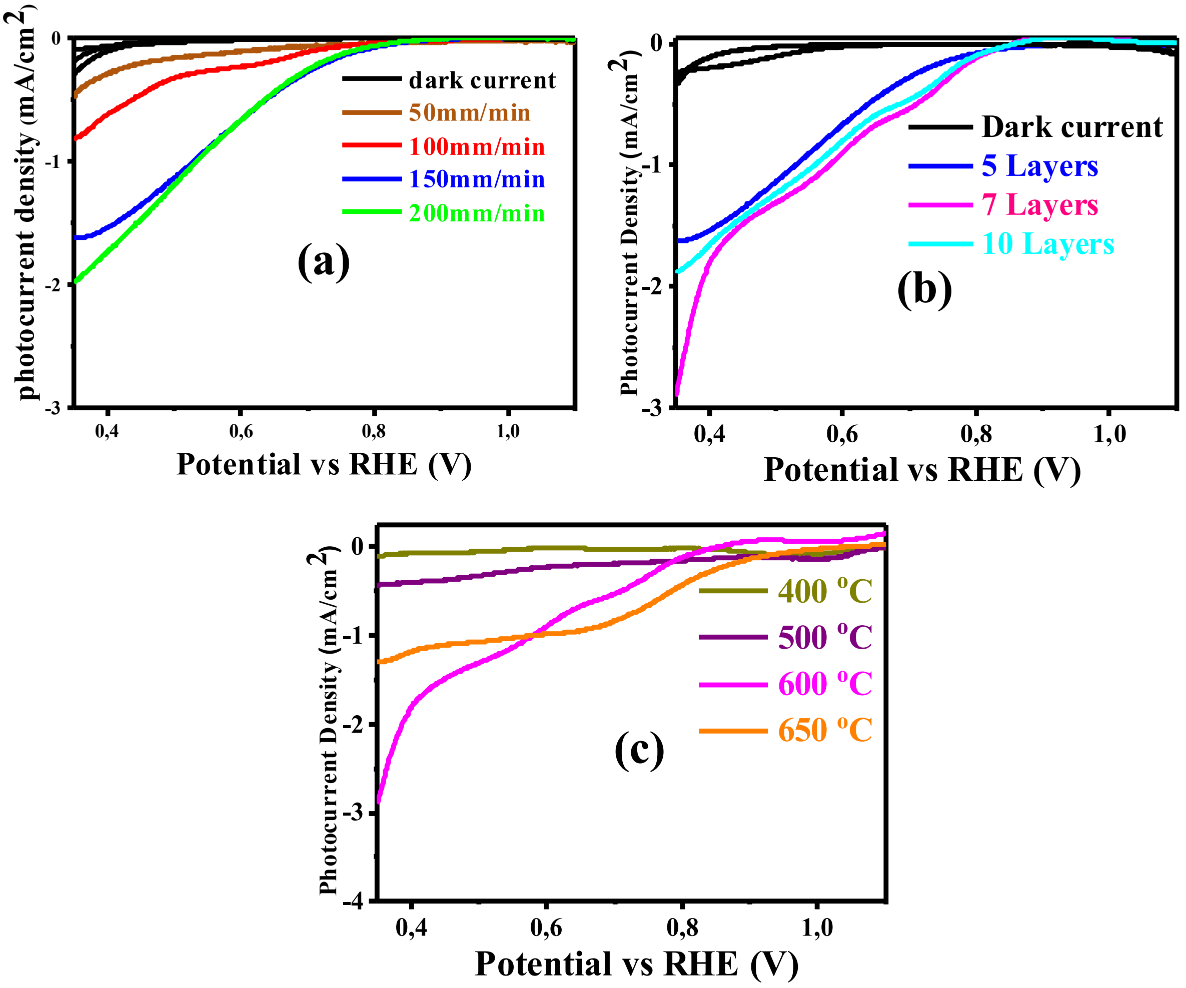

Figure 4.2.13 Photo-current density for CuO photocathodes: **(a)** withdrawn from the precursor at different speeds, **(b)** consisting of different number of film layers, and **(c)** annealed at different temperatures.

Electrochemical Impedance Spectroscopy (EIS) measurements were performed on CuO photocathodes to analyse charge transfer processes occurring at the semiconductor/electrolyte interface. Figure **4.2.*14*** (a), (b), (c) shows the Nyquist plots of the EIS experimental and fitted data for samples prepared at different withdrawal rates, consisting of different film layers, and annealed at various temperatures respectively. The circuit model used to fit the EIS experimental data obtained for the films is given in Figure **4.2.*14*** (d). Rs represents the total series resistance caused by the FTO, electrolyte, and connecting wires and its value is equivalent to the intersection of the semi-circle with the real part of impendence [1, 32], whereas the Constant Phase Element (CPE) denotes the capacitance of the electric double-layer [33]. Rct refers to the charge transfer resistance across the solid/liquid interface for hydrogen evolution reaction, and it is represented by the semi-circle diameters of the Nyquist plot. The smaller the semi-circle, the lower the charge transfer resistance [32, 34].

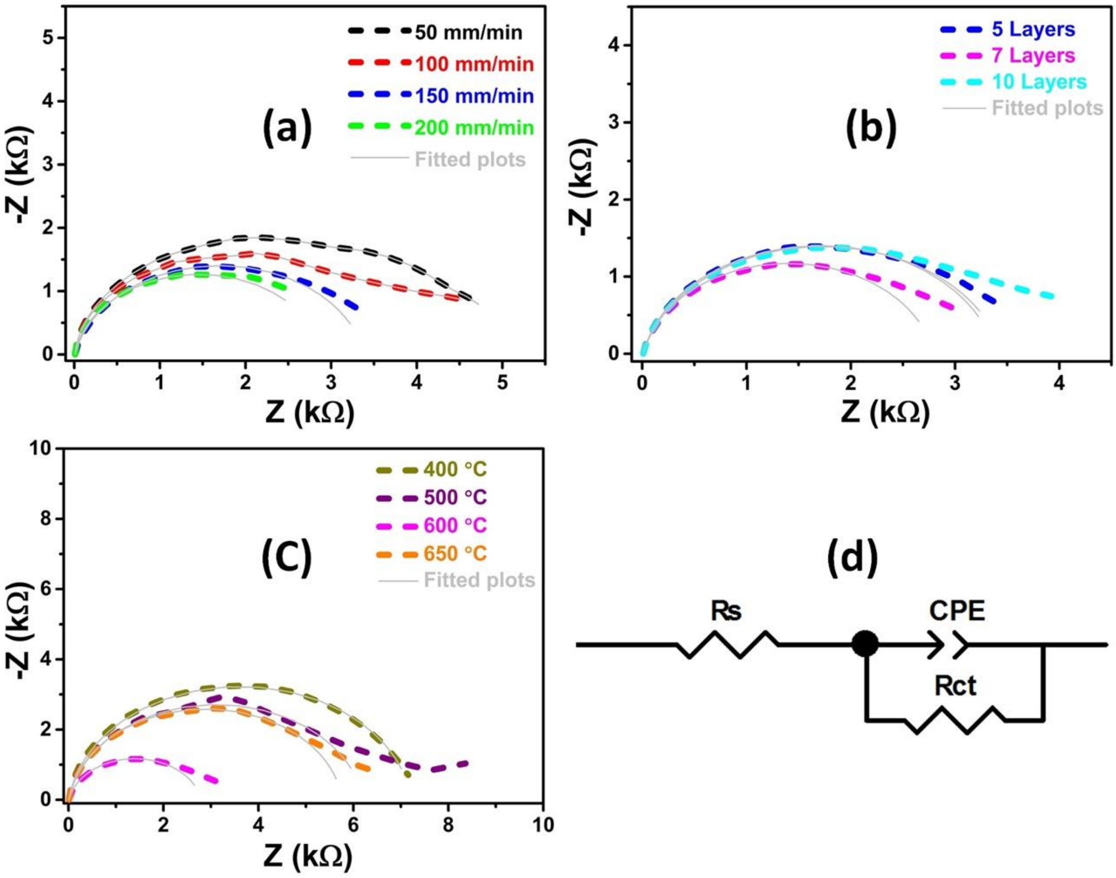

Figure 4.2.14 EIS of CuO photocathodes **(a)** withdrawn at different withdrawal speeds **(b)** consisting of different number of film layers, and **(c)** annealed at different temperature.

Upon fitting the modelled circuit to the raw EIS measurements, estimated values were obtained for the different elements and given in Table 4.2.2. The results show the least charge transfer resistance and an elevated value of double-layer capacitance for the films prepared at the withdrawal speed of 150 mm/min, deposited with 7 layers, and annealed at 600 ℃. These will ease the movement of electrons at the solid/liquid interface for hydrogen evolution which justifies the relatively large photo-current density obtained for the films. The largest resistance to charge transfer was recorded by films annealed at 400 °C, leading to the small photo-current exhibited by the films (Figure **4.2.*13***). Generally, the reduction of R_{ct} values largely corresponds with an increase in the photo-current response achieved in the LSV results which are like other reported observations [1, 34, 35].

Table 4.2.2 The values obtained for the different elements after fitting the EIS data to the circuit model using ZView software.

Processing parameter	Sample	Rs (Ω)	Rct kΩ	CPE (µF)
Withdrawal rates	**50 mm/min**	8.39	4.42	35.4
	100 mm/min	9.16	3.74	40.4
	150 mm/min	9.25	3.38	70.1
	200 mm/min	9.02	2.89	36.1
Film layers **(150 mm/min)**	**5L**	9.25	3.38	70.1
	7L	9.71	2.79	89.3
	10L	9.68	3.45	79.3
Annealing temperature **(7 Layers)**	**400°C**	10.84	7.21	0.5
	500°C	10.00	6.20	38.6
	600°C	9.71	2.79	89.3
	650°C	10.33	5.76	0.5

The stability of the pristine CuO thin film consisting of 7 layers and annealed at 600 ℃, which yielded the highest photo-current density was studied using chronoamperometry measurements at -0.4 V vs Ag/AgCl (i.e., 0.6 V vs RHE) for a time scan of 500 s in the presence of a 1 M NaOH electrolyte. Figure **4.2.*15*** shows that the CuO films lost about 23.8 and 71.64 % of their photo-current density after 100 and 500 s respectively. This was due to the photo-corrosion caused by the self-reduction of CuO by photoexcited electrons because of the position of the thermodynamic reduction potential which is below that of water [36-38]. This means that some of the photo-current observed for the CuO films (Figure **4.2.*13***) was not entirely due to the reduction of H^+ to hydrogen and the Faraday efficiencies of the photocatalytic reactions are expected to be way below 100%. For instance, Cots *et al.*, 2018 achieved Faraday efficiency of 45% for CuO films during photocatalysis because of their poor photo-stability [39]. Photo-corrosion is a limiting factor for the effective use of CuO as photocathodes for water reduction [36, 40]. This could be improved through doping of metal/non-metal ions [41], hetero coupling [1], defect engineering [42], as well as the incorporation of passivation layers [43], plasmonic metals [44], co-catalysts [45], nanoparticles [46] and quantum dots [47] on the surface of the films, respectively.

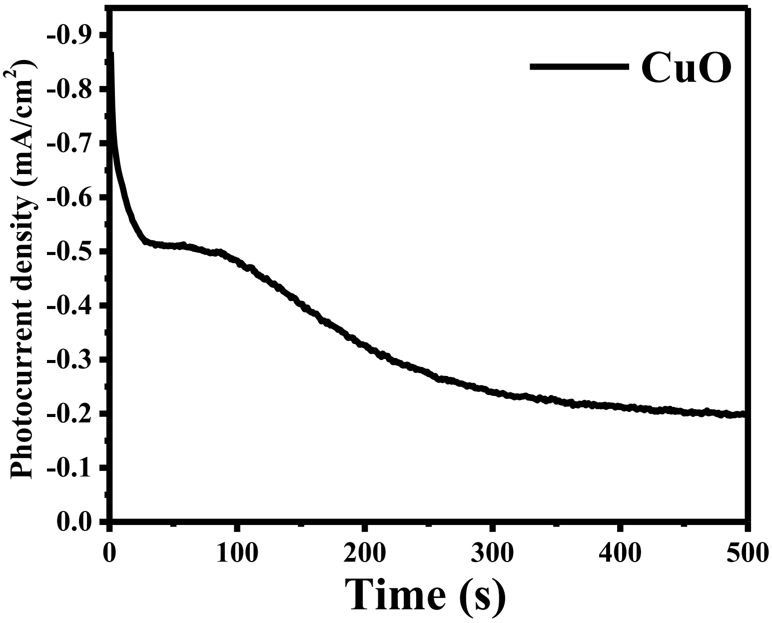

Figure 4.2.15 Photo-stability measurements performed at 0.6 vs RHE on the CuO thin films prepared at the withdrawal rate of 150 mm/min, deposited with 7 layers, and annealed at 600 °C.

4.3. CuO thin films decorated with protective layers of Activated Charcoal (AC) for PEC water-splitting

Here, the results obtained from the morphological, structural, optical and PEC studies of the pristine CuO films and the ones modified with 1, 3, and 5 layers of AC are discussed in detail. The protective layers of AC were deposited on CuO to help improve its photo-stability in electrolyte. These results are presented in sections 4.3.1 to 4.3.5.

4.3.1 Structural properties

The structural properties of CuO thin films consisting of 1, 3, 5 layers of AC were investigated using X-ray diffraction (XRD) spectroscopy within a 2 theta range of 20 - 80°, the results are shown in Figure **4.3.*1***. The XRD patterns show diffraction peaks at ($\bar{1}11$) and (111) planes, confirming the monoclinic crystal structure of the CuO films with lattice parameters a = 4.64 Å, b = 3.4 Å, c = 5.09 Å, β = 99.5° according to JCPDS no. 05–0661 [1, 2]. Other weak reflections corresponding to CuO are also observed at (020) and ($\bar{1}13$). No peak shifts or Bragg reflections for secondary phases of copper oxide are indicated. Also, diffraction peaks corresponding to AC are not visible on the XRD plots due to the low intensity of the peaks compared to those of CuO and FTO. Similar observations in which peaks of carbon were detected on the XRD patterns of CuO/carbon films have been reported [48, 49]. The intensity of diffraction peaks at ($\bar{1}11$) and (111) planes for the films consisting of 5 layers of AC significantly decreased due to the high concentration of carbon which has a more amorphous structure compared to CuO [50].

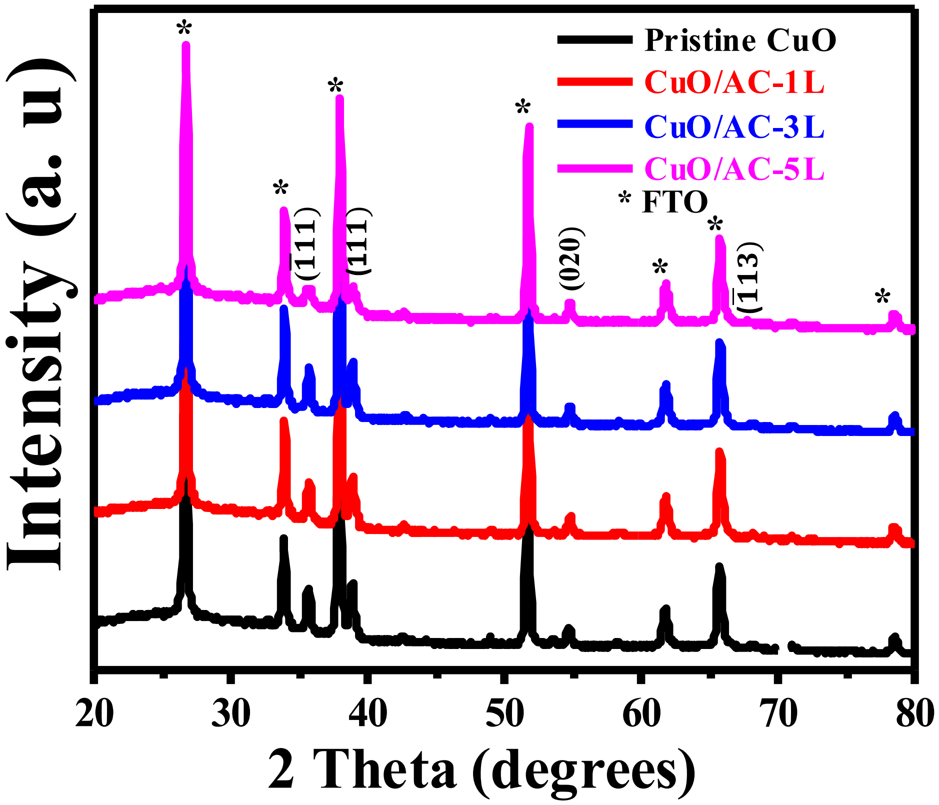

Figure 4.3.1 XRD patterns of pristine CuO, CuO/AC-1L, CuO/AC-3L and CuO/AC-5L thin films.

To further study the influence of AC on the crystallinity of CuO, the peaks at (111) plane were engaged to obtain the approximate crystal sizes of the prepared CuO/AC films using the Debye-Scherrer method. The average crystal sizes are presented in Table 4.3.1. The CuO/AC composite material which consist of 5 layers of AC was observed to greatly reduced the crystallinity of the CuO films due to high loading of carbon materials on the CuO films surface. The CuO/AC films which consist of 1 and 3 layers of AC did not show significant influence on the crystal sizes of the CuO films.

Table 4.3.1 XRD analysis showing FWHM and crystal size of pristine CuO and CuO thin films coated with 1, 3, 5 layers of AC.

Sample	2 theta	FWHM	Crystal size (nm)
Pristine CuO	36.08	0.38	19.89
1 Layer CuO/AC	35.71	0.36	21.02
3 Layers CuO/AC	35.7	0.35	21.62
5 Layers CuO/AC	35.68	0.6	12.61

Structural properties of CuO thin films consisting of 1, 3, 5 layers of AC were further investigated to confirm the presence of CuO and AC using Raman spectroscopy. The Raman spectrum of all the films (Figure **4.3.*2***) show an A_g phonon mode at 302 cm^{-1}, two B_g modes at 250 and 638 cm^{-1}, as well as a $2B_g$ mode at 1130 cm^{-1} which are ascribed to CuO. The $2B_g$ mode is reported to be a stretching vibration in the x^2-y^2 plane caused by the variation of electronic density between the two planes in the CuO structure [1, 10]. The CuO film with 5 layers AC shows two other prominent D and G modes at 1368 cm^{-1} and 1592 cm^{-1} which belong to AC. Also, the intensity of the modes ascribed to CuO have drastically decreased due to the drop in the crystallinity of the films resulting from the high amount of AC deposited on the surface of CuO films [48]. The Raman spectra of CuO/AC-1L and CuO/AC-3L films did not reveal the D and G modes due to the low concentration of carbon on the films which may be below the detection limit of the Raman equipment used for the measurements.

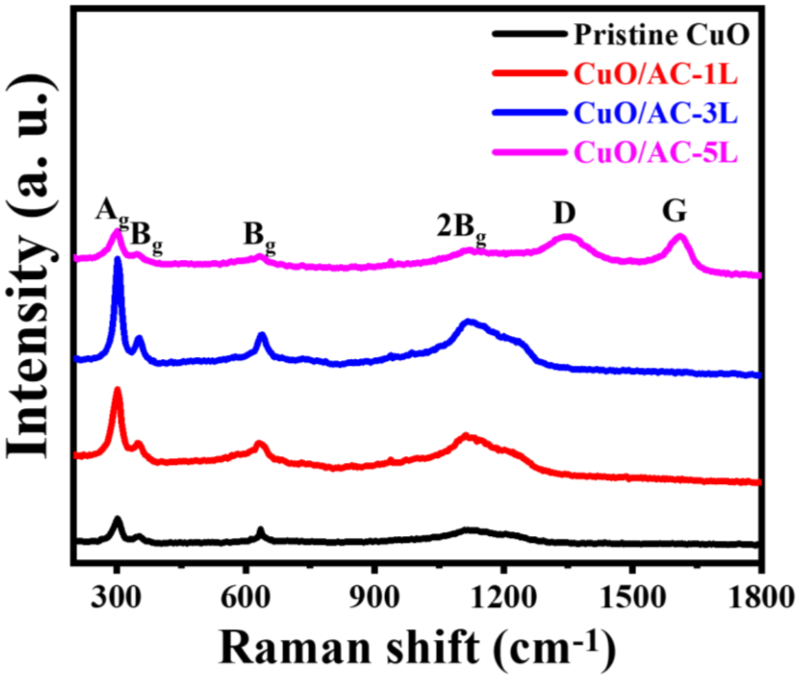

Figure 4.3.2 Raman spectra of pristine CuO and CuO/AC thin films deposited with 1, 3, 5 layers of AC.

4.3.2 Surface morphology and film thickness

The surface morphology of CuO thin films consisting of 1, 3, 5 Layers of AC were characterized using FE-SEM, as shown in Figure **4.3.*3*** (a), (b), and (c). Morphology of the CuO/AC-1L thin film revealed homogeneously distributed CuO spherical nanoparticles throughout the substrate. The AC on the CuO was not clearly distinguishable owing to the small amount of the deposited charcoal on the films surface. The CuO/AC-3L films shows some slight deposits of AC on the CuO film's surface. whereas the CuO/AC-5L samples disclosed significant deposits of AC on the CuO film's surface. A significant loading of the AC on the CuO is necessary to serve as a protective layer to the CuO films during PEC water-splitting.

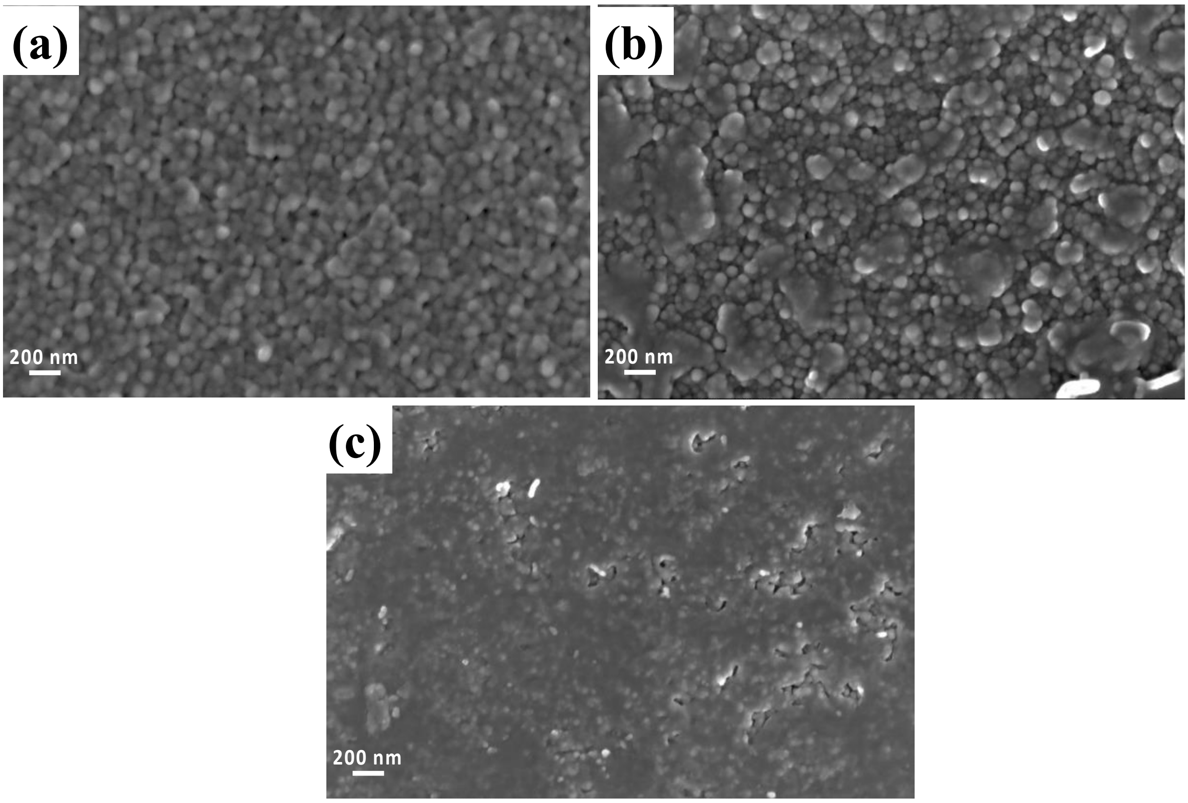

Figure 4.3.3 FE-SEM images of **(a)** CuO/AC-1L **(b)** CuO/AC-3L **(c)** CuO/AC-5L thin films.

The FE-SEM was further used to study the cross-sectional views of CuO films loaded with AC. Cross-sectional views of the films coated with 1, 3, 5 layers of AC are presented in Figure ***4.3.4*** (a), (b) and (c) respectively. Morphology of CuO/AC-1L did not exhibit any layer of AC due to the small deposition of the charcoal; hence, it's film thickness could not be estimated. However, the average film thickness for CuO/AC-3L and CuO/AC-5L was estimated to be 13.28 and 25.02 nm respectively.

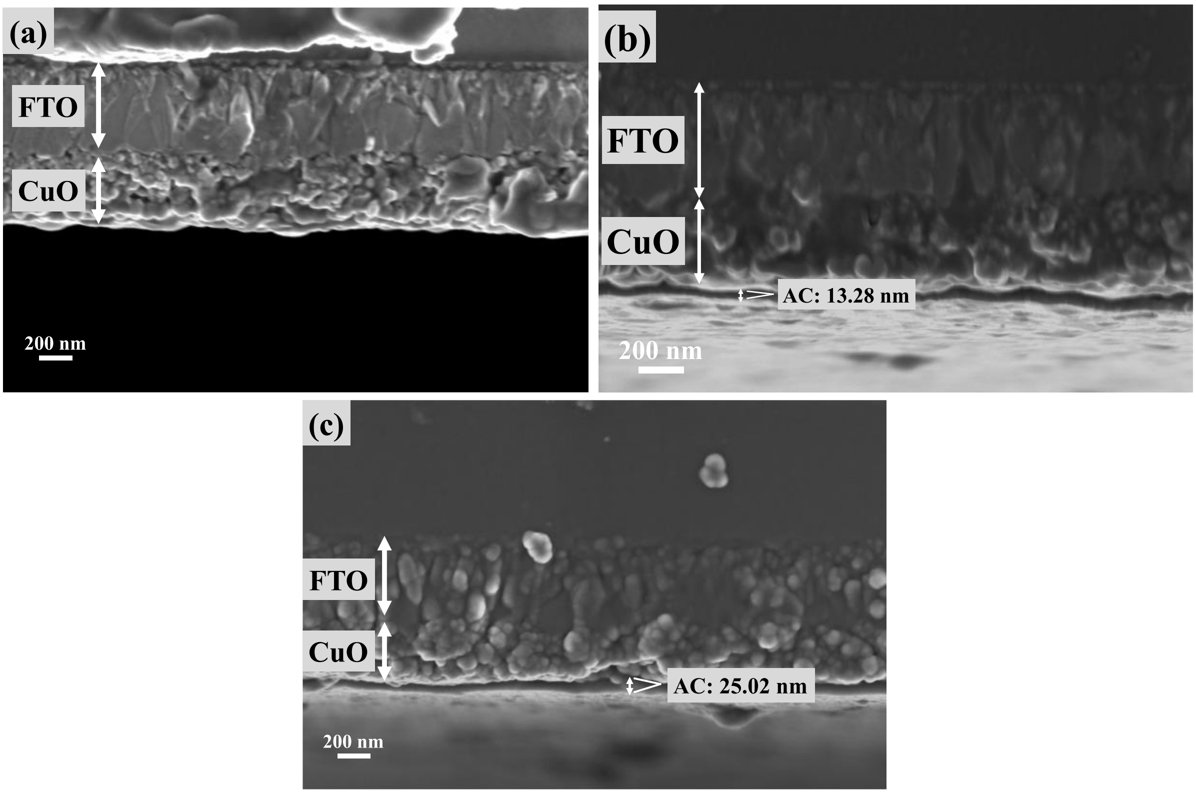

Figure 4.3.4 FE-SEM cross-sectional images of **(a)** CuO/AC-1L **(b)** CuO/AC-3L **(c)** CuO/AC-5L thin films.

4.3.3 Elemental composition

Energy Dispersive X-ray Spectroscopy (EDS) was used to verify the absence of impurities and to confirm the elemental composition of the films. The EDS analysis of CuO/AC-1L, CuO/AC-3L, and CuO/AC-5L are given in Figure 4.3.5 (a), (b) and (c) respectively. The presence of oxygen (O) and copper (Cu) was confirmed for all the films since they are the constituent elements of CuO. Carbon (C) was also confirmed for CuO thin films consisting of 1, 3, 5 layers of AC, since AC is a less dense and microcrystalline form of carbon [51].

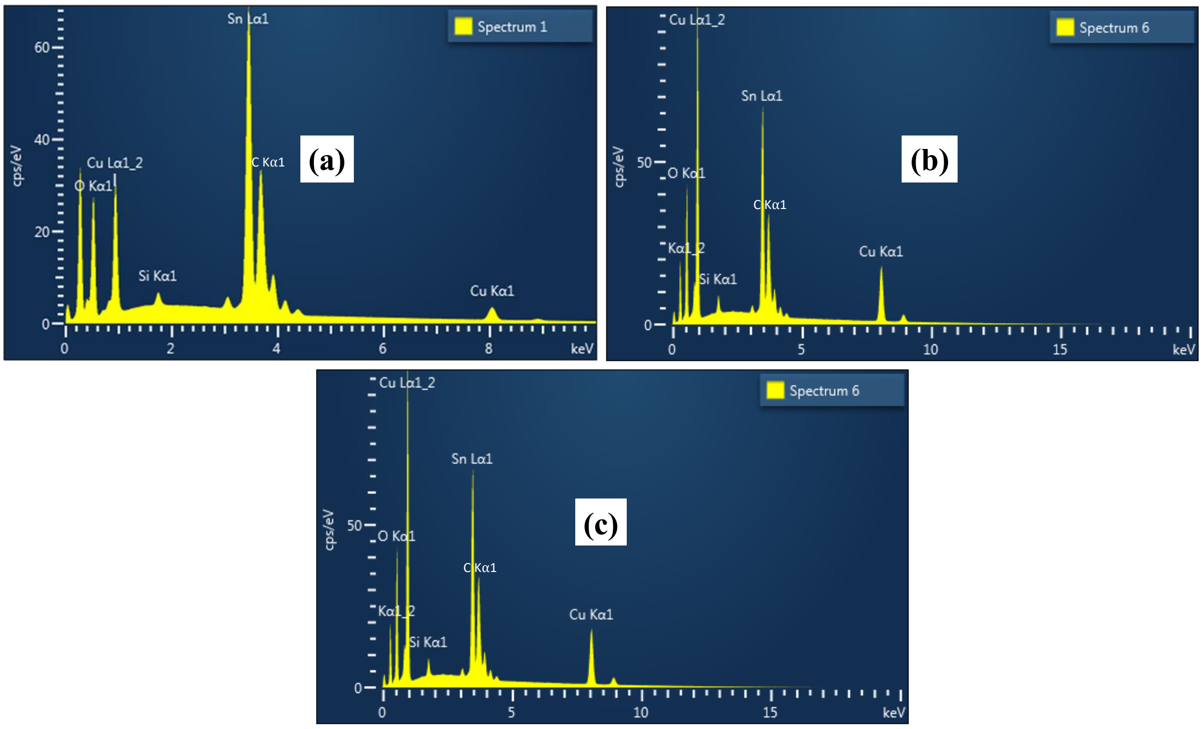

Figure 4.3.5 EDS spectrum of **(a)** CuO/AC-1L **(b)** CuO/AC-3L **(c)** CuO/AC-5L thin films, respectively.

4.3.4 Optical properties

UV-Vis spectroscopy was done to investigate the optical absorption and transmittance of the thin films. The obtained absorption was further utilized to determine the indirect bandgap of the films. Figure **4.3.*6*** shows the optical absorption of the pristine CuO films, and the ones modified with 1, 3, and 5 layers of AC. All films show photo-absorption in the visible region, with a slight absorption in the near-infrared region. CuO/AC-1L and CuO/AC-3L films exhibit similar photoabsorbance compared to pristine CuO, thus there is no improvement in the photoabsorbance of those films, this might be due to the small and moderate amount of AC decorated on CuO/AC-1L and CuO/AC-3L films, respectively. The film coated with 5 layers of AC showed the least photoabsorbance and its wavelength is observed to have narrowed to shorter wavelengths, these may indicate the presence of surface defects resulting from the large amount of AC coated on the CuO film. The enhanced light absorption observed for CuO/AC-1L and CuO/AC-3L over CuO/AC-5L films can help in promoting their photo-current response during water-splitting as earlier explained in section 4.2.4. The optical transmittance of the films is presented in the inset of Figure **4.3.*6***. All films are observed to be transmitting light in the near-infrared region of the electromagnetic region of the spectrum. The transmittance of films coated with AC are observed to be in line with their photo-absorbance behaviour in the visible region.

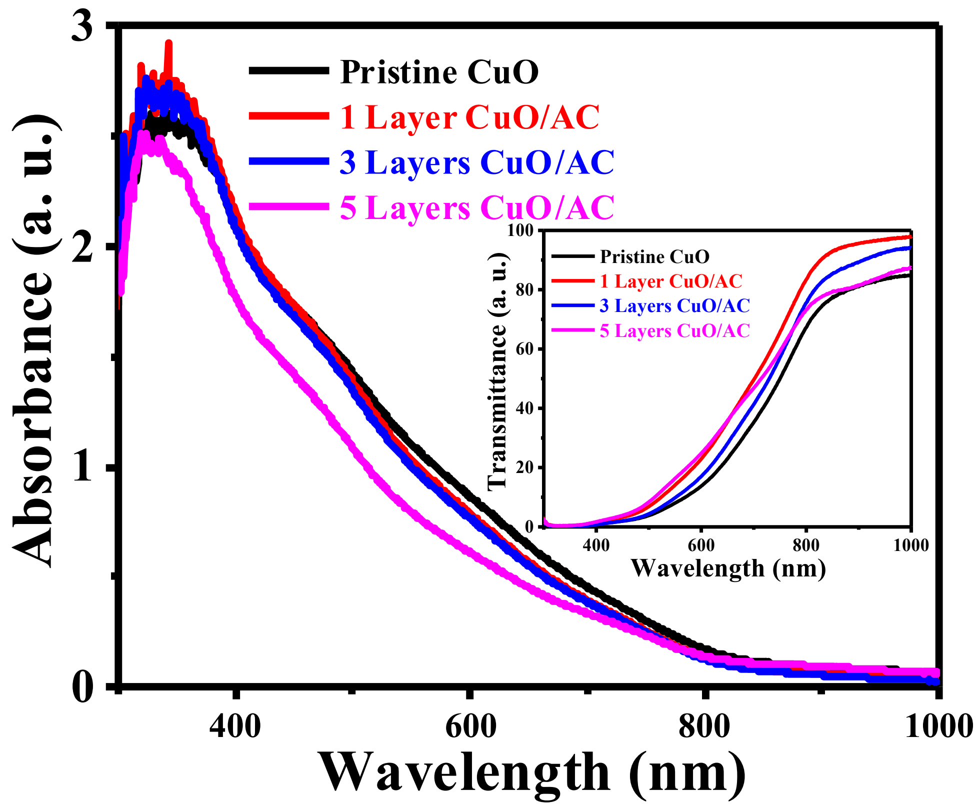

Figure 4.3.6 UV–Vis spectra of Pristine and CuO thin films coated with 1, 3, 5 layers of AC.

The Tauc plots for the indirect transitions of the pristine CuO thin films and the ones coated with 1, 3, 5 layers of AC are presented in Figure **4.3.7**. The plots were used to approximate the optical bandgap (Eg) values using the Tauc relation given in Eq. 4.2.2. The indirect bandgap was estimated to be 1.25±0.04 eV for all AC-incorporated CuO films, whereas for pristine CuO it was estimated to be approximately 1.34 eV (section 4.2.4), respectively.

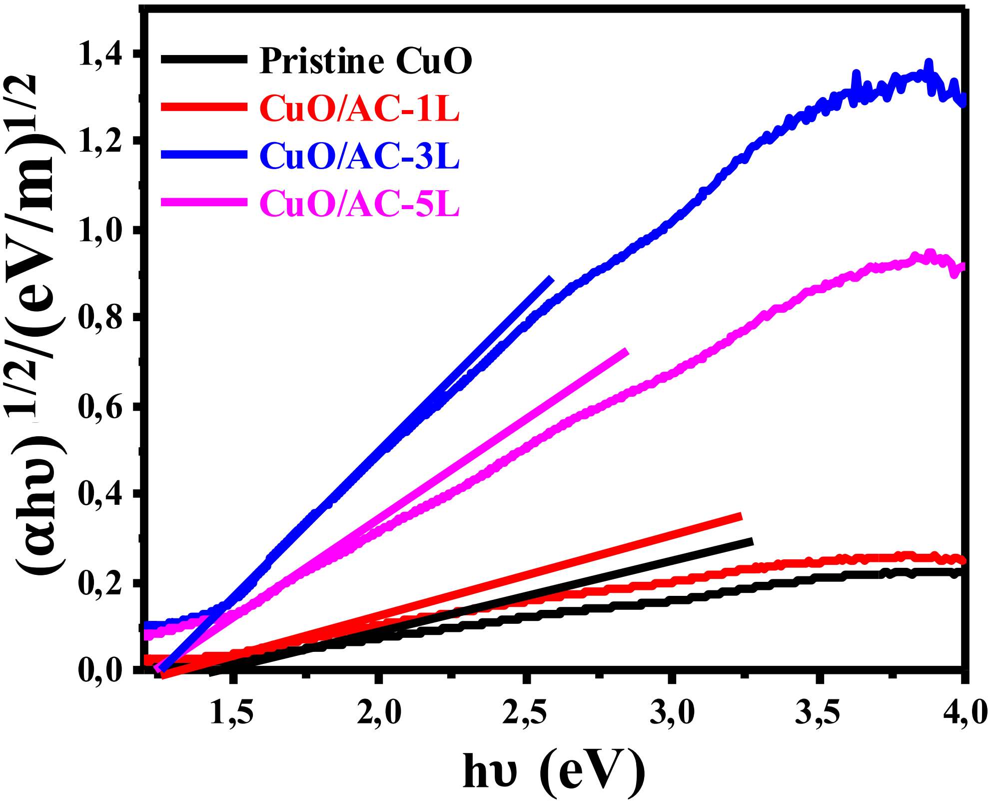

Figure 4.3.7 The Tauc approximation for the indirect bandgaps of pristine CuO, CuO/AC-1L, CuO/AC-3L and CuO/AC-5L thin films.

4.3.5 Photoelectrochemical properties

LSV measurements were performed under illumination conditions to obtain the photo-current response of the pristine CuO and CuO/AC photocathodes coated with 1, 3, 5 layers, as shown in Figure **4.3.*8***. The maximum photo-current density of 1.5 mA/cm^2 at 0.5 V vs RHE was produced by the CuO/AC-1L photocathode, whereas pristine CuO produced 1.2 mA/cm^2 at the same potential. The enhanced photo-current response of CuO/AC-1L is attributed to the low coverage of AC over the film [52, 53]**,** suggesting an improvement in the electric charge on the surface of the film, as well as in the separation and transport of the photo-generated charges [52, 54]. On the contrary, CuO/AC-5L produced the least photo-current response. The overloading of AC may have resulted in the formation of defects on the surface of the CuO films which may serve as centers for the accumulation of photo-generated electrons.[52]. This will stimulate electron/hole recombination, preventing the generation of photo-current [50].

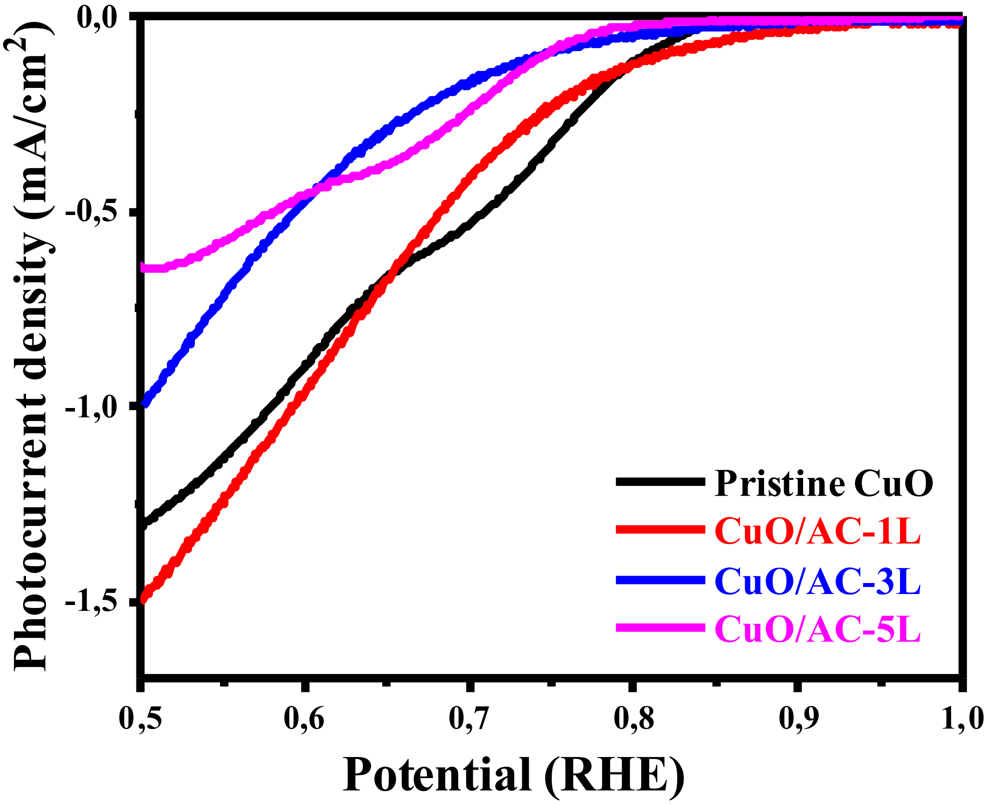

Figure 4.3.8 Current density measurements done under illumination conditions for pristine and CuO/AC photocathodes.

EIS measurements were also performed on pristine CuO and CuO photocathodes coated with 1, 3, 5 layers of AC, to analyse charge transfer processes occurring at the solid/liquid interface. Figure **4.3.9** shows the Nyquist plot of the EIS experimental and fitted data for the prepared photocathodes. The simple Randles circuit given in Figure **4.2.*14*** (d) was also used to fit the EIS experimental data obtained for the CuO/AC films. The circuit elements Rs, Rct and CPE also denote the same physical properties as explained in section 4.2.5. As earlier stated, Rs represents the total series resistance caused by the FTO, electrolyte, and connecting wires. CPE denotes the capacitance of the electric double-layer and Rct refers to the charge transfer resistance at the solid/liquid interface.

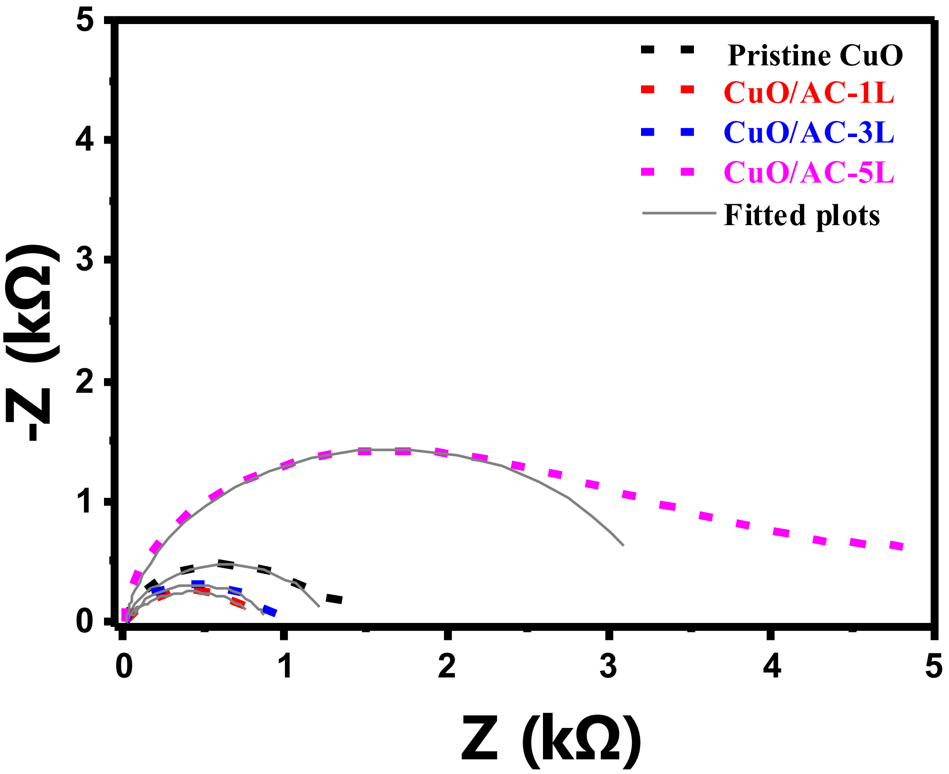

Figure 4.3.9 Electrochemical Impedance Spectra (EIS) of pristine CuO, CuO/AC-1L, CuO/AC-3L and CuO/AC-5L photocathodes.

Table 4.3.2 The values obtained for the different elements after fitting the EIS data to the circuit model using ZView software.

Sample	**Rs (Ω)**	**Rct (kΩ)**	**CPE (µF)**
Pristine CuO	9.29	1.24	128.8
CuO/AC-1L	9.56	0.82	306.4
CuO/AC-3L	8.52	0.89	150.8
CuO/AC-5L	10.24	3.29	99.00

The values estimated for the different elements of the circuit model after fitting to the raw EIS measurements are given in Table 4.3.2. The CuO/AC-1L photocathode exhibits the least charge resistance (R_{ct}) and the highest value of the double-layer capacitance (CPE). These results correlate with the photo-current response of the photocathodes in Figure **4.3.*8***, where CuO/AC-1L yielded the highest photo-current response compared to the other CuO films modified with AC. CuO/AC-5L produced the highest Rct values for the AC modified films which resulted in the low photo-current density obtained for the films as seen in Figure **4.3.*8***. The overloading of AC on the surface of the CuO films may have limited the movement of charge carriers to the surface of the films resulting in the high Rct value obtained for the films.

Mott-Schottky measurements were performed to obtain the charge carrier concentration (N_A) and flat-band potentials (V_{fb}) of pristine CuO, as well as CuO/AC-1L, CuO/AC-3L and CuO/AC-5L photocathodes respectively. The MS plots of all films are presented in Figure **4.3.*10***, and they exhibit a negative slope, indicating their p-type nature and validating the cathodic photo-current response observed in Figure **4.3.*8*** [15]. The values for the flat-band potentials and charge carrier concentrations were obtained from the MS relation equation earlier given in chapter 3 (Eq. 3.4). The estimated values of V_{FB} and N_A extracted from MS plots are given in Table 4.3.3. The flat-band potential for the pristine CuO was estimated to be 1.049 V vs RHE, however this value shifted to 1.135 ± 0.048 V vs RHE for the AC modified films. The positive shift may be attributed to the achieved equilibrium between the fermi levels of CuO and AC, when CuO/AC was formed. The maximum charge carrier density was observed for the CuO/AC-1L photocathode with an approximate value of 10.28 x 10^{20} cm^{-3}. The increased charge concentration indicates an improvement in the conductivity of the films and justifies the enhanced photo-current response observed in Figure **4.3.*8*** [15, 48].

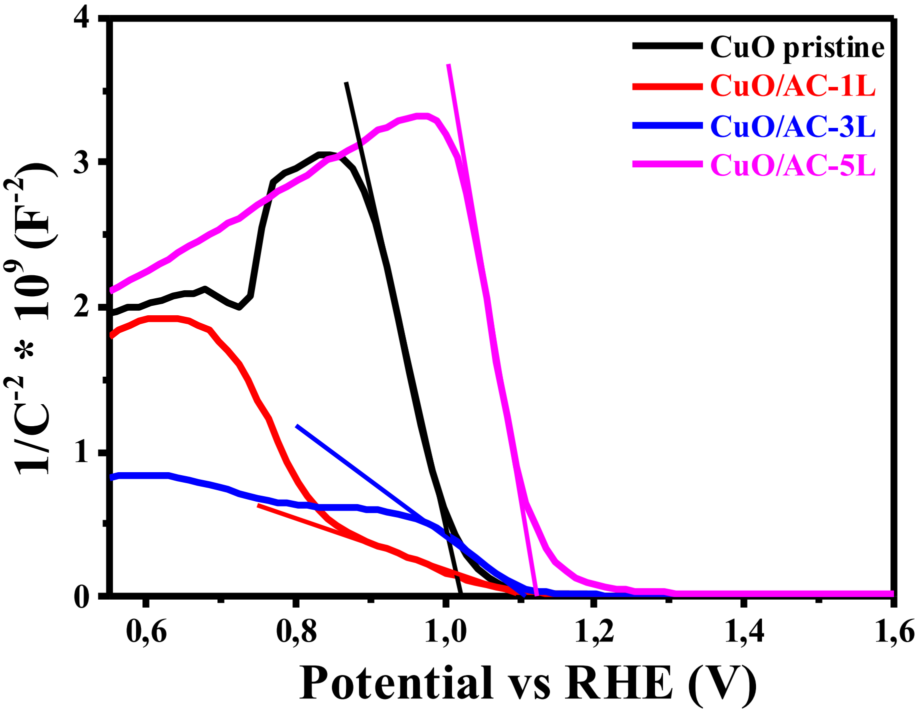

Figure 4.3.10 MS plots of pristine CuO films and the ones consisting of 1, 3, 5 layers of AC.

Table 4.3.3 Table showing V_{fb} and N_d estimated from the MS plots of pristine CuO films and the ones coated with 1, 3, and 5 layers of AC.

Sample	**V_{fb} vs RHE (V)**	**$N_D * 10^{20}$ (cm^{-3})**
CuO Pristine	1.049	0.9
CuO /AC-1L	1.115	10.28
CuO/AC-3L	1.137	5.31
CuO/AC-5L	1.154	0.73

Chronoamperometry measurements were performed to study the stability of CuO photocathodes coated with 1, 3, and 5 layers of AC over-time. Figure **4.3.*11*** shows the photo-current density of CuO/AC-1L, CuO/AC-3L and CuO/AC-5L photocathodes at a constant potential of 0.6 V vs RHE, over a period of 0 - 500 s. CuO/AC-1L and CuO/AC-3L films did not improve the stability of CuO in the electrolyte used, retaining 47.2 % and 41.5 % of their photo-current densities after 200 s, respectively. The poor stability exhibited by the films indicate that a large part of the photo-current observed for the films may be due to photo-corrosion, and not entirely from hydrogen evolution reaction [39]. However, the photo-stability of CuO/AC-5L showed a significant improvement in electrolyte, retaining 45.5 % of its photo-current after 500 s as compared to the 28.4 % sustained by the pristine CuO samples after the same period. Thus, the photo-stability exhibited by CuO/AC-5L at 500 s is 17.1 % larger than the pristine photocathodes (Figure **4.2.*15***). Although the CuO/AC-5L films showed improved stability, it produced the least photo-current (Figure **4.3.*8***), thus additional work needs to be done to simultaneously improve both the photo-current density and photo-stability of the AC modified films in aqueous electrolytes.

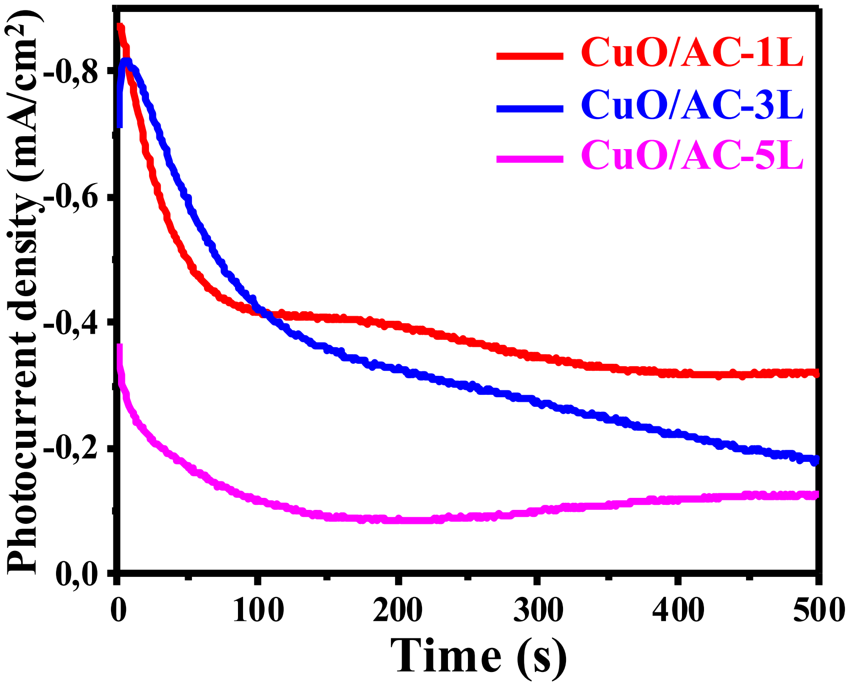

Figure 4.3.11 Photo-stability measurements performed at 0.6 V vs RHE on the CuO/AC-1L, CuO/AC-3L and CuO/AC-5L photocathodes.

4.4 CuO thin films modified with Ag nanoparticles for enhanced photo-stability during PEC reactions

In this section, the results obtained from the morphological, structural, optical and PEC studies of the pristine CuO films and the ones modified with 1, 3, and 5 layers of Ag nanoparticles (AgNPs) are discussed in detail. The protective layers of Ag were deposited on CuO films to improve their photo-stability in electrolyte. These results are presented in sections 4.4.1 to 4.4.5.

4.4.1 Structural properties

XRD measurements were done to analyse the structural properties of the pristine CuO thin films, and the ones modified with consisting of 1, 3, 5 layers of Ag NPs. Figure **4.4.*1*** shows XRD patterns of the films within a 2 theta range of 20 – 80°. The XRD patterns show diffraction peaks at ($\bar{1}$11) and (111) crystallographic planes, verifying the monoclinic crystal structure of the CuO films [1, 2]. Also, CuO thin films coated with 5 layers of Ag NPs showed diffraction peaks at (111), (200), (220), and (311) planes, revealing the face-centered cubic crystal structure of the Ag, with lattice parameters a = 4.0861 Å, according to JCPDS no 65-2871 [55, 56]. The Ag peak at the (111) plane cannot be clearly observed due to the overlap with the CuO peak, also at the (111) plane. Similar observations were reported by Sang *et. al*, 2019 when Ag NPs were loaded on a TiO_2 photoanode for efficient solar water-splitting [57]. Also, CuO films coated with 1 and 3 Layers of Ag NPs did not exhibit any Ag diffraction peaks owing to the small amount of Ag NPs deposited on the films.

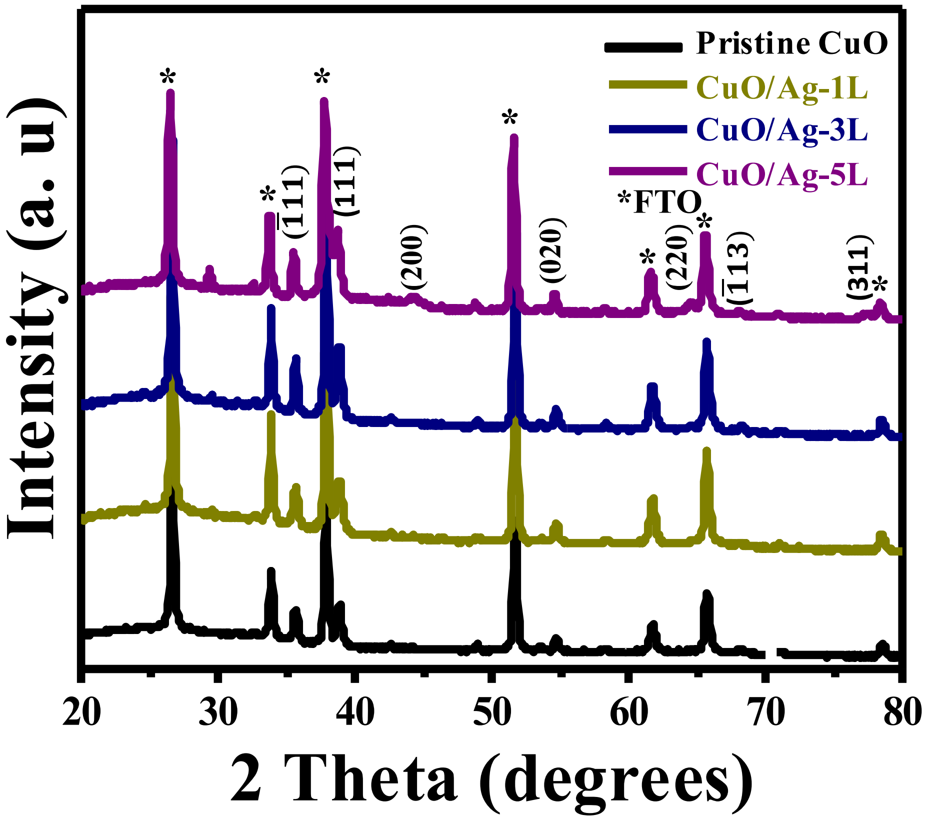

Figure 4.4.1 XRD patterns of a pristine CuO and CuO/Ag thin films.

To study the influence of Ag NPs on the crystallinity of the CuO thin films, the peaks at ($\bar{1}11$) were used to obtain the FWHM and crystal size values of the prepared films. The crystal sizes of the thin films were also estimated using the Debye-Scherrer method. The FWHM and estimated crystal sizes of the thin films are presented in Table 4.4.1. The average crystal sizes are observed to have increased slightly upon the deposition of Ag NPs, indicating a small improvement in the crystallization of CuO films.

Table 4.4.1 XRD analysis showing FWHMs and crystal sizes of a pristine CuO thin film and CuO thin films coated with 1, 3, and 5 layers of Ag NPs.

Sample	2 theta	FWHM	Crystal size (nm)
Pristine CuO	36.08	0.38	19.89
CuO/Ag-1L	35.66	0.33	22.93
CuO/Ag-3L	35.67	0.33	22.93
CuO/Ag-5L	35.54	0.34	22.26

To further study the structural properties of the films, the Raman spectra of the CuO samples were obtained to study the vibration of phonon modes of the films. Figure **4.4.*2*** shows the Raman spectra of pristine CuO films, and the ones coated with 1, 3, 5 layers of Ag NPs. The spectra revealed one A_g Raman active phonon mode at 302 cm^{-1} and two B_g phonon modes at 250 and 638 cm^{-1}, which are attributed to CuO [1, 11]. The spectra also show vibrational modes ascribed to Ag at 1292, 1364, and 1544 cm^{-1} for the film loaded with 3 layers of Ag NPs. Also, the film coated with 5 layers reveals an extra Ag phonon mode at 233 cm^{-1}. Furthermore, it is observed that the intensity of the Raman peaks ascribed to CuO drastically declined when the film was coated with 5 layers. This was due to the Raman active sites which have been covered by the high amount of Ag loaded onto the CuO films [58].

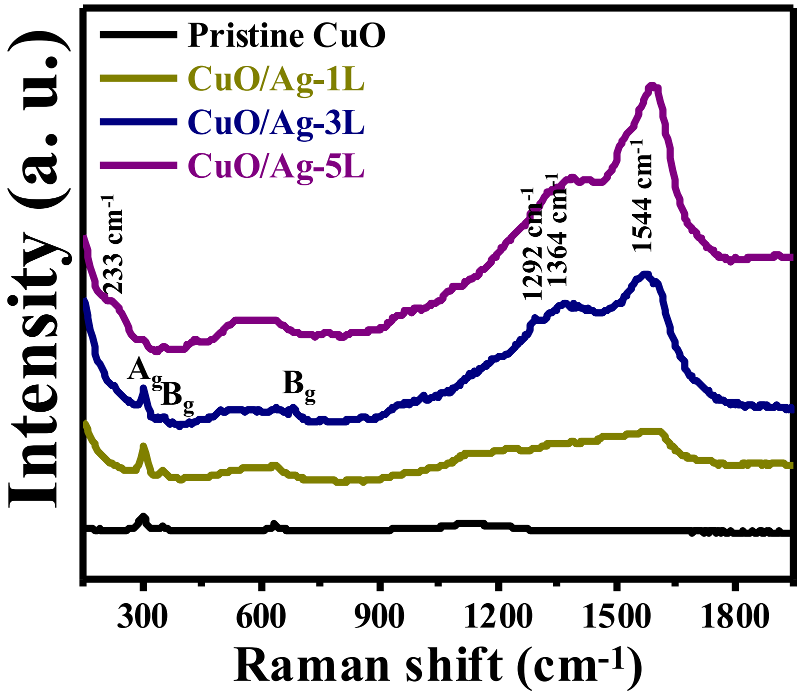

Figure 4.4.2 Raman spectra of pristine CuO and CuO/Ag thin films.

4.4.2. Surface morphology and film thickness

FE-SEM was utilized to investigate the influence of Ag NPs on the surface morphology of CuO thin films. Morphologies of CuO/Ag-1L and CuO/Ag-3L films are given in Figure 4.4.3 (a) and (b), respectively. The morphologies disclosed spherical CuO nanostructures which have been largely covered with Ag NPs. Lastly, the morphology of 5 layered-CuO/Ag films given in Figure 4.4.3 (c) shows the entire CuO films covered with AgNPs. The grain sizes of Ag NPs could not be estimated due to the high agglomeration of on the nanoparticles on the CuO films.

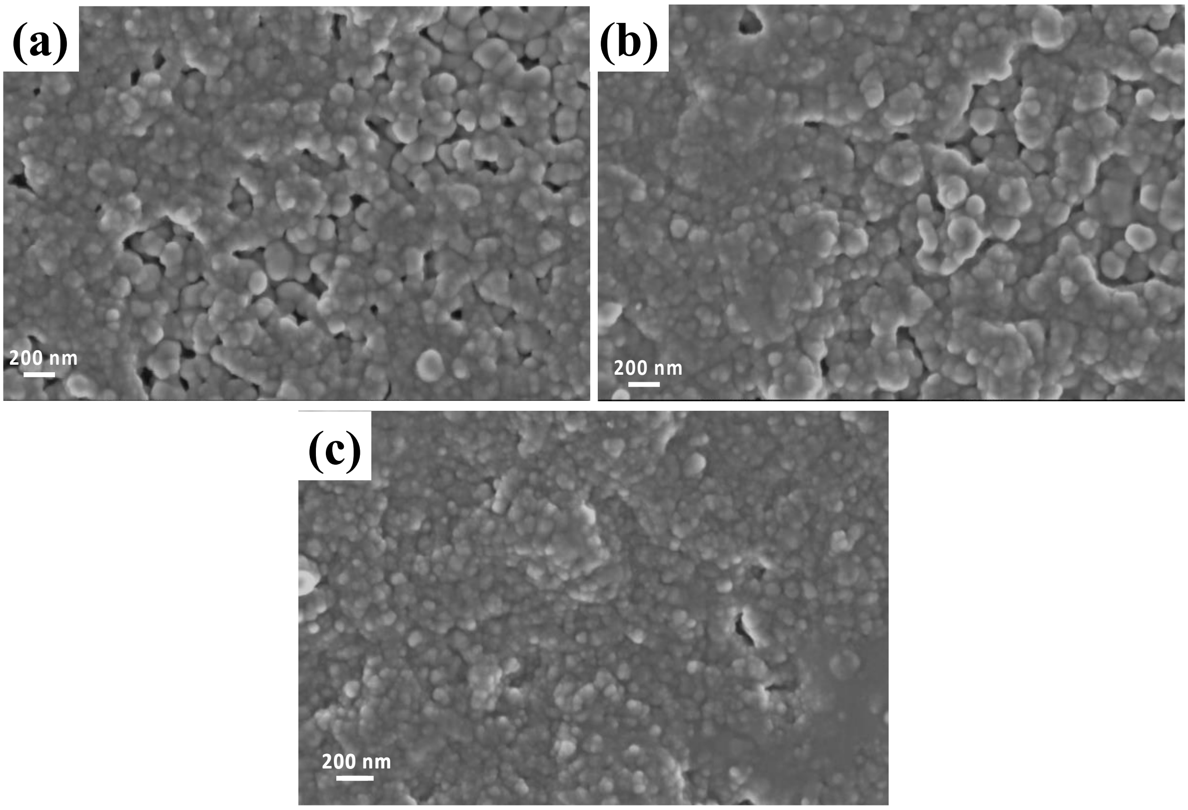

Figure 4.4.3 FE-SEM images of CuO thin films coated with (a) one (b) three (c) five layers of Ag NPs.

The FE-SEM was further used to study the cross-sectional views of the CuO films decorated with AC on the surface. Cross-sectional views of the films coated with 1, 3, 5 layers of AC are presented in Figure 4.4.4 (a), (b) and (c), respectively. The average film thickness of CuO/AC-1L, CuO/AC-3L and CuO/AC-5L was estimated to be 43.00, 55.18 and 111.41 nm respectively.

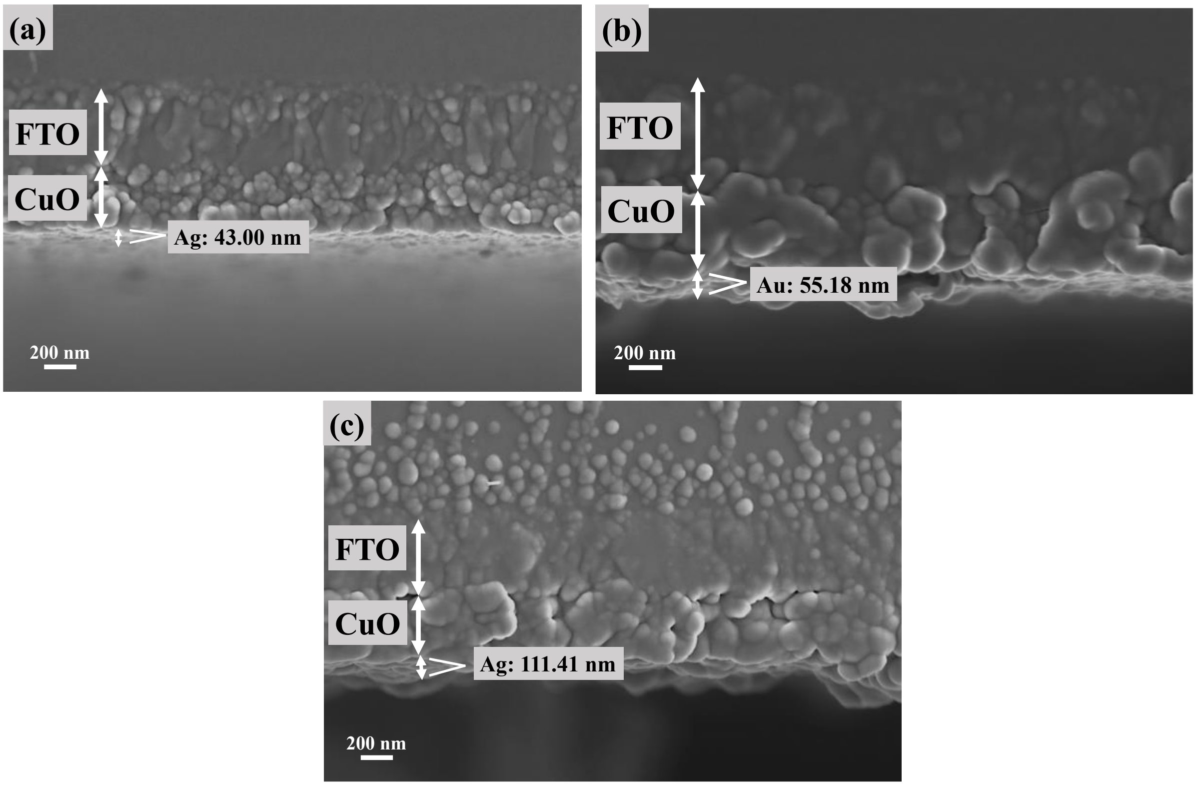

Figure 4.4.4 Cross-sectional images of **(a)** CuO/Ag-1L **(b)** CuO/Ag-3L and **(c)** CuO/Ag-5L thin films

4.4.3 Elemental composition

EDS was also used to verify the absence of impurities and to confirm the elemental composition of the films. The EDS analysis of CuO/Ag-1L, CuO/Ag-3L and CuO/Ag-5L thin films are given in Figure 4.4.5 (a), (b), and (c). As mentioned in section 4.2.3, The presence of oxygen (O) and copper (Cu) was confirmed for all films, since they are constituent elements of CuO. The analysis also verifies the presence of Ag on the CuO thin films consisting of 1, 3, 5 layers of Ag NPs, respectively.

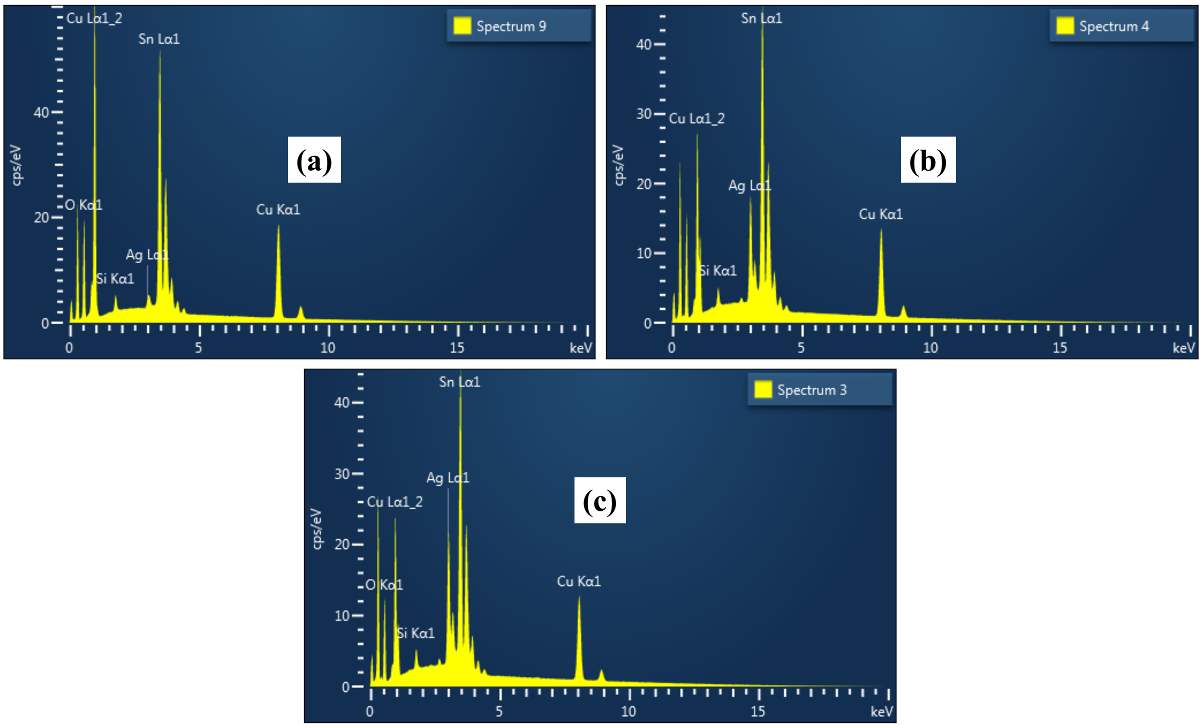

Figure 4.4.5 EDS spectrum of **(a)** a pristine CuO, and CuO thin films coated with **(b)** one **(c)** three **(d)** five layers of Ag NPs.

4.4.4 Optical properties

UV-Vis spectroscopy was done to investigate the optical absorption and transmittance of the CuO/Ag thin films. The absorption pattern was further used to determine the indirect bandgap of the films. Figure 4.4.6 exhibits the optical absorption and transmittance of the pristine CuO films and the ones consisting of 1, 3, 5 layers of Au. All films exhibit photo-absorption in the visible region, with a slight absorption in the near-infrared region. The photo-absorbance of the CuO films was observed to increase with the addition of Ag NPs, whereas pristine films show the least photoabsorbance. The observed enhancement was as a result of the localized plasmonic effect on the surface of the films generated by the interaction of photons with Ag-decorated films [59]. Furthermore, the absorption band of the films was broadened to longer wavelengths with increasing number of Ag NPs layers. The broadening effect is attributed to the enhancement in photo-absorption resulting from the surface plasmon resonance induced by the addition of Ag NPs [60].

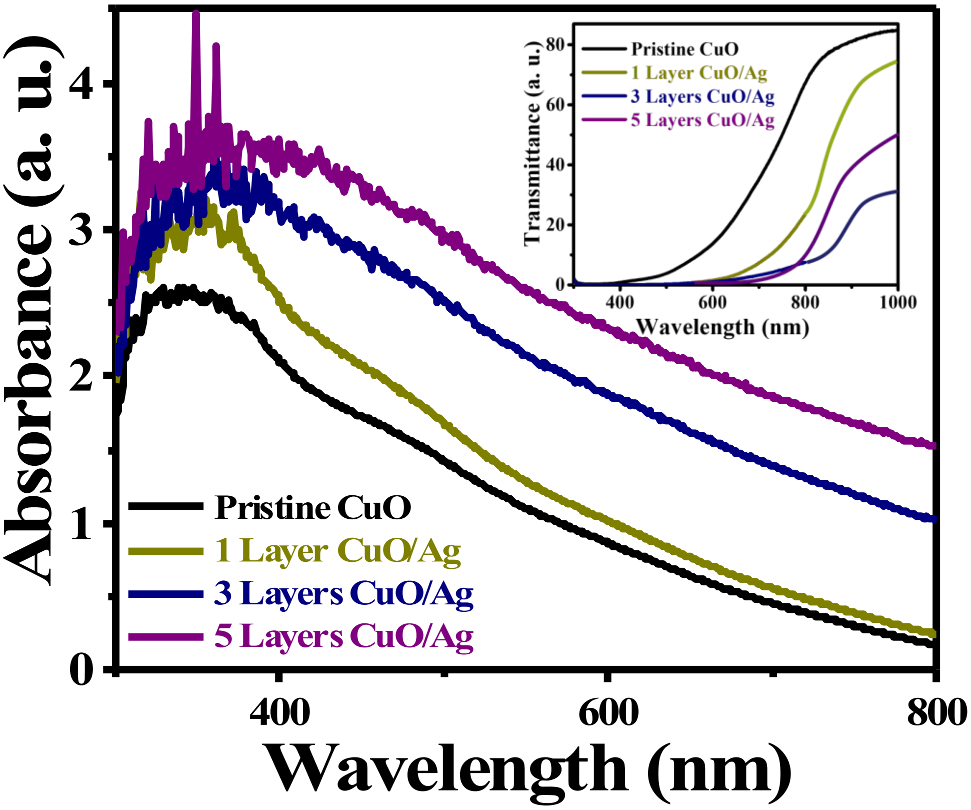

Figure 4.4.6 UV–Vis spectra of pristine and CuO thin films coated with 1, 3, 5 layers of Ag.

The Tauc plots for the indirect transitions of the CuO thin films coated with 1, 3, 5 layers of Ag are presented in Figure **4.4.7**. The plots were also used to approximate the optical bandgap values of the films using the Tauc relation given in Eq. 4.2.2. The indirect bandgaps of CuO/Ag-3L and CuO/Ag-5L films were estimated to be 0.83 ± 0.02 eV, whereas for CuO/Ag-1L it was estimated to be 1.20 eV. Furthermore, all estimated bandgaps for CuO/Ag films are significantly narrow with respect to the 1.34 ± 0.04 estimated for the pristine films (section 4.2.4). The observed decline in the estimated bandgaps is a result of the downward and upward shift of the conduction and valence band caused by free electrons produced by the over-loading of Ag NPs on the surface of the CuO samples [60].

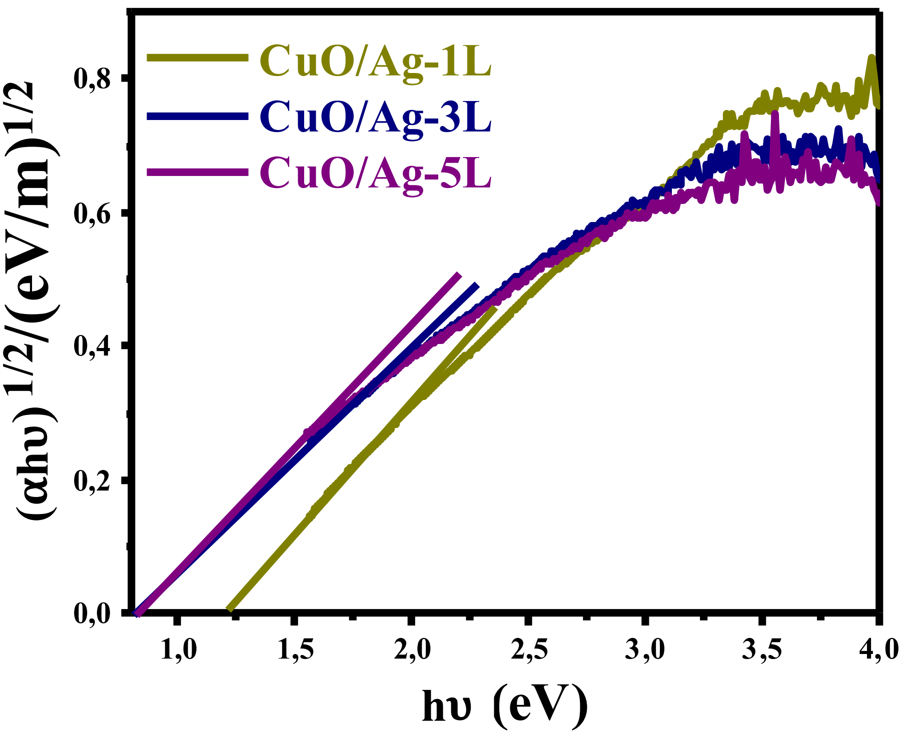

Figure 4.4.7 The Tauc approximation for indirect bandgaps of CuO/Ag-1L, CuO/Ag-3L and CuO/Ag-5L thin films.

4.4.5 Photoelectrochemical properties

LSV measurements were performed under dark and illumination conditions to obtain the photo-current response of CuO photocathodes coated with 1, 3, 5 layers of Ag NPs (Figure **4.4.***8*) and compared them with that of the pristine films. The highest photo-current of 2.9 mA/cm^2 at 0.35 V vs RHE was produced by the pristine CuO. The high photo-current response for the pristine CuO was partly due to photo-corrosion and not solely attributed to water reduction [39]. Plasmonic nanoparticles (Ag or Au NPs) are essential for preventing photo-corrosion of photoelectrodes in the presence of liquid electrolytes. Hence, the photo-response of the pristine CuO dropped upon the deposition of Ag, owing to the lost in the photo-current density which was as a result of photo-corrosion [61]. The CuO film coated with 5 layers of Ag NPs exhibits a strong cathodic peak at 0.58 V vs RHE associated with the reduction of Ag [62, 63]. Mikhlin *et.al, 2014* reported this cathodic behaviour for large citrate-capped Ag nanoparticles [64]. The reduction peak was largely influenced by the large amount of citrate-capped Ag NPs deposited on the surface of the CuO film.

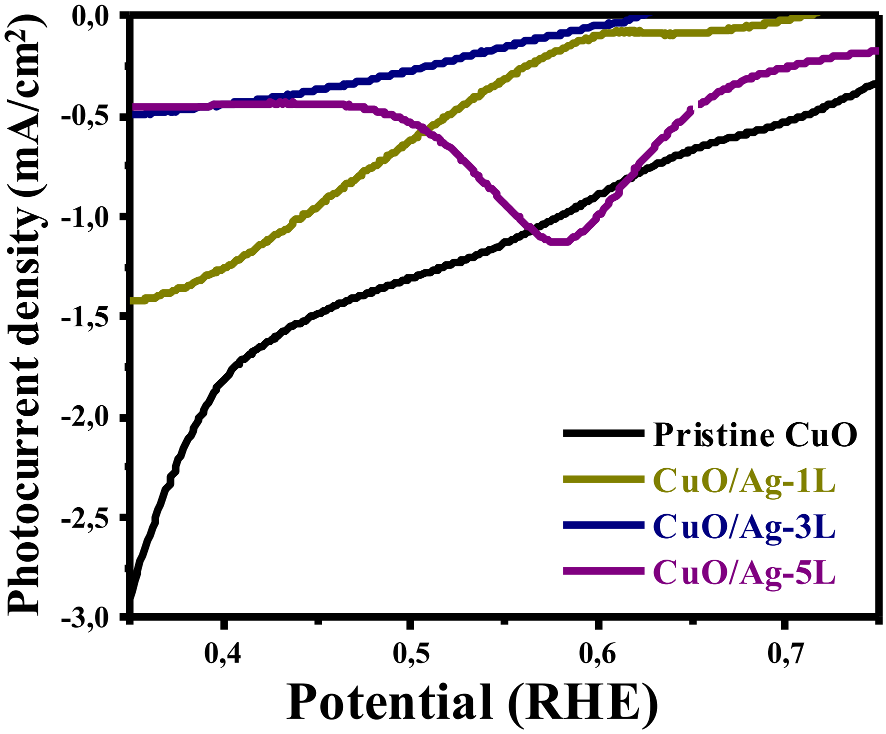

Figure 4.4.8 photo-current densities pristine CuO and CuO/Ag photocathodes.

Electrochemical Impedance Spectroscopy (EIS) measurements were performed to analyse the charge transfer processes occurring at the solid/liquid interface of the pristine CuO photocathodes and the ones coated with 1, 3, 5 layers of Au, respectively. The Nyquist plot of the EIS experimental and fitted data for all photocathodes are given in Figure 4.4.9. The Randles circuit consisting of a resistor, Rs, in series with a parallel connection of CPE and Rct, given in Figure **4.2.*1*** (d), was also used to fit the EIS experimental data obtained for the CuO/Au films. The components of the Randles circuit represent the same physical processes as explained in section 4.2.5.

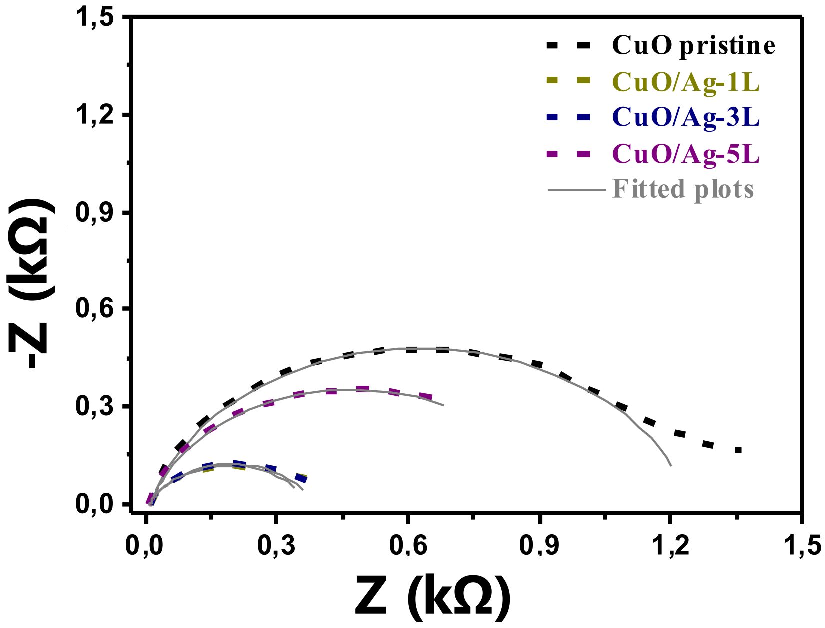

Figure 4.4.9 EIS Nyquist plots of pristine CuO, CuO/Ag-1L, CuO/Ag-3L, and CuO/Ag-5L photocathodes.

Table 4.4.2 The values obtained for the different elements after fitting the EIS data to the equivalent circuit model using ZView software.

Sample	**Rs (Ω)**	**Rct (kΩ)**	**CPE (µF)**
CuO pristine	9.29	1.24	128.8
CuO/Ag-1L	8.73	0.37	743.5
CuO/Ag-3L	6.51	0.38	601.0
CuO/Ag-5L	8.12	0.93	860.6

Table 4.4.2 shows the values estimated for the different elements of the circuit model after fitting it to the raw EIS measurements. The charge transfer resistance, Rct, value of CuO/Ag-1L and CuO/Ag-3L photocathodes were similar, differing by a small value of 0.01 kΩ. CuO/Ag-1L yeilded the lowest Rct value of 0.37 kΩ. The highest charge transfer resistance of 1.24 kΩ was observed for the pristine CuO films despite recording the maximum photo-current density (Figure **4.4.*8***). The high photo-current response obtained for the pristine films was partly due to the photo-corrosion occurring at the surface of the photocathode, as earlier explained. The Ag NPs deposited on the pristine CuO samples helped to ease the transfer of electrons across the solid/liquid interface owing to the localized plasmon effect occurring when

Ag interacts with CuO [65, 66]. Thus, all the Ag modified CuO films yielded lower Rct values compared to the pristine film.

To obtain the charge carrier concentration (N_A) and flat-band potential (V_{fb}) for the CuO/Ag photocathodes, Mott-Schottky measurements were performed on the films and the results are presented in Figure **4.4.*10***. The MS plot for the pristine CuO photocathode was earlier given in Figure **4.3.10**. The approximate values of V_{FB} and N_A were extracted from the MS plots in line with Eq. 3.4 and are given in Table 4.4.3. The maximum flat-band potential was yielded by pristine CuO at 1.049 V vs RHE. The values of flat-band potentials shifted to more negative potentials in the presence of Ag NPs with CuO/Ag-3L photocathodes having the least V_{fb} of 0.844 V vs RHE. Furthermore, a steep negative slope was not observed for the CuO/Ag-5L photocathode. Hence, a straight line could not be fitted to obtain the value of the flat-band potential. The non-cathodic behaviour may be caused by the photoelectrochemical reduction of Ag as observed in Figure **4.4.*8***. The flat-band potential depends on the level of band-bending of a photoelectrode. The higher the level of bending of bands, the thicker the depletion layer, and thus the greater the flat-band potential. This can be caused by the increased number of species on the surface of the photoelectrode [67, 68]. The charge carrier concentration estimated for the films produced the highest and least values of approximately 40.02×10^{20} and 0.90×10^{20} cm^{-3} for CuO/Ag-1L and pristine CuO photocathodes respectively. The increased charge concentration and low V_{fb} values observed for the CuO/Ag modified films is an indication of improvement in the transfer of charges, and reduced charge recombination at the films surface [15, 48]

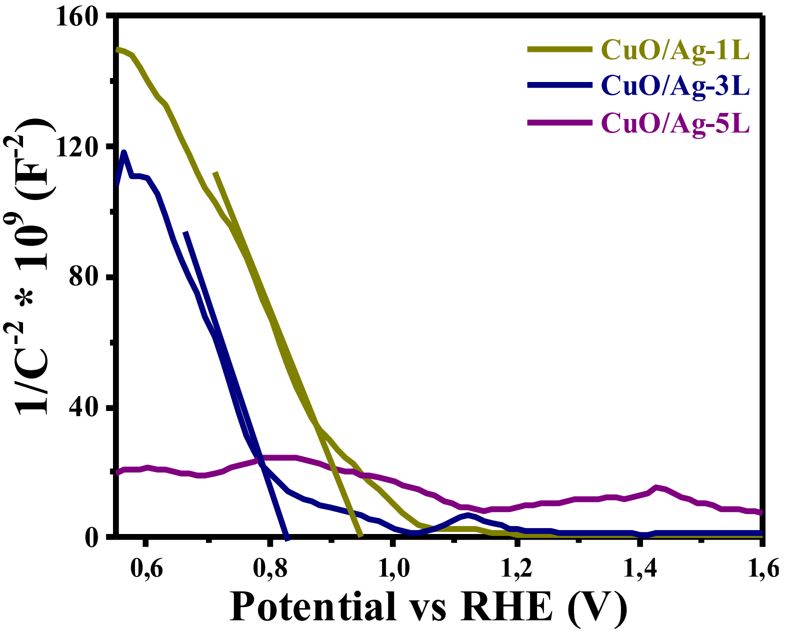

Figure 4.4.10 MS plots of pristine CuO/Ag-1L, CuO/Ag-3L and CuO/Ag-5L photocathodes.

Table 4.4.3 Table showing V_{fb} and N_d estimated from the MS plots of pristine CuO and CuO photocathodes coated with 1 and 3 layers of Ag NPs.

Sample	**V_{fb} vs RHE (V)**	**N_D * 10^{20} (cm^{-3})**
CuO Pristine	1.049	0.90
CuO/Ag-1L	0.959	40.02
CuO/Ag-3L	0.844	36.01

To study the influence of Ag on the stability of CuO photocathodes, chronoamperometry measurements were performed on CuO/Ag-1L, CuO/Ag-3L, and CuO/Ag-5L films, respectively. Figure 4.4.11 shows the photo-current density of the films at a constant potential of 0.5 V vs RHE for a time scan of 1200 s in a 1 M NaOH electrolyte. The CuO/Ag-1L, CuO/Ag-3L, and CuO/Ag-5L photocathodes retained about 74.5, 60.0 and 75.9 % of their photo-current density after 500 s respectively. This represents a significant improvement in the photo-stability the films in electrolyte when compared to the 28.4 % of photo-current retained by the pristine CuO photocathodes after the same duration of 500 s. The CuO/Ag-1L, CuO/Ag-3L, and CuO/Ag-5L photocathodes further retained about 65.9, 47.3 and 74.7 % of their photo-current density after a scan of 1200 s respectively. The improved photo-stability observed for the CuO/Ag films suggests that a large portion of the photo-current density observed for the films in Figure **4.4.*8*** will result in the reduction of H_2O.

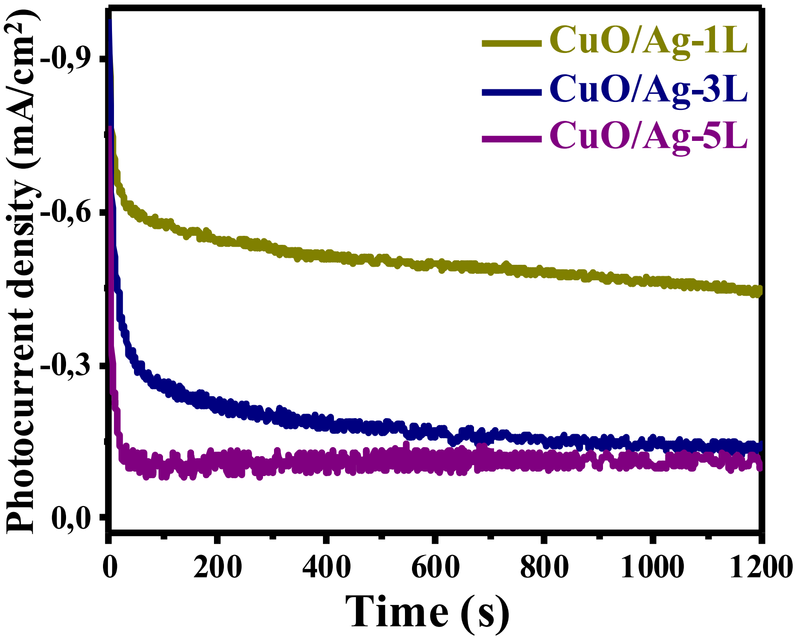

Figure 4.4.11 Photo-stability measurements performed at 0.5 V vs RHE on the CuO/Ag-1L, CuO/Ag-3L and CuO/Ag-5L photocathodes.

4.5 CuO thin films modified with Au nanoparticles for improved photo-stability in electrolyte

In this section, the results obtained from the morphological, structural, optical and PEC studies of the pristine CuO films and the ones modified with 1, 3, and 5 layers of Au nanoparticles are discussed. The protective layers of Au were deposited on CuO to help improve its photo-stability in electrolyte. These results are presented in sections 4.5.1 to 4.5.5.

4.5.1 Structural properties

Structural properties of CuO thin films consisting of 1, 3, 5 layers of Au were studied using XRD. The measurements were performed within a 2 theta range of 20 - 80° and the results are given in Figure **4.5.*1***. The diffraction peaks at ($\bar{1}$11) and (111) planes were observed for all the samples, confirming the monoclinic crystal structure of the CuO films. Furthermore, the diffraction peaks attributed to Au at (111), (200), (220), and (311) planes emerge for CuO films coated with 3 and 5 layers of the Au NPs. According to JCPDS no. 01-071-3755, these planes confirm the face-centered cubic structure of Au, with a lattice constant a = 4.077 Å [69, 70]. The 1-layer CuO/Au film did not show any Au diffraction peaks due to the small amount of Au NPs deposited on the surface.

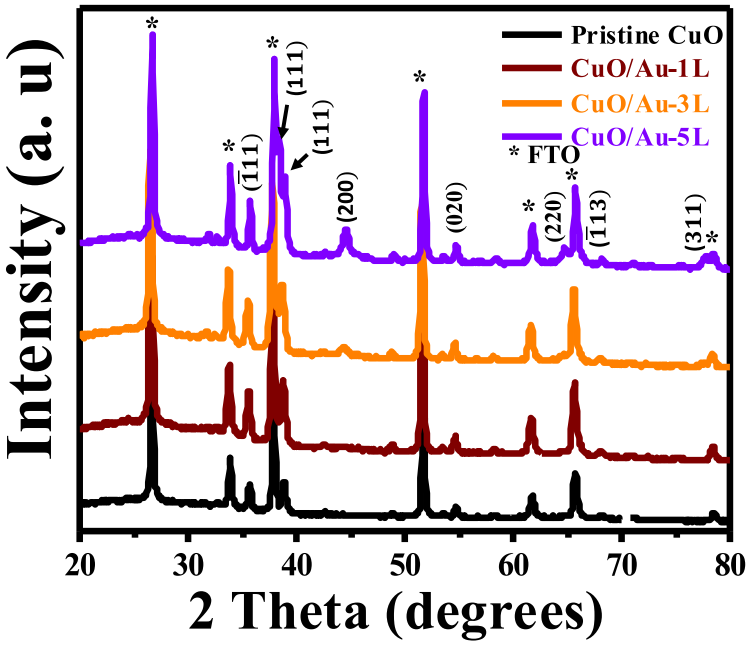

Figure 4.5.1 XRD patterns of a pristine CuO film, as well as CuO films coated with 1, 3, 5 layers of Au NPs.

To study the influence of Au NPs on the crystallization of the CuO thin films, the peaks at $(\bar{1}11)$ were used to obtain the full width at half maximum (FWHM) and crystal size values of the prepared films. The FWHM and estimated crystal sizes of the thin films are presented in Table 4.5.1. The Au NPs are observed to have no significant influence on the crystal sizes of the CuO thin films.

Table 4.5.1 XRD analysis showing the FWHM and crystal sizes of a the pristine CuO thin film and the ones coated with 1, 3, and 5 layers of Au NPs.

Sample	2 theta	FWHM	Crystal size (nm)
Pristine CuO	36.08	0.38	19.89
CuO/Au-1L	35.56	0.41	18.46
CuO/Au-3L	35.50	0.37	20.46
CuO/Au-5L	35.71	0.36	21.02

Raman spectroscopy was further utilized to study the structural properties of the films by obtaining their phonon modes vibrations. The Raman spectra of the pristine CuO films and the ones coated with 1, 3, 5 layers of Au are given in Figure **4.5.*1***. The spectra revealed one A_g Raman active phonon mode at 302 cm^{-1} and two B_g phonon modes at 250 and 638 cm^{-1} which belong to CuO [1, 11]. Additional vibrational modes were observed at 773, 1124, 1185, 1364, 1507 and 1546 cm^{-1} when CuO films were coated with AuNPs, further confirming the presence of Au.

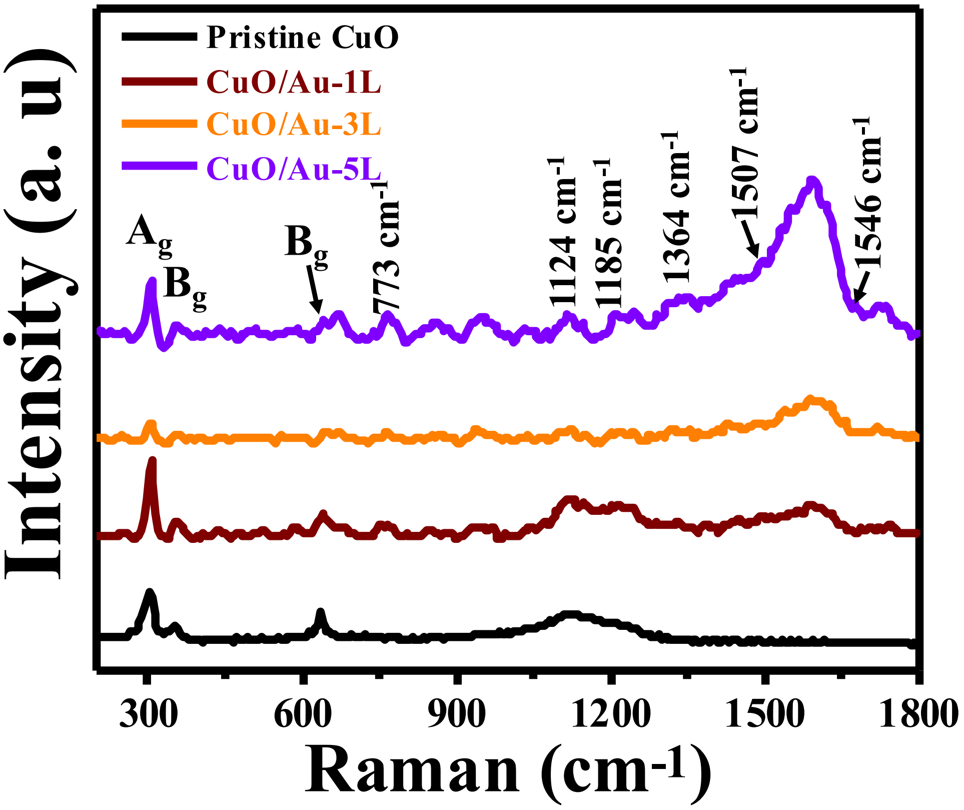

Figure 4.5.2 Raman spectra of a pristine CuO film, as well as CuO films coated with 1, 3, 5 layers of Au NPs.

4.5.2. Surface morphology and film thickness

FE-SEM was utilized to investigate the influence of Au NPs on the surface morphology of the CuO thin films. The surface morphology of CuO films coated with 1 and 3 layers of Au NPs shown in Figure 4.5.3 (a) and (b) revealed spherical CuO nanostructures which have been largely covered with densely packed Au NPs. The morphology of the CuO films covered with

5 layers Au NPs (Figure 4.5.3 (d)) shows an extremely agglomerated and coalesced AuNPs on the CuO film's surface. The grain sizes of CuO/Au films could not be estimated due to the high agglomeration of the Au NPs on CuO films.

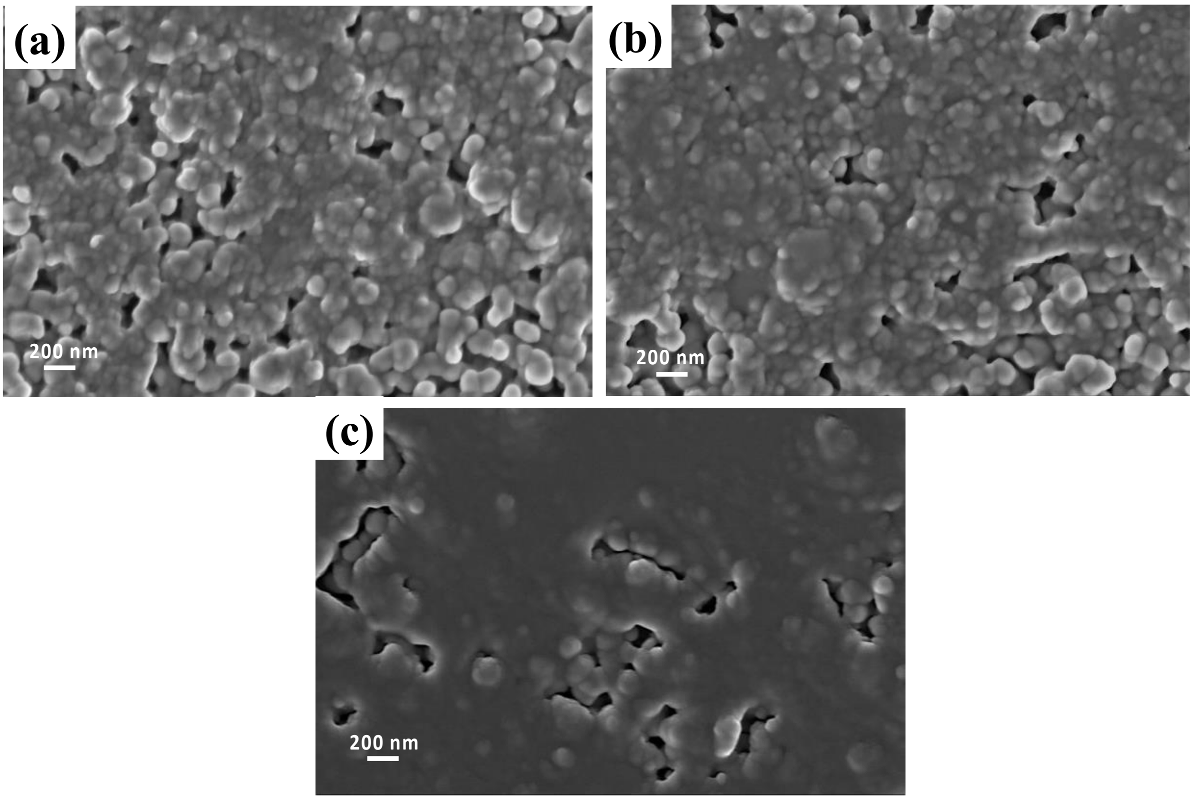

Figure 4.5.3 SEM images of **(a)** CuO/Au-1L **(b)** CuO/Au-3L and **(c)** CuO/Au-5L thin films.

Cross-sectional views of a pristine CuO and CuO films loaded with Au were analysed using FE-SEM. The cross-sectional images of the CuO films coated with 1, 3, and 5 layers of Au are presented in Figure 4.5.4 (a), (b), (c). The average thicknesses of the films were estimated to be 24.02, 55.84 and 111.41 nm respectively.

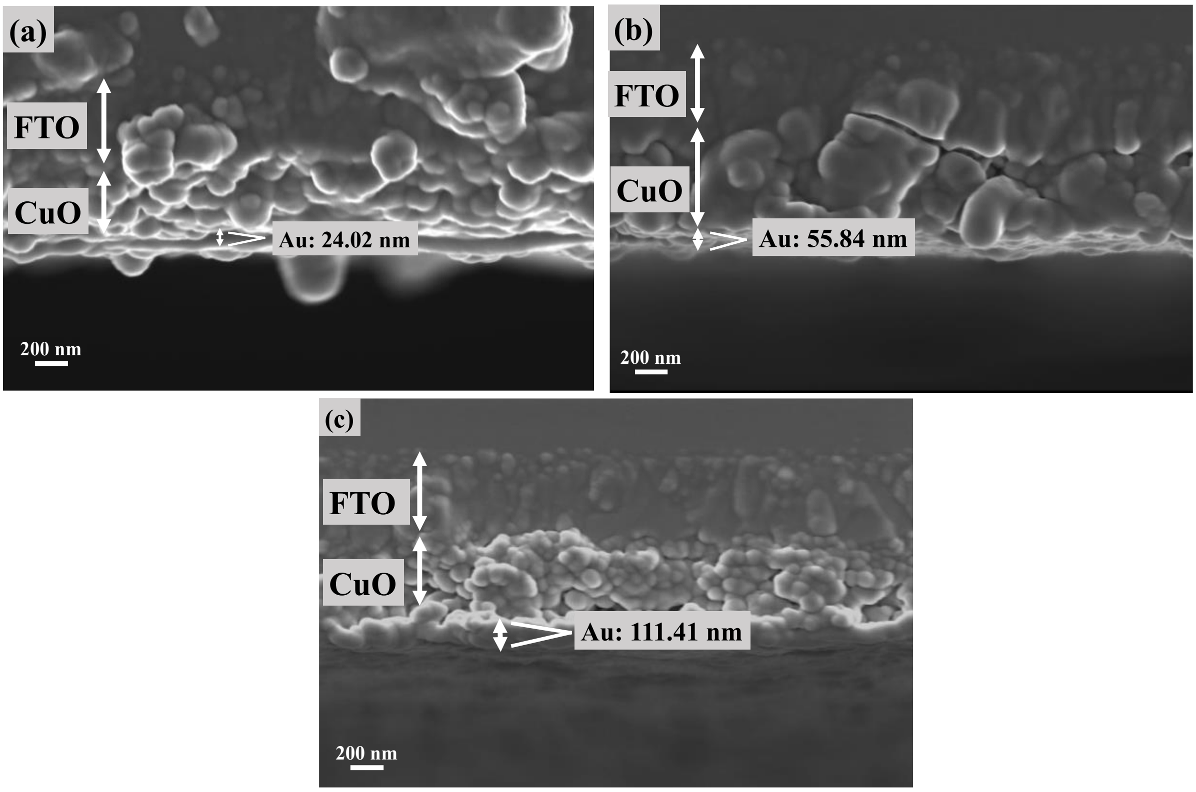

Figure 4.5.4 FE-SEM of cross-sectional images of **(a)** CuO/Au-1L **(b)** CuO/Au-3L and **(c)** CuO/Au-5L thin films.

4.5.3 Elemental composition

EDS was used to verify the absence of impurities and to confirm the elemental composition CuO/Au films. The EDS analysis of CuO/Au thin films consisting of 1, 3, and 5 layers of AuNPs are given in Figure 4.5.5 (a), (b) and (c) respectively. The presence of oxygen (O) and copper (Cu) was confirmed for all the films since they are the constituent elements of CuO. The analysis also verifies the presence of Au in the CuO thin films consisting of 1, 3, and 5 Layers of Au NPs.

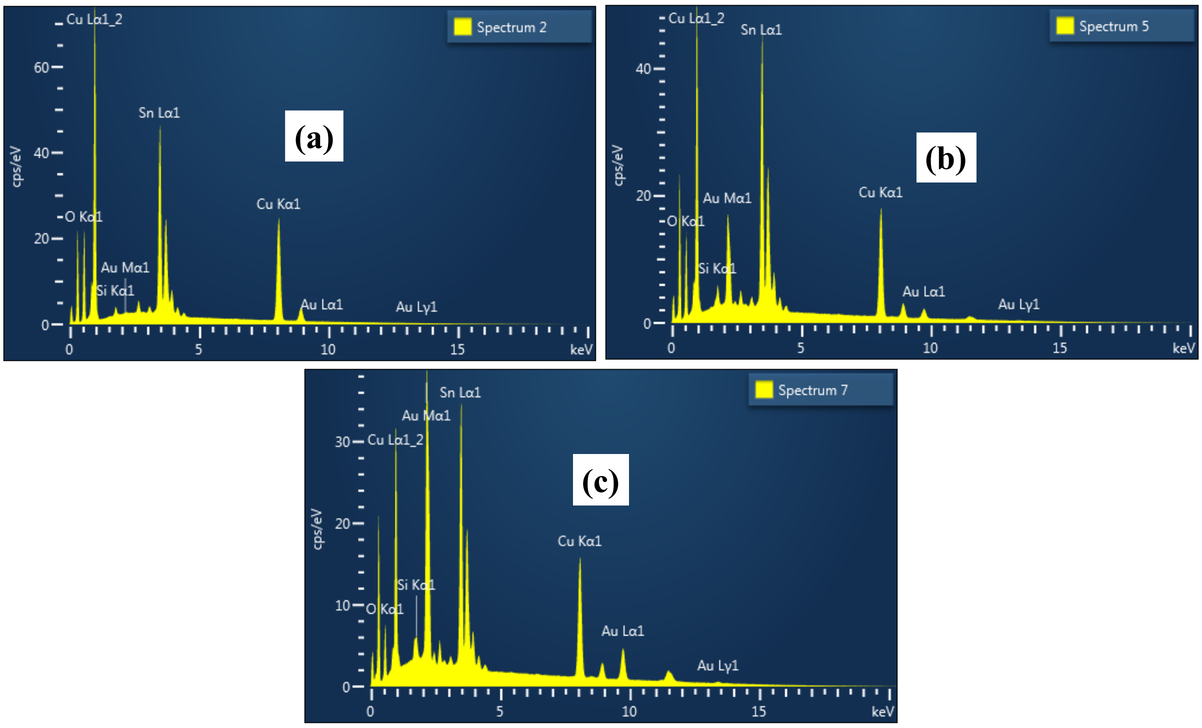

Figure 4.5.5 EDS spectrum of **(a)** CuO/Au-1L, **(b)** CuO/Au-3L, and **(c)** CuO/Au-5L thin films.

4.5.4. Optical properties

UV-Vis spectroscopy was done to investigate the optical absorption, transmittance and the indirect bandgap of the films. Figure 4.5.6 shows the optical absorption and transmittance of the pristine CuO films and the ones consisting of 1, 3, 5 layers of Au. All films exhibit photo-absorption in the visible region, with a slight absorption in the near-infrared region. The photo-absorbance of CuO films was observed to increase for samples decorated with Au NPs which was similar with other results that have been reported in literature [69]. This may be attributed to the increased scattering of photons caused by large amounts of Au NPs on the films surface.

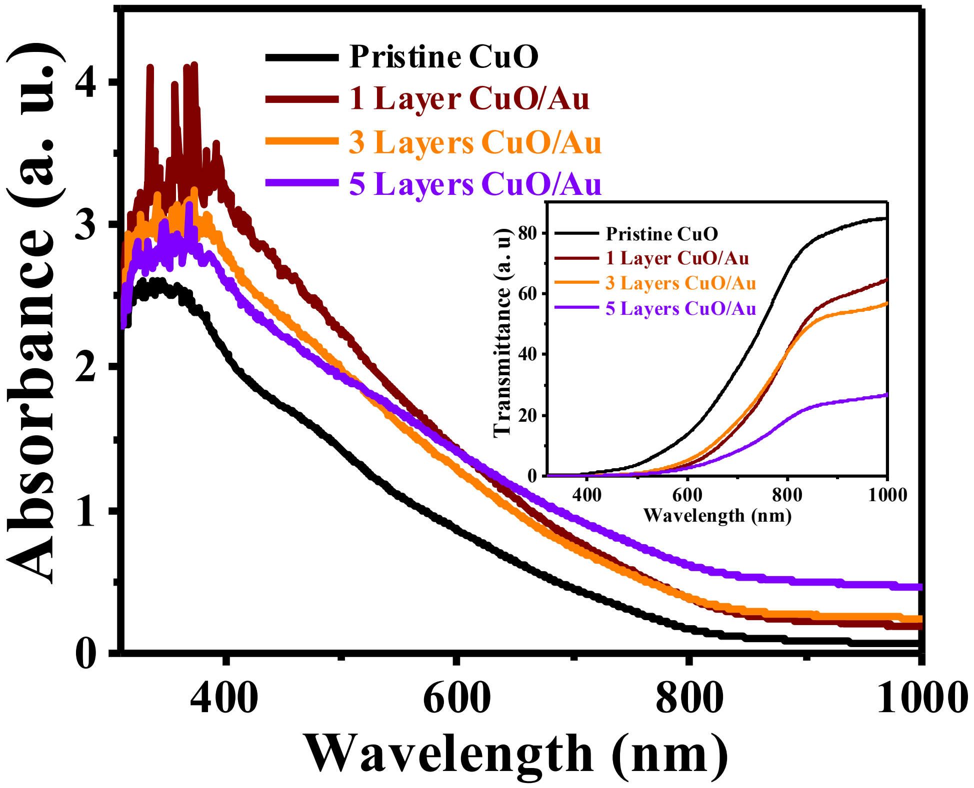

Figure 4.5.6 UV–Vis spectra of pristine CuO thin films and the ones coated with 1, 3, and 5 layers of AuNPs.

The Tauc plots for the indirect transitions of the pristine and Au coated CuO thin films are given in Figure 4.5.7. The optical band gaps of all films were estimated from the Tauc plots as earlier explained in section 4.2.4. The indirect band gap for CuO/Au-1L and CuO/Au-3L thin films was estimated to be 1.20 ± 0.03 eV, whereas for CuO/Au-5L the value declined to 1.13 eV. The narrowed bandgap observed for the CuO/Au-5L films was caused by the free electrons produced by the large amount of Au NPs deposited on the surface of the CuO samples [71]. The decreased bandgap aligns with studies previously reported in literature for CuO/Au films [23, 72, 73].

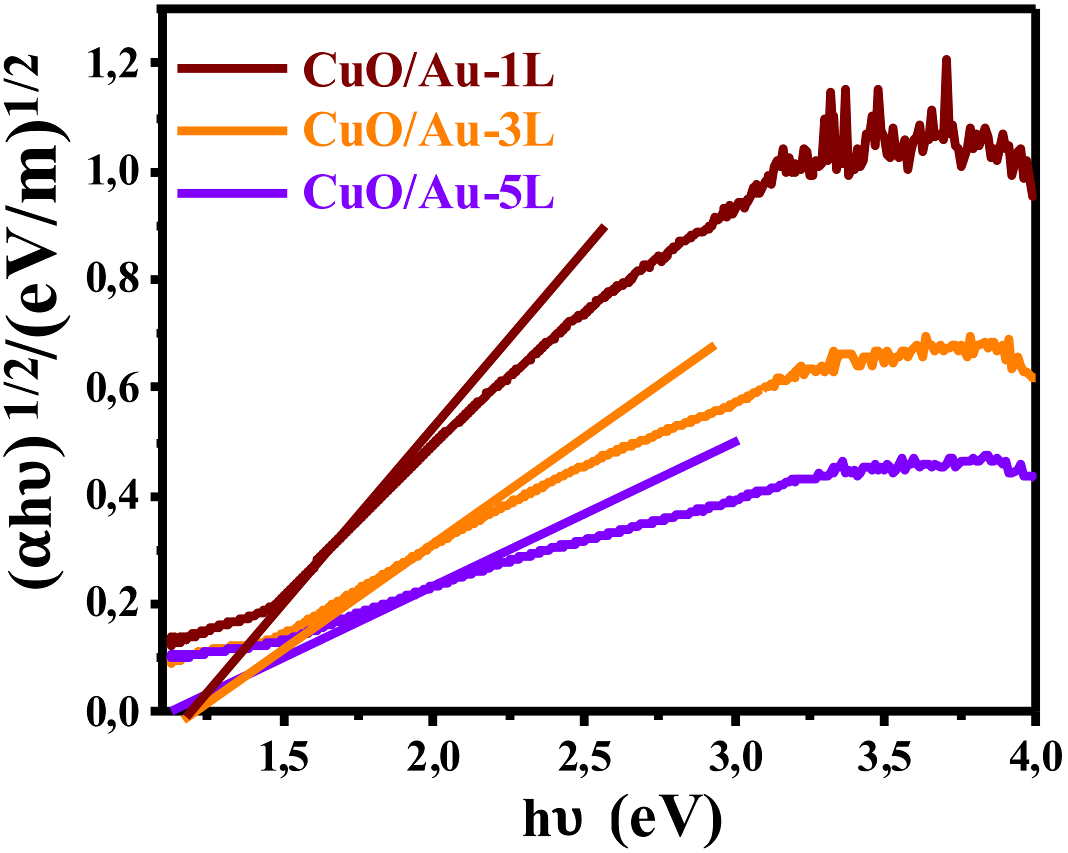

Figure 4.5.7 Tauc approximation for indirect bandgaps of CuO thin films coated with 1, 3, and 5 layers of Au.

4.5.5 Photoelectrochemical properties

LSV measurements were done to obtain the photo-current response of the CuO/Au films. Figure **4.5.*8*** presents the photo-current densities of the samples at different potentials. The pristine CuO films produced the highest photo-current density of 2.9 mA/cm^2 at 0.35 V vs RHE, whereas the least photo-current of about 1.1 mA/cm^2 was observed for CuO/Au-1L and CuO/Au-3L films at the same potential vs RHE. The obtained photo-current density was 42.9 % less than the value obtained for the pristine films at the same potential. The decrease in the photo-current density of the CuO/Au photocathodes could be attributed to the prevention of photo-corrosion which significantly enhanced the current response of the pristine CuO films under illumination.

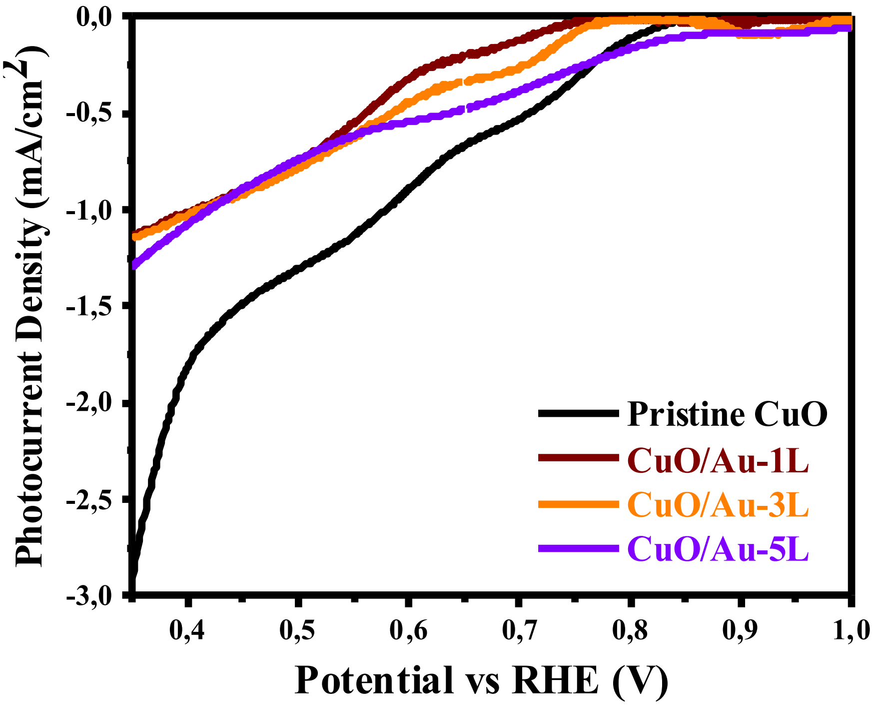

Figure 4.5.8 Photo-current density of pristine CuO and CuO/Au photocathodes.

EIS measurements were also performed on the CuO/Au photocathodes to analyse the charge transfer processes occurring at the solid/liquid interface of the films. Figure **4.5.*9*** shows the Nyquist plot of the EIS experimental and fitted data for the pristine CuO and CuO/Au photocathodes. The Randles circuit consisting of a resistor, Rs, in series with a parallel connection of CPE and Rct, given in Figure **4.2.*14*** (d) was also used to fit the EIS experimental data obtained for the CuO/Au films. The components of the Randles circuit represent the same physical processes as explained in section 4.2.5.

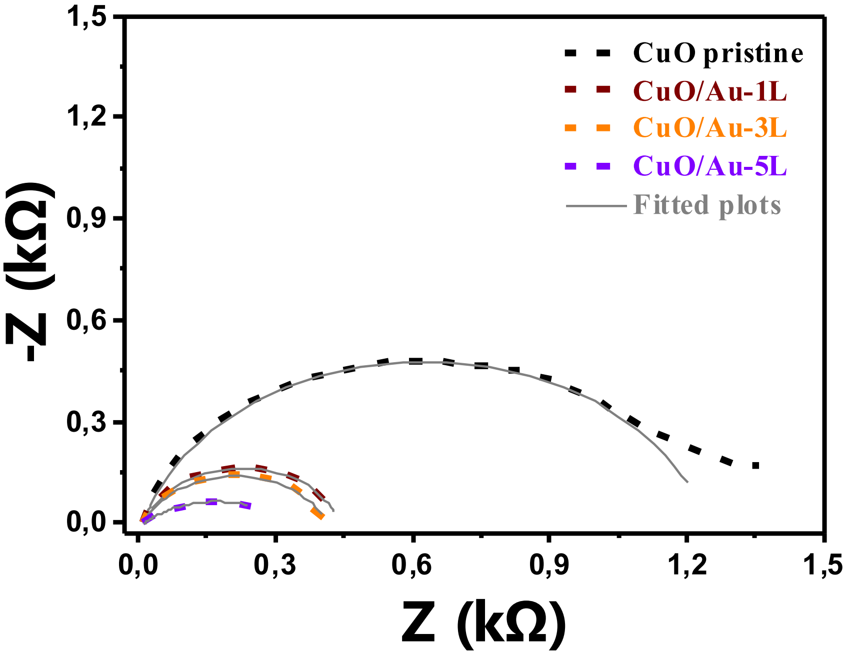

Figure 4.5.9 Electrochemical Impedance Spectra (EIS) of pristine CuO, CuO/Au-1L, CuO/Au-3L and CuO/Au-5L photocathodes.

Table 4.5.2 The values obtained for the different elements after fitting the EIS data to the circuit model using ZView software.

Sample	**Rs (Ω)**	**Rct (kΩ)**	**CPE (µF)**
CuO pristine	9.29	1.24	128.8
CuO/Au-1L	11.62	0.43	320.1
CuO/Au-3L	9.07	0.4	262.4
CuO/Au-5L	8.04	0.32	1758.6

Table 4.5.2 shows the values estimated for the different elements of the circuit model used to fit the raw EIS measurements. The least charge transfer resistance with the value of 0.32 kΩ was produced by CuO/Au-5L, while pristine CuO yielded the highest value of 1.24 kΩ. Au NPs have been shown to enhance charge transport and migration during photocatalysis when deposited on the surface of a photoelectrode [23, 74]. Hence the integration of the Au NPs on CuO photocathodes improved the movement of electrons across the photoelectrode/electrolyte interface, decreasing their charge transfer resistance. Despite having lower Rct values, the CuO/Au films yielded lower photo-current densities at 0.5 V vs RHE compared to the pristine

CuO photocathodes. This was because a large part of the photo-current obtained for the pristine CuO films was due to photo-corrosion processes occurring on the surface of the films as explained in section 4.5.5. This is evident in the poor stability showed by the pristine CuO films (Figure **4.2.*13***).

To obtain the charge carrier concentration (N_A) and flat-band potentials (V_{fb}), Mott-Schottky measurements were also performed on the CuO photocathodes coated with 1, 3, and 5 layers of Au. MS plots of all CuO/Au photocathodes are presented in Figure **4.5.*10***, whereas the MS plot for pristine CuO was earlier given in Figure **4.3.*10***. The approximate values of V_{FB} and N_A extracted from the MS plots are given in **Table 4.5.*3***. Pristine CuO produced a slightly higher flat-band potential values which was at least about 18 mV more positive than the values obtained for the CuO/Au films. This contributed to the slightly earlier photo-current onset observed for the pristine CuO films (Figure **4.5.*8***). The shift to a more negative flat band potential observed for the CuO/Au films may be attributed to the achieved equilibrium between the fermi levels of CuO and Au when the composite photocathodes were formed. The charge carrier concentration obtained for the CuO/Au films ranges between 6.75-5.64 x 10^{20} cm^{-3}, which was at least over 6.3 times higher than the values obtained for the pristine films. Enhanced charge carrier concentration estimated for the CuO/Au photocathodes will enhance their charge mobility and transport, limiting election-hole recombination in the bulk and surface of the films [15]. This contributed to the reduced Rct values obtained for the CuO/Au photocathodes (**Table 4.5.*2***).

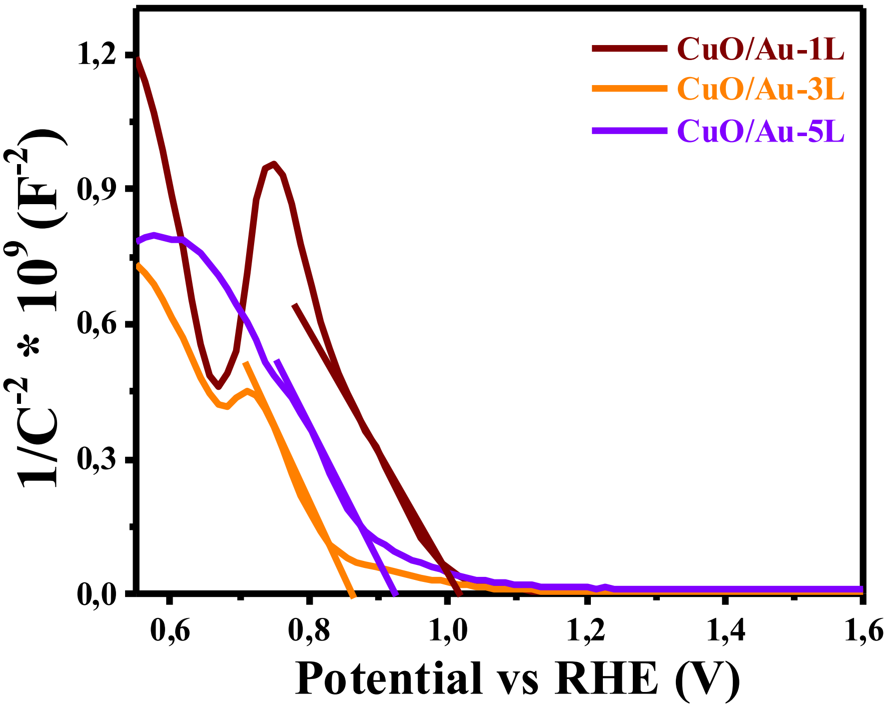

Figure 4.5.10 MS plots of CuO/Au-1L, CuO/Au-3L and CuO/Au-5L photocathodes.

Table 4.5.3 Table showing V_{fb} and N_d estimated from the MS plots of pristine CuO and CuO photocathodes coated with 1, 3, and 5 layers of Au NPs.

Sample	**V_{fb} vs RHE (V)**	**N_D * 10^{20} (cm^{-3})**
CuO Pristine	1.049	0.90
CuO /Au-1L	1.031	6.75
CuO/Au-3L	0.877	5.64
CuO/Au-5L	0.940	6.38

Chronoamperometry measurements were performed in dark and under illumination to study the stability of CuO/Au-1L, CuO/Au-3L and CuO/Au-5L thin films in electrolyte. The photo-current densities of the photocathodes were obtained at a fixed potential of 0.5 V vs RHE, for a time-scan of 1200 s, and the results are shown in Figure **4.5.*11***. The CuO/Au-1L, CuO/Au-3L, and CuO/Au-5L photocathodes retained about 65.0, 85.1 and 87.9 % of their photo-current density after 500 s respectively. This represents a significant improvement in the photo-stability of the films in electrolyte when compared to the 28.4 % of photo-current retained by the pristine CuO photocathodes after the same duration of 500 s. More so, the CuO/Au-1L, CuO/Au-3L, and CuO/Au-5L photocathodes further retained about 58.4, 83.6, and 84.3 % of their photo-current density after a scan of 1200 s, respectively. The improved photo-stability observed for the CuO/Au films indicates that a large portion of the photo-current density observed for the films in Figure **4.4.*8*** may result in the reduction of H_2O. The CuO/Au-3L and CuO/Au-5L photocathodes showed a significantly enhanced photo-stability in electrolyte. However, the samples still produced less photo-current density compared to the pristine films (Figure **4.5.*8***). This again suggest that more research need to be done to further improve the photo-current density of CuO/Au photocathodes while maintaining or further enhancing its photo-stability under aqueous electrolytes.

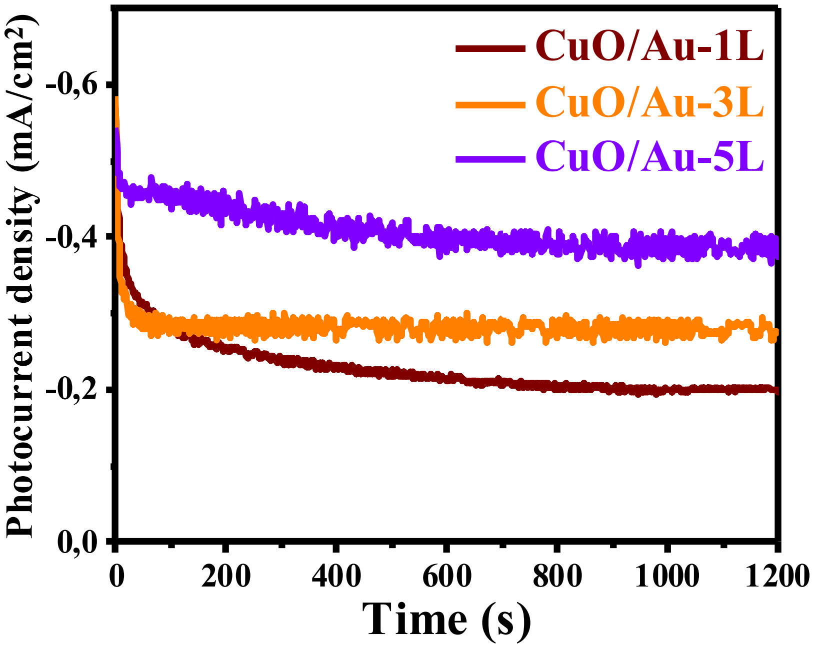

Figure 4.5.11 Photo-stability measurements performed at 0.5 V vs RHE on CuO/Au-1L, CuO/Au-3L and CuO/Au-5L photocathodes.

References

[1] P. I. Kyesmen, N. Nombona, and M. Diale, "Heterojunction of nanostructured α-Fe2O3/CuO for enhancement of photoelectrochemical water splitting," *Journal of Alloys and Compounds*, vol. 863, p. 158724, 2021.

[2] H. B. Saâd, M. Ajili, S. Dabbabi, and N. T. Kamoun, "Investigation on thickness and annealing effects on physical properties and electrical circuit model of CuO sprayed thin films," *Superlattices and Microstructures*, vol. 142, p. 106508, 2020.

[3] C. Brinker, G. Frye, A. Hurd, and C. Ashley, "Fundamentals of sol-gel dip coating," *Thin solid films,* vol. 201, no. 1, pp. 97-108, 1991.

[4] Y. Akaltun, "Effect of thickness on the structural and optical properties of CuO thin films grown by successive ionic layer adsorption and reaction," *Thin Solid Films,* vol. 594, pp. 30-34, 2015.

[5] F. A. Akgul, G. Akgul, N. Yildirim, H. E. Unalan, and R. Turan, "Influence of thermal annealing on microstructural, morphological, optical properties and surface electronic structure of copper oxide thin films," *Materials Chemistry and Physics,* vol. 147, no. 3, pp. 987-995, 2014.

[6] P. I. Kyesmen, N. Nombona, and M. Diale, "Influence of coating techniques on the optical and structural properties of hematite thin films," *Surfaces and Interfaces,* vol. 17, p. 100384, 2019.

[7] P. Peerakiatkhajohn, J.-H. Yun, S. Wang, and L. Wang, "Review of recent progress in unassisted photoelectrochemical water splitting: from material modification to configuration design," *Journal of Photonics for Energy,* vol. 7, no. 1, p. 012006, 2016.

[8] J. Joy, J. Mathew, and S. C. George, "Nanomaterials for photoelectrochemical water splitting–review," *international journal of hydrogen energy,* vol. 43, no. 10, pp. 4804-4817, 2018.

[9] W. Wang, Z. Liu, Y. Liu, C. Xu, C. Zheng, and G. Wang, "A simple wet-chemical synthesis and characterization of CuO nanorods," *Applied Physics A,* vol. 76, no. 3, pp. 417-420, 2003.

[10] T. H. Tran and V. T. Nguyen, "Copper oxide nanomaterials prepared by solution methods, some properties, and potential applications: a brief review," *International scholarly research notices,* vol. 2014, 2014.

[11] J. Xu *et al.*, "Raman spectra of CuO nanocrystals," *Journal of Raman spectroscopy,* vol. 30, no. 5, pp. 413-415, 1999.

[12] M. Dhaouadi *et al.*, "Physical properties of copper oxide thin films prepared by sol–gel spin–coating method," *Am. J. Phys. Appl,* vol. 6, no. 2, pp. 43-50, 2018.

[13] S. Shariffudin, S. Khalid, N. Sahat, M. Sarah, and H. Hashim, "Preparation and characterization of nanostructured CuO thin films using sol-gel dip coating," in *IOP Conference Series: Materials Science and Engineering*, 2015, vol. 99, no. 1: IOP Publishing, p. 012007.

[14] N. Sangwaranatee, N. Sangwaranatee, M. Horprathum, C. Chananonnawathorn, and E. Sustini, "Influence of film thickness on microstructural and electrical properties of copper oxide thin film prepared by magnetron sputtering," *Materials Today: Proceedings,* vol. 5, no. 7, pp. 15198-15202, 2018.

[15] P. I. Kyesmen, N. Nombona, and M. Diale, "A Promising Three-Step Heat Treatment Process for Preparing CuO Films for Photocatalytic Hydrogen Evolution from Water," *ACS Omega,* 2021.

[16] J. Sultana, S. Paul, A. Karmakar, G. K. Dalapati, and S. Chattopadhyay, "Optimizing the thermal annealing temperature: technological route for tuning the photo-detecting property of p-CuO thin films grown by chemical bath deposition method," *Journal of Materials Science: Materials in Electronics,* vol. 29, no. 15, pp. 12878-12887, 2018.

[17] H. Jun *et al.*, "Photoelectrochemical water splitting over ordered honeycomb hematite electrodes stabilized by alumina shielding," *Energy & Environmental Science,* vol. 5, no. 4, pp. 6375-6382, 2012.

[18] X. Chen *et al.*, "Three-dimensional porous g-C3N4 for highly efficient photocatalytic overall water splitting," *Nano Energy,* vol. 59, pp. 644-650, 2019.

[19] C. J. Brinker and G. W. Scherer, *Sol-gel science: the physics and chemistry of sol-gel processing*. Academic press, 2013.

[20] S. Aydemir, "Effects of withdrawal speed on the microstructural and optical properties of sol–gel grown ZnO: Al thin films," *Vacuum,* vol. 120, pp. 51-58, 2015.

[21] Z. N. Kayani, A. Aslam, R. Ishaque, S. N. Zahra, H. Hanif, and H. Khan, "The effect of the withdrawal speed on properties of nickel oxide thin films," *Zeitschrift für Kristallographie-Crystalline Materials,* vol. 234, no. 10, pp. 647-655, 2019.

[22] J. Tauc, "The optical properties of solids," *The Optical Properties of Solids,* 1966.

[23] R. A. Ismail and R. S. A. Hamed, "Decoration of copper oxide nanoplatelets with gold nanoparticles by laser ablation in methanol for photodetection applications," *Optical and Quantum Electronics,* vol. 50, no. 7, pp. 1-15, 2018.

[24] Z. Wang and L. Wang, "Photoelectrode for water splitting: Materials, fabrication and characterization," *Science China Materials,* vol. 61, no. 6, pp. 806-821, 2018.

[25] A. Kudo and Y. Miseki, "Heterogeneous photocatalyst materials for water splitting," *Chemical Society Reviews,* vol. 38, no. 1, pp. 253-278, 2009.

[26] T. Hisatomi, J. Kubota, and K. Domen, "Recent advances in semiconductors for photocatalytic and photoelectrochemical water splitting," *Chemical Society Reviews,* vol. 43, no. 22, pp. 7520-7535, 2014.

[27] S. Masudy-Panah *et al.*, "Nanocrystal engineering of sputter-grown CuO photocathode for visible-light-driven electrochemical water splitting," *ACS applied materials & interfaces,* vol. 8, no. 2, pp. 1206-1213, 2016.

[28] A. Mahmood, F. Tezcan, and G. Kardaş, "Photoelectrochemical characteristics of CuO films with different electrodeposition time," *International Journal of Hydrogen Energy,* vol. 42, no. 36, pp. 23268-23275, 2017.

[29] S. Masudy-Panah, R. S. Moakhar, C. S. Chua, A. Kushwaha, T. I. Wong, and G. K. Dalapati, "Rapid thermal annealing assisted stability and efficiency enhancement in a sputter deposited CuO photocathode," *RSC advances,* vol. 6, no. 35, pp. 29383-29390, 2016.

[30] M. Lamers, S. Fiechter, D. Friedrich, F. F. Abdi, and R. van de Krol, "Formation and suppression of defects during heat treatment of BiVO 4 photoanodes for solar water splitting," *Journal of Materials Chemistry A,* vol. 6, no. 38, pp. 18694-18700, 2018.

[31] F. Du, Q.-Y. Chen, and Y.-H. Wang, "Effect of annealing process on the heterostructure CuO/Cu2O as a highly efficient photocathode for photoelectrochemical water reduction," *Journal of Physics and Chemistry of Solids,* vol. 104, pp. 139-144, 2017.

[32] Y. Chen, A. Li, Q. Li, X. Hou, L.-N. Wang, and Z.-H. Huang, "Facile fabrication of three-dimensional interconnected nanoporous N-TiO2 for efficient photoelectrochemical water splitting," *Journal of materials science & technology,* vol. 34, no. 6, pp. 955-960, 2018.

[33] P. Córdoba-Torres, T. J. Mesquita, and R. P. Nogueira, "Relationship between the origin of constant-phase element behavior in electrochemical impedance spectroscopy and electrode surface structure," *The Journal of Physical Chemistry C,* vol. 119, no. 8, pp. 4136-4147, 2015.

[34] J. Toupin, H. Strubb, S. Kressman, V. Artero, N. Krins, and C. Laberty-Robert, "CuO photoelectrodes synthesized by the sol–gel method for water splitting," *Journal of Sol-Gel Science and Technology,* vol. 89, no. 1, pp. 255-263, 2019.

[35] R. S. Neves, E. De Robertis, and A. J. Motheo, "Capacitance dispersion in EIS measurements of halides adsorption on Au (2 1 0)," *Electrochimica acta,* vol. 51, no. 7, pp. 1215-1224, 2006.

[36] H. Xing, E. Lei, Z. Guo, D. Zhao, X. Li, and Z. Liu, "Exposing the photocorrosion mechanism and control strategies of a CuO photocathode," *Inorganic Chemistry Frontiers,* vol. 6, no. 9, pp. 2488-2499, 2019.

[37] M. Basu, "Porous cupric oxide: efficient photocathode for photoelectrochemical water splitting," *ChemPhotoChem,* vol. 3, no. 12, pp. 1254-1262, 2019.

[38] H. Gerischer, "On the stability of semiconductor electrodes against photodecomposition," *Journal of Electroanalytical Chemistry and Interfacial Electrochemistry,* vol. 82, no. 1-2, pp. 133-143, 1977.

[39] A. Cots, P. Bonete, and R. Gómez, "Improving the stability and efficiency of CuO photocathodes for solar hydrogen production through modification with iron," *ACS applied materials & interfaces,* vol. 10, no. 31, pp. 26348-26356, 2018.

[40] H. Tang *et al.*, "Enhancing the stability of CuO thin-film photoelectrodes by Ti alloying," *Journal of electronic materials,* vol. 41, no. 11, pp. 3062-3067, 2012.

[41] A. Ranjitha, N. Muthukumarasamy, M. Thambidurai, D. Velauthapillai, R. Balasundaraprabhu, and S. Agilan, "Fabrication of Ni-doped TiO2 thin film photoelectrode for solar cells," *Solar energy,* vol. 106, pp. 159-165, 2014.

[42] Z. Wang *et al.*, "Identifying copper vacancies and their role in the CuO based photocathode for water splitting," *Angewandte Chemie,* vol. 131, no. 49, pp. 17768-17773, 2019.

[43] R. Liu, Z. Zheng, J. Spurgeon, and X. Yang, "Enhanced photoelectrochemical water-splitting performance of semiconductors by surface passivation layers," *Energy & Environmental Science,* vol. 7, no. 8, pp. 2504-2517, 2014.

[44] G. S. Pawar, A. Elikkottil, B. Pesala, A. A. Tahir, and T. K. Mallick, "Plasmonic nickel nanoparticles decorated on to LaFeO3 photocathode for enhanced solar hydrogen generation," *International Journal of Hydrogen Energy,* vol. 44, no. 2, pp. 578-586, 2019.

[45] S. Pokrant, S. Dilger, S. Landsmann, and M. Trottmann, "Size effects of cocatalysts in photoelectrochemical and photocatalytic water splitting," *Materials Today Energy,* vol. 5, pp. 158-163, 2017.

[46] E. Thimsen, F. Le Formal, M. Gratzel, and S. C. Warren, "Influence of plasmonic Au nanoparticles on the photoactivity of Fe2O3 electrodes for water splitting," *Nano letters,* vol. 11, no. 1, pp. 35-43, 2011.

[47] S. R. AR, B. M. Momin, H. M. Wilson, U. S. Annapure, and N. Jha, "Optimal fabrication of 0D/1D Cu2O quantum dots sensitized CdS nanorods heterojunction: Efficient photoredox catalyst for H2 generation under visible light irradiation," *Journal of Alloys and Compounds,* vol. 835, p. 155262, 2020.

[48] C. Xiao, B. Lei, W. Jin, and L. Xu, "Candle flame fabrication of carbon coated CuO-Cu2O composite photocathode for photoelectrochemical water reduction," *Materials Letters,* vol. 298, p. 130006, 2021.

[49] P. P. Kunturu and J. Huskens, "Efficient solar water splitting photocathodes comprising a copper oxide heterostructure protected by a thin carbon layer," *ACS Applied Energy Materials,* vol. 2, no. 11, pp. 7850-7860, 2019.

[50] S. Xie *et al.*, "Enhanced photoactivity and stability of carbon and nitrogen co-treated ZnO nanorod arrays for photoelectrochemical water splitting," *Journal of Materials Chemistry,* vol. 22, no. 28, pp. 14272-14275, 2012.

[51] A. Mohammad-Khah and R. Ansari, "Activated charcoal: preparation, characterization and applications: a review article," *Int J Chem Tech Res,* vol. 1, no. 4, pp. 859-864, 2009.

[52] W. Shi, X. Zhang, S. Li, B. Zhang, M. Wang, and Y. Shen, "Carbon coated Cu2O nanowires for photo-electrochemical water splitting with enhanced activity," *Applied Surface Science,* vol. 358, pp. 404-411, 2015.

[53] H. O. Panganoron, J. D. A. Pascasio, E. A. Esparcia, J. A. D. del Rosario, and J. D. Ocon, "Hydrothermally Carbonized Waste Biomass as Electrocatalyst Support for α-MnO2 in Oxygen Reduction Reaction," *Catalysts,* vol. 10, no. 2, p. 177, 2020.

[54] J. Hou, C. Yang, H. Cheng, S. Jiao, O. Takeda, and H. Zhu, "High-performance p-Cu 2 O/n-TaON heterojunction nanorod photoanodes passivated with an ultrathin carbon sheath for photoelectrochemical water splitting," *Energy & Environmental Science,* vol. 7, no. 11, pp. 3758-3768, 2014.

[55] K. Shameli *et al.*, "Green biosynthesis of silver nanoparticles using Curcuma longa tuber powder," *International journal of nanomedicine,* vol. 7, p. 5603, 2012.

[56] P. Wang *et al.*, "Highly efficient visible-light plasmonic photocatalyst Ag@ AgBr," *Chemistry–A European Journal,* vol. 15, no. 8, pp. 1821-1824, 2009.

[57] L. Sang, H. Ge, and B. Sun, "Probing plasmonic Ag nanoparticles on TiO2 nanotube arrays electrode for efficient solar water splitting," *International Journal of Hydrogen Energy,* vol. 44, no. 30, pp. 15787-15794, 2019.

[58] S. Hsieh, P.-Y. Lin, and L.-Y. Chu, "Improved performance of solution-phase surface-enhanced Raman scattering at Ag/CuO nanocomposite surfaces," *The Journal of Physical Chemistry C,* vol. 118, no. 23, pp. 12500-12505, 2014.

[59] Y. Wei *et al.*, "Enhanced photoelectrochemical water-splitting effect with a bent ZnO nanorod photoanode decorated with Ag nanoparticles," *Nanotechnology,* vol. 23, no. 23, p. 235401, 2012.

[60] Z. D. Mahmoudabadi, E. Eslami, and M. Narimisa, "Synthesis of Ag/TiO2 nanocomposite via plasma liquid interactions: Improved performance as photoanode in dye-sensitized solar cell," *Journal of colloid and interface science,* vol. 529, pp. 538-546, 2018.

[61] S. Pan and A. Gupta, "Surface-enhanced solar energy conversion systems using gold and silver nanoparticles," *Material Matters,* vol. 7, no. 4, pp. 64-66, 2012.

[62] M. E. Hafez, H. Ma, Y.-Y. Peng, W. Ma, and Y.-T. Long, "Correlated anodic–cathodic nanocollision events reveal redox behaviors of single silver nanoparticles," *The journal of physical chemistry letters,* vol. 10, no. 12, pp. 3276-3281, 2019.

[63] M. L. Teijelo, J. Vilche, and A. Arvia, "Comparative voltammetric behaviour of the silver/silver oxide electrode prepared on vitreous carbon and silver substrates," *Journal of applied electrochemistry,* vol. 18, no. 5, pp. 691-698, 1988.

[64] Y. L. Mikhlin *et al.*, "Oxidation of Ag nanoparticles in aqueous media: Effect of particle size and capping," *Applied Surface Science,* vol. 297, pp. 75-83, 2014.

[65] H.-Y. Jung, I.-S. Yeo, T.-U. Kim, H.-C. Ki, and H.-B. Gu, "Surface plasmon resonance effect of silver nanoparticles on a TiO2 electrode for dye-sensitized solar cells," *Applied Surface Science,* vol. 432, pp. 266-271, 2018.

[66] V. Madhavi and P. Kondaiah, "Influence of silver nanoparticles on titanium oxide and nitrogen doped titanium oxide thin films for sun light photocatalysis," *Applied Surface Science,* vol. 436, pp. 708-719, 2018.

[67] R. E. Adam *et al.*, "ZnO/Ag/Ag 2 WO 4 photo-electrodes with plasmonic behavior for enhanced photoelectrochemical water oxidation," *RSC advances,* vol. 9, no. 15, pp. 8271-8279, 2019.

[68] A. Kushwaha, R. S. Moakhar, G. K. Goh, and G. K. Dalapati, "Morphologically tailored CuO photocathode using aqueous solution technique for enhanced visible light driven

water splitting," *Journal of Photochemistry and Photobiology A: Chemistry,* vol. 337, pp. 54-61, 2017.

[69] P. J. Boruah, R. R. Khanikar, and H. Bailung, "Novel single-step synthesis and shape transformation of Au/CuO micro/nanocomposites using plasma-liquid interaction," *Nanotechnology,* vol. 32, no. 24, p. 245601, 2021.

[70] C.-J. Huang, P.-H. Chiu, Y.-H. Wang, W. R. Chen, and T. H. Meen, "Synthesis of the gold nanocubes by electrochemical technique," *Journal of The Electrochemical Society,* vol. 153, no. 8, p. D129, 2006.

[71] S. K. Khore, S. R. Kadam, S. D. Naik, B. B. Kale, and R. S. Sonawane, "Solar light active plasmonic Au@ TiO 2 nanocomposite with superior photocatalytic performance for H 2 production and pollutant degradation," *New Journal of Chemistry,* vol. 42, no. 13, pp. 10958-10968, 2018.

[72] R. A. Ismail and R. S. Abdul-Hamed, "Laser ablation of Au–CuO core–shell nanocomposite in water for optoelectronic devices," *Materials Research Express,* vol. 4, no. 12, p. 125020, 2017.

[73] T. X. Phuoc and M. K. Chyu, "Synthesis and characterization of nanocomposites using the nanoscale laser soldering in liquid technique," *Journal of Nanoscience and Nanotechnology,* vol. 1, p. 101, 2013.

[74] A. K. Mishra *et al.*, "Superficial fabrication of gold nanoparticles modified CuO nanowires electrode for non-enzymatic glucose detection," *RSC advances,* vol. 9, no. 4, pp. 1772-1781, 2019.

Chapter 5

5.0. Conclusions

5.1. Introduction

This chapter presents a summary for findings of the study conducted on the optimization of processing parameters such as withdrawal velocity, film thickness and calcination temperature in the preparation of dip-coated pristine CuO films for photoelectrochemical (PEC) water-splitting. In addition, key findings obtained from the surface decoration of the optimized pristine CuO photocathodes with activated charcoal (AC), Silver (Ag) nanoparticles (NPs) and Gold (Au) NPs are elaborated. Lastly, some recommendations for future work are given based on the finding of the studies carried out in this dissertation.

5.2 Optimization of processing parameters

Dip-coated copper (II) oxide (CuO) thin films were prepared on fluorine-doped tin oxide (FTO) substrates using a copper acetate-based precursor solution. The processing parameters for the preparation of the films such as the withdrawal velocity, calcination temperature, and film thickness, were varied for the optimization of PEC water-splitting. The fabrication of the CuO samples was done at withdrawal rates in the range 50-200 mm/min, having films of 239.7–693.6 nm thicknesses, and annealed at 400-650 °C for 1 hour. The samples were used as photocathodes in a three-electrode PEC device for water-splitting. X-ray diffraction (XRD) and Raman patterns of the films confirmed the preparation of highly crystallized CuO films. Field emission scanning electron microscopy (FE-SEM) revealed the morphology of the thin films to consist of compact spherical nanoparticles. The cross-sectional views of the films exhibited an increase in their thickness with increasing withdrawal speed and number of film layers. EDS analysis confirmed the presence of O and Cu which were the constituent elements of the CuO films prepared. Ultra-violet-Visible (UV-Vis) spectroscopy studies indicated strong optical absorptions in the visible region with some slight absorption in the near-infrared spectrum due to the estimated low bandgap of 1.34 ± 0.04 eV obtained for all the films. Linear sweep voltammetry (LSV) measurements yielded the highest photo-current density of 2.9 mA/cm^2 at 0.35 V vs RHE for the films prepared at withdrawal speed of 150 mm/min, with thickness of

397.3 nm and annealed at 600 °C. The improved photo-current density attained by the films has been linked to the optimization of the film thickness, optical absorbance, crystallization, and the low resistance to the transfer of charge carriers at the photocathode/electrolyte interface of the films. Stability measurements performed on the most optimized pristine CuO photocathodes in terms of PEC response revealed that the films could only retain 76.2 and 28.4 % of their photo-current density after 100 and 500 s respectively. This was attributed to the photo-corrosion occurring on the films surface. The study emphasized the significance of optimizing processing parameters in the preparation of CuO films for PEC applications and revealed an innovative pathway that should precede studies concerning the stability of CuO in electrolyte.

5.3 Surface decoration of pristine CuO with activated charcoal (AC), silver (Ag), and gold (Au) nanoparticles (NPs) for the enhancement of photo-stability

The pristine dip-coated CuO photocathodes which yielded the best PEC response after optimizing processing parameters were decorated with 1, 3, and 5 thin layers of AC via spray pyrolysis for the enhancement of their photo-stability in electrolyte. The XRD and Raman patterns of the films confirmed the preparation of highly crystallized CuO/AC thin films. FE-SEM images revealed increasing agglomeration on the surface of the films following the addition of 1, 3, and 5 layers of AC. The cross-sectional views of the films showed an increase in the thickness of the films with increasing number of AC layers. EDS analysis confirmed the presence of O and Cu which are the constituent elements of CuO and carbon which result from the deposited AC. UV-Vis spectroscopy studies indicated strong optical absorption in the visible region due to the low bandgap values of 1.25 ± 0.04 eV for all the AC-incorporated CuO films. LSV measurements revealed that CuO/AC-1L produced the highest photo-current density of 1.5 mA/cm^2 at 0.5 V vs RHE, indicating a 20% increase compared to pristine CuO at the same potential. Electrochemical impedance spectroscopy (EIS) measurements affirmed the observed photo-current, as the same photocathode showed the least charge transfer resistance (R_{ct}) at the photocathode/electrolyte interface. Moreover, the maximum charge carrier density estimated for the films from the Mott-Schottky (MS) plots yielded the maximum value of 10.28 x 10^{20} cm^{-3} for the CuO/AC-1L photocathodes, further validating the enhanced photo-current response produced by the films. Chronoamperometry measurements showed a significant improvement in the photo-stability of the CuO/AC-5L photocathode, retaining 45.5 % of its photo-current after 500 s as compared to the 28.4 % sustained by the pristine CuO after the same period.

Furthermore, the pristine CuO photocathodes which yielded the best PEC response after optimizing processing parameters were also decorated with 1, 3, 5 layers of Ag NPs, using a drop-casting method to investigate the effects on their photo-stability in electrolyte. The XRD and Raman patterns verified the preparation of highly crystallized CuO/Ag NPs. FE-SEM showed a large distribution of Ag NPs over the surface of all films. Cross-sectional views of the films revealed an increase in the thickness of the films with increasing number of Ag NPs layers. UV-Vis spectroscopy showed good optical absorbance for all the films in the visible region of the electromagnetic spectrum. Furthermore, the absorption wavelengths of the films were observed to be more broaden with increasing layers of Ag NPs due to the surface plasmon resonance induced by the addition of Ag NPs. The indirect bandgap of CuO/Ag-3L and CuO/Ag-5L films were estimated to be 0.83 ± 0.02 eV, whereas for CuO/Ag-1L, it was 1.20 eV. LSV measurements showed the highest photo-current density for pristine CuO which was 2.9 mA/cm^2 at 0.35 V vs RHE. The drop in the photo-response of CuO upon the deposition of Ag was associated to the lost in the photo-current density resulting from the high photo-corrosion occurring on the surface of the pristine films. EIS measurements reveal lower charge transfer resistance for the Ag modified CuO films, indicating that the enhanced photo-current density yielded by the pristine films was due to the photo-corrosion occurring on the photocathodes. Chronoamperometry measurements revealed that the CuO/Ag-1L, CuO/Ag-3L, and CuO/Ag-5L photocathodes retained about 74. 5, 60.0 and 75.9 % of their photo-current density respectively, after 500 s. This represents a significant improvement in the photo-stability of the modified films in electrolyte when compared to the 28.4% of photo-current retained by the pristine CuO photocathodes after the same duration of 500 s. Moreover, the CuO/Ag-1L, CuO/Ag-3L, and CuO/Ag-5L photocathodes further retained about 65.9, 47.3 and 74.7 % of their photo-current density after a scan of 1200 s respectively, affirming the notable enhancement in the photo-stability of the pristine CuO films.

Lastly, the pristine dip-coated CuO photocathodes which yielded the best PEC response after optimizing processing parameters were coated with 1, 3, 5 protective layers of Au NPs, via the drop-casting technique. XRD and Raman patterns confirmed the preparation of highly crystallized CuO/Au NPs. FE-SEM micrographs of the films revealed deposits of Au NPs distributed over the surface of CuO films. Cross-sectional views of the films revealed a significant increase in the thickness of the films with increasing number of Au NPs film layers on the CuO films. UV-Vis spectroscopy showed optical absorbance of all films in the visible region, with a slight absorption in the near-infrared region of the electromagnetic spectrum. The indirect bandgaps for CuO/Au-1L and CuO/Au-3L thin films was estimated to be 1.20 ± 0.03 eV, whereas for CuO/Au-5L, the value declined to ±1.13 eV. LSV measurements also showed the highest photo-current density of 2.9 mA/cm^2 at 0.35 V vs RHE for the pristine CuO. EIS measurement revealed lower charge transfer resistance for the CuO/Au modified films as compared to the pristine photocathodes with the least value observed for CuO/Au-5L. Again, this indicates that the enhanced photo-current density yielded by the pristine CuO photocathodes was due to photo-corrosion occurring at the surface of the films. The highest charge carrier concentration was produced by CuO/Au-1L with a value of 6.751 x 10^{20} cm^{-3}, indicating enhanced charge transfer and migration at the photocathode/electrolyte junction for hydrogen evolution reactions. Chronoamperometry measurements revealed that the CuO/Au-1L, CuO/Au-3L, and CuO/Au-5L photocathodes retained about 65.0, 85.1, and 87.9 % of their photo-current density after 500 s respectively. This represents a significant improvement in the photo-stability of the films in electrolyte when compared to the 28.4% of photo-current retained by the pristine CuO photocathodes after the same period. More so, the CuO/Ag-1L, CuO/Ag-3L, and CuO/Ag-5L photocathodes further retained about 58.4, 83.6, and 84.3 % of their photo-current density after a scan of 1200 s respectively.

5.4 Future work

The deposition of AC, Ag and Au of the surface of pristine CuO films notably enhance the photo-stability of the films in electrolyte as stated in sections 5.3. However, the photo-current density was lower for most of the CuO films after modification with AC, Ag and Au which was largely attributed to the significant drop in photo-corrosion occurring on the pristine films. Notwithstanding, it will be important to device ways of improving the stability of CuO photocathodes in electrolyte while maintaining or further enhancing its photo-current density. Also, since only the thickness of AC, Ag, or Au NPs was varied as discussed in sections 4.3, 4.4 and 4.5, the influence of parameters such as concentration [1], and annealing temperature [2] may also need to be investigated for possible improvement of the photo-current response of the modified films while maintaining or even further enhancing their photo-stability.

In addition, the deposition techniques of thin films play an important role in the outcome of structural, morphological, optical, and PEC properties of thin films [3]. Thus, exploring other techniques for the deposition of AC, Ag and Au protective layers on the surface of the pristine CuO films can further influence the photo-current response and photo-stability of the films for enhanced PEC water-splitting.

References

[1] B. Koo *et al.*, "Reduced graphene oxide as a catalyst binder: greatly enhanced photoelectrochemical stability of Cu (In, Ga) Se2 photocathode for solar water splitting," *Advanced Functional Materials*, vol. 28, no. 16, p. 1705136, 2018.

[2] J. Gu *et al.*, "A graded catalytic–protective layer for an efficient and stable water-splitting photocathode," *Nature Energy*, vol. 2, no. 2, pp. 1-8, 2017.

[3] P. I. Kyesmen, N. Nombona, and M. Diale, "Influence of coating techniques on the optical and structural properties of hematite thin films," *Surfaces and Interfaces*, vol. 17, p. 100384, 2019.

Appendix

Publication

[1] Nteseng D. M. Mosalakgotla, Pannan I. Kyesmen and Mmantsae Diale, “Optimization of processing parameters of dip coated CuO films for photoelectrochemical water-splitting,” *Surfaces and interfaces* [Under review].